

CELL BEHAVIOR OF HUMAN-FETAL-OSTEOBLASTS (hFOB) AND *STAPHYLOCOCCUS AUREUS* ON NANOSTRUCTURED TITANIUM ALLOY Ti-13Nb-13Zr (NanoTNZ)

Christopher Spiegel¹, Lina Klinge², Lukas Kluy³, Peter Groche³, Carsten Siemers² and Débora C. Coraça-Huber¹

¹ Research Laboratory for Biofilms and Implant Associated Infections (BIOFILM LAB), Medical University of Innsbruck, Innsbruck.

² Institute for Materials Science, TU Braunschweig, Brunswick, Germany.

³ Institute for Production Engineering and Forming Machines, TU Darmstadt, Darmstadt, Germany.

Titanium and titanium alloys are the most suitable metallic materials in implant engineering, whereas currently, 1–2% of all prosthetic joint surgeries are followed by an infection. Prosthetic joint infections are mainly caused by *Staphylococcus aureus*. The formation of biofilms helps bacterial cells to withstand critical environmental conditions. Due to their tolerance against antibacterial substances, biofilms are a significant problem in modern medicine. Nanostructured titanium alloys have shown promising results on controlling bacterial adhesion and growth in comparison to adhesion of osteoblasts. To accomplish the requirements for lighter, more elastic materials with a nanostructured surface, Ti-13Nb-13Zr (TNZ) shows promising properties. In this study we investigated cell adhesion and proliferation of human-fetal-osteoblasts (hFOB 1.19) and *Staphylococcus aureus* ATCC 29213 on nanostructured Ti-13Nb-13Zr, a second-generation biomedical β -rich ($\alpha+\beta$)-titanium alloy which was produced by equal channel angular swaging (ECAS) followed by recrystallisation and ageing treatments. In addition, CP Titanium Grade 4 and Ti-6Al-4V ELI were investigated as reference materials. To evaluate the adhesion and proliferation of hFOB 1.19, we performed cell counting after 72 h of cultivation with a hemacytometer, following RNA extraction and RT-PCR with suiting primers for cell proliferation and differentiation. In addition, scanning electron microscopy was used to gain insights into cell morphology of hFOB 1.19 on nanostructured Ti-13Nb-13Zr. Bacterial adhesion and proliferation of *Staphylococcus aureus* ATCC 29213 was studied by colony forming unit counting after 24 h of incubation together with SEM analyses. The results of our investigations will help to optimize the microstructure of Nano-TNZ with respect to good osteoblast adhesion and minimized bacterial colonization and biofilm production to allow the development of TNZ-implants with enhanced biological properties.

Keywords: nanostructured titanium, Ti-13Nb-13Zr, TNZ, NanoTNZ, medical implants.

1. Introduction

Titanium and titanium alloys are the most suitable metallic materials in implant engineering, whereas currently, 1–2% of all prosthetic joint surgeries are followed by an infection [1]. Prosthetic joint infections are mainly caused by *Staphylococcus aureus* strains which could lead to severe health problems [2]. *Staphylococcus aureus* have the capability of biofilm formation and methicillin resistance [3, 4]. Of all dental implantations 19% - 65% suffer from peri-implant mucositis and up to 47% from peri-implantitis [5]. Crestal bone loss and an inflammatory reaction can be classified as part of the clinical picture of peri-implantitis which might result in total implant loss [6-8]. Possible causes of peri-implantitis are bacterial infections, disruption of the peri-implant connection and corrosion [9]. The formation of biofilms helps bacterial cells to withstand critical environmental conditions like antibiotic therapies [10]. Due to their tolerance against antibacterial substances, biofilms are a significant problem in modern medicine.

In this project we examined Ti-13Nb-13Zr (TNZ, NanoTNZ) as an alternative to the commonly used titanium alloys CP titanium grade 4 (CP4) and Ti-6Al-4V ELI (Ti64ELI) as the latter contains the potentially critical alloying elements aluminium (Al) and vanadium (V) and both have a relatively high Young's modulus which might

cause stress shielding and gap formation between the implant and the bone [11]. Ti-13Nb-13Zr is a second-generation β -rich ($\alpha+\beta$)-titanium alloy for biomedical applications which was nanostructured in this project by equal channel angular swaging (ECAS) followed by recrystallisation and ageing treatments [12, 13]. Nanostructured titanium alloys have shown promising results on controlling bacterial adhesion and growth [4].

2. Biological Experiments

2.1. Materials

In this study we examined titanium Ti64ELI, CP4, both in the as received conditions (fine globular microstructures) and Ti-13Nb-13Zr alloys (TNZ, NanoTNZ). We examined two different Ti-13Nb-13Zr material conditions, TNZ and NanoTNZ. Rotary swaging has been carried out on both materials. (i) A heat treatment at 700 °C for 10 minutes was carried out for TNZ material, followed by water quenching to produce a fully (soft) α' -martensitic structure in the former β -grains. For the ageing process, the material was heat treated at 500 °C for 60 minutes and air cooled (martensite decomposition). (ii) In addition, an ECAS-deformed, rotary swaged, recrystallised and aged material state with a nanostructured microstructure (NanoTNZ) was produced. This microstructure consists of nanoscale primary α -grains (α_p) and β -phase with even smaller

secondary α precipitates (α_s). After rotary swaging a heat treatment of 750 °C for 30 minutes, followed by water quenching was performed. Then the ECAS process was applied to the material. Afterwards, recrystallisation was carried out by a heat treatment in the ($\alpha+\beta$)-phase field at 700 °C for 10 minutes followed by water quenching (to transform the β -phase to α -phase). Afterwards this martensite has been partially decomposed at 500 °C for 60 minutes and cooled of at air, to produce the final nanostructured microstructure.

The samples used for the biological investigations had a cylindrical geometry with 6 mm of height and 6 mm of diameter. All samples were ground and polished (final size 0.05 μm). Ti64ELI and CP4 samples were etched for 8 seconds with Krolls reagent containing 2.7 % hydrofluoric acid, 5.5 % nitric acid and 91.7 % TNZ and NanoTNZ samples were etched for 3 seconds with a reagent, containing 4.7 % hydrofluoric acid, 4.2 % nitric acid, 11.1 % hydrogen peroxide and 80 % H_2O . Prior to use, all samples have been cleaned in sterile distilled water and were sterilized with UV-light for 1 h at 254 nm with 40 $\mu\text{W}/\text{cm}^2$ intensity (ESCO SC2-6E1, UV-30A Lamp) to ensure similar starting conditions.

2.2. Biofilm formation

Before use, for each pre-culture of *Staphylococcus aureus* ATCC 29213, 3 colonies were suspended in 2 mL of TSB + 1% Glu media in a 15 mL centrifuge tube (VWR International, Radnor, PA, USA). The pre-cultures were incubated in a moisture chamber at 37 °C on a shaker with 200 rpm for 24 h. To ensure biofilm growth on the upper circular area of the titanium cylinders, a silicone O-ring sealed off the upper sample area fitting into a well of a 48-well plate. Six titanium samples were used for each strain. The pre-cultures were diluted 1:100 to reach an initial cell count of 10^3 per mL media. A total of 500 μL of each culture dilution were pipetted in each well used.

2.3. Colony forming unit analysis

After biofilm formation, we removed the remaining media. We used nine replicates for each material. Following this, we removed the titanium samples from the 48-well plates and washed them in PBS to remove planktonic bacteria cells. We added the samples into sterile vials. Then, we added 500 μL of TrypLE (Thermo Fisher Scientific, Waltham, MA, USA) to remove bacteria cells from the titanium surface. Before and after 5 min of incubation at 37°C, we vortexed each vial for 15 s. To inactivate TrypLE, we added 500 μL of DMEM media. Before dilution steps were initiated, we

vortexed each vial. We diluted each vial from 10^{-1} to 10^{-8} with TSB + 1% glucose and plated 10^{-6} to 10^{-8} dilutions in triplicates on MHA plates. The freshly plated MHA plates were incubated for 48 h at 37 °C. After incubation, we counted the CFU.

2.4. Osteoblast adhesion and proliferation

Prior to osteoblast adhesion to the titanium samples used, we precultured *hFOB 1.19* cells in two passages to 90% confluency. For the first subculture we seeded 1×10^4 osteoblasts in a 75 mL cell culture flask in 10 mL of Dulbecco's Modified Eagle Medium: Nutrient Mixture F12 (Gibco, Life Technologies, USA) in combination with 10 % FCS and 1 % of Pen-strep. The preculture got incubated at 34 °C at 95% humidity and 5 % of CO_2 to 90% confluency. After 90% confluency was reached, we passaged the cells, starting with 1×10^4 cells and incubated them up to 90% confluency. The media got changed every 48 hours.

After 90% confluency was reached of the second passage, we extracted the cells for adhesion on the titanium samples used. To do so, we removed the old media, washed the cells in 5 mL phosphate-free PBS, removed the PBS and added 5 mL of TrypLE (Thermo Fisher Scientific, Waltham, MA, USA). After 5 min at 37°C of incubation we deactivated the trypsin with 10 mL of DMEM F12 media. Then 15 mL of the cells got transferred to a 15 mL falcon and were centrifuged at 200 g for 5 min. The liquid got removed and 2 mL of DMEM F12 media was added and mixed. Afterwards, the cells were diluted to $1-2 \times 10^4$ cells /mL and added per well of a 48-well plate in a total volume of 500 μL per well. Before the cells were added, titanium samples were washed in sterile distilled water and sterilized with UV-light for 1 h at 254 nm with 40 $\mu\text{W}/\text{cm}^2$ intensity (ESCO SC2-6E1, UV-30A Lamp). For osteoblast growth on the upper circular area of the titanium cylinders, the upper sample area was sealed off with a silicone O-ring to fit into a well of a 48-well plate. After addition of the cells to the titanium samples, the setup got incubated for 72 h at 34°C at 95% humidity and 5% CO_2 atmosphere. The media was exchanged after 48 hours of incubation.

2.5. Osteoblast cell counting

After 72 h of incubation the osteoblast adhesion was controlled by cell counting. We removed the used media, washed each well with 250 μL of PBS, removed the PBS and added 500 μL of TRYPLE. After 5 min at 37°C of incubation, we deactivated trypsin of the cells by adding 500 μL of DMEM F12 media. The cells got extracted and of each well, 1 mL of cell containing liquid was added to a 1.5 mL reaction tube. The tubes

were centrifuged at 200 g for 5 min. The media was removed and 1 mL of DMEM F12 Media was added. In the next step, the cells were counted with Trypan blue solution in a Neubauer improved chamber.

2.6. Bacterial biofilm primers and osteoblast proliferation primers

To evaluate expression levels of genes responsible for biofilm formation on CP 4, Ti64ELI, TNZ and NanoTNZ we used the following genes and primers:

Table 1. Primer tables for biofilm related genes and cell stress related genes for Staphylococcus aureus ATCC 29213

Gene	Forward primer Reverse primer
ica A	5'- CGC ACT CAA TCA AGG CAT TA -3' 5'- CCA GCA AGT GTC TGA CTT CG -3'
ica B	5'- CAC ATA CCC ACG ATT TGC AT -3' 5'- TCG GAG TGA CTG CTT TTT CC -3'
ica C	5'- CTT GGG TAT TTG CAC GCA TT -3' 5'- GCA ATA TCA TGC CGA CAC CT -3'
ica D	5'- ACC CAA CGC TAA AAT CAT CG -3' 5'- GCG AAA ATG CCC ATA GTT TC -3'
SarA	5'- AAG GAC AAT CAC ATC ACG AAG -3' 5'- GAA CGC TCT AAT TCA GCG G -3'
SodA	5'- GTT TCA TCA CGA CAA ACA TCA C -3 5'- TGA CAT CCT CAT CGC TTC C -3'
SigB	5'- AGA AGC AAT GGA AAT GGG AC -3' 5'- CTT AAA CCG ATA CGC TCA CC -3'
16s	5'- GAA AGC CAC GGC TAA CTA CG -3' 5'- CAT TTC ACC GCT ACA CAT GG -3'

For osteoblast proliferation, the following primers were designed and used:

Table 2. Primer table for proliferation genes of hFOB 1.19

Gene	Forward primer Reverse primer
Runx 2.1	5'- CAC CAT GTC AGC AAA ACT TCT T -3' 5'- TCA CGT CGC TCA TTT TGC -3'
Runx 2.2	5'- GTG CCT AGG CGC ATT TCA -3' 5'- GCT CTT CTT ACT GAG AGT GGA AGG -3'
Col1A1	5'- CAA GAG TGG TGA TCG TGG TG -3' 5'- GCC TGT CTC ACC CTT GTC A -3'
Col2A1	5'- AGA GGG CAA TAGC AGG TTC A -3' 5'- GCG TGA GGT CTT CTG TGA CC -3'
ALPL	5'- CCA TCC TGT ATG GCA ATG G -3' 5'- CGC CTG GTA GTT GTT GTG AG -3'
BMP7	5'- TCA GCG TTT ATC AGG TGC TC -3' 5'- CCA GAG GGT ACG GCT GTC -3'
GAPDH	5'- AGC CAC ATC GCT CAG ACA C -3' 5'- GCC CAA TAC GAC CAA ATC C -3'

2.7. RNA extraction, cDNA synthesis and Real-Time Quantitative Polymerase Chain Reaction Analysis (RT-qPCR)

Before the extraction of bacterial RNA, 24 h of biofilm formation with Staphylococcus aureus ATCC 29213 on titanium samples was performed. To extract RNA from osteoblasts, 72 h of osteoblast proliferation of hFOB 1.19 cells on titanium samples was performed. We used for each material 6 samples to extract RNA. The RNA extraction, cDNA synthesis step and RT-qPCR analysis were adapted from Spiegl et.al [15].

2.8. Scanning electron microscopy

To characterize biofilm formation and osteoblast proliferation on the titanium samples, pictures were taken with a scanning electron microscope. After biofilm formation and proliferation of osteoblasts the titanium samples got fixed overnight in 500 µL of 2.5% glutaraldehyde. After fixation, the samples got dehydrated in an ascending alcohol series 50%-70%-80%-99.9% of ethanol for 5 minutes for each stage. The titanium cylinders were then fixed onto aluminium pins with Leit-C gluing strips (Göcke, Plano GmbH, Wetzlar, Germany). The samples and pins were sputtered with Au for 40 seconds (Agar Sputter Coater, Agar Scientific Ltd., Stansted, GB). The samples were then analysed by scanning electron microscopy (SEM, JSM-6010LV, JEOL GmbH, Freising, Germany).

3. Results and Discussion

3.1. Colony forming unit analysis

The lowest count of colony forming units (CFU) occurred on the NanoTNZ material with 5.01×10^6 CFU/mm² (SD: $\pm 3.56 \times 10^6$ CFU/mm²) whereas the highest CFU count was found on etched TNZ material with 15.56×10^7 CFU/mm² (SD: $\pm 1.15 \times 10^7$ CFU/mm²). CP 4 titanium and Ti64ELI showed CFU counts of 1.09×10^7 CFU/mm² (SD: $\pm 7.3 \times 10^6$ CFU/mm²) and 9.09×10^6 CFU/mm² (SD: $\pm 6.0 \times 10^6$ CFU/mm²). Therefore, the results do not show a significant difference between the different alloys, but a tendency that ECAS is able to improve the antibacterial properties of TNZ can be observed.

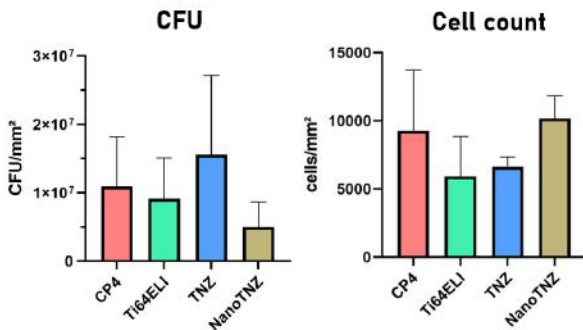


Figure 1. Colony forming units of *Staphylococcus aureus* ATCC 29213 and cell count of hFOB 1.19 on Titanium CP Grade 4, Ti-6Al-4V ELI, TNZ RS 700 and NanoTNZ

3.2. Osteoblast adhesion

Osteoblast proliferation and adhesion was highest on NanoTNZ samples with 10168 cells/mm². On CP 4 samples osteoblasts grew with 9284 cells/mm² and on Ti64ELI with 5924 cells/mm². TNZ samples showed 6631 cells/mm².

3.3. PCR

The bacterial biofilm gene expression showed no higher expression on Ti64 ELI in comparison to CP 4 (figure 1). Whereas on TNZ in comparison to CP 4, the gene expression was higher regulated in IcaB, 1.39 times, IcaC, 3.89 times, IcaD, 4.62 times, SigB, 4.41 times, SarA, 2.17 times and sodA, 1.38 times higher. NanoTNZ material showed the highest upregulation of biofilm related genes and cell stress related genes with an upregulation between 4 to 40 times higher than on CP 4. The upregulation of biofilm related genes (IcaA, D, B, C) and cell stress related genes (SigB, SarA, sodA) indicate an antibacterial influence on *Staphylococcus aureus* ATCC 29213 due to cell stress(4). As SigB and SarA are both involved in cell stress and biofilm upregulation, a higher regulation of both genes is to be expected, when

Ica-cascade genes and superoxide dismutase gene sodA are also upregulated.

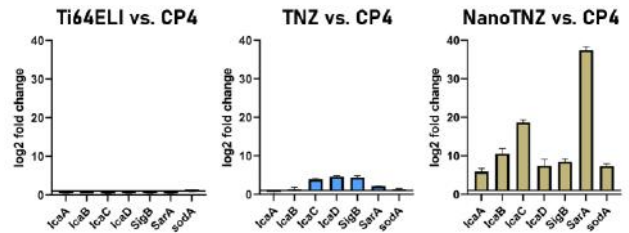


Figure 2. Biofilm related gene expression of IcaADBC genes and cell stress related genes SigB, SarA and sodA of *Staphylococcus aureus* ATCC 29213 on Ti64ELI, TNZ 700 and NanoTNZ in comparison to Titanium CP Grade 4

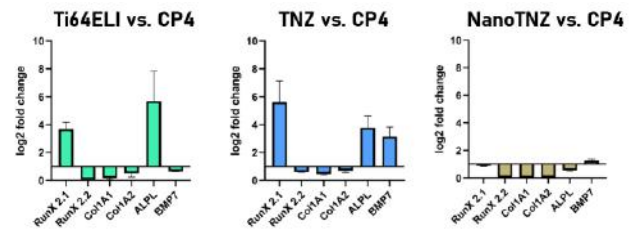


Figure 3. Proliferation related gene expression of RunX 2 genes, collagen type 1 genes, alkaline phosphatases and BMP7 of hFOB 1.19 cells on Ti64ELI, TNZ 700 and NanoTNZ in comparison to Titanium CP Grade 4

The proliferation gene expression of hFOB 1.19 cells showed an upregulation on Ti64ELI in comparison to CP 4 within the RunX 2 variant 1 gene and alkaline phosphatases. Collagen type 1 variant 1 and 2 were down regulated as RunX 2 variant 2 and BMP7. The downregulation of BMP7 indicates a cell proliferation as BMP7 is inhibiting osteoblast proliferation and stimulates cell differentiation. On TNZ material also RunX2 variant 1, alkaline phosphatases and BMP7 were upregulated. On NanoTNZ all genes but BMP7 were downregulated.

3.4. Scanning electron microscopy

The bacterial cell morphology of *Staphylococcus aureus* ATCC 29213 on NanoTNZ differed compared to the cell morphology on CP4 titanium, Ti64ELI and TNZ samples (figure 3). The cells on CP4 titanium, Ti64ELI and TNZ are more roundly shaped, sometimes with a hole in the middle of the cells. On NanoTNZ the bacteria seem to be more fractured and roughed. Cells with a hole in the middle are less common. The more fractured shape indicates cellular stress. This morphological observation may correspond to observed lower CFU count and higher gene expression of cell stress genes. Scanning electron microscopy images showed confluent osteoblasts on all examined materials.

On CP 4 titanium and on NanoTNZ osteoblasts showed more stretched cell nucleolus than on Ti64ELI and on TNZ (figure 4). As hFOB 1.19 are fibroblast-like

in cell morphology and in confluency, this indicates that confluency is already reached on CP4 titanium and NanoTNZ in comparison to Ti64ELI and TNZ.

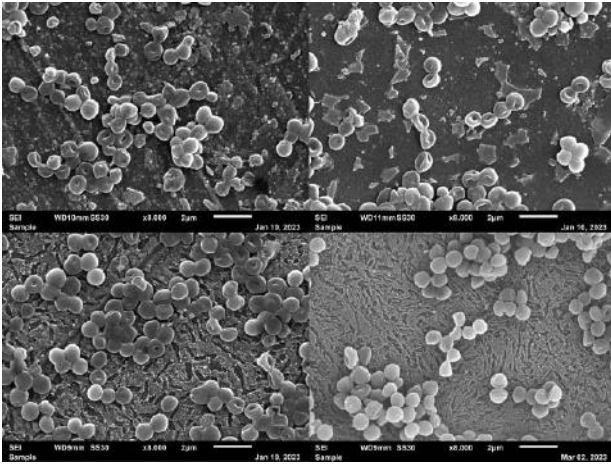


Figure 4. Scanning electron microscopy pictures of *Staphylococcus aureus* ATCC 29213 on CP grade 4 titanium, Ti64ELI, TNZ 700 and NanoTNZ after 24 hours of incubation.

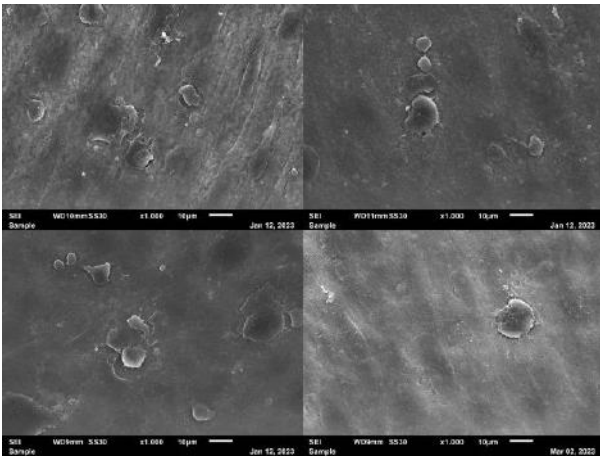


Figure 5. Scanning electron microscopy pictures of hFOB 1.19 on CP grade 4 titanium, Ti64ELI, TNZ 700 and NanoTNZ after 72 hours of incubation

3.5. Influence of TNZ and the ECAS process on bacteria and osteoblasts

The examined NanoTNZ material showed lower bacterial growth after 24 h of incubation and higher genes expression of biofilm genes and cells stress genes. In addition, SEM showed a more fractioned cell morphology. Aguilera-Correa et al. connected the antibacterial properties to the production of hydroxyl radicals on Ti13Nb13Zr alloy [16]. As the formation of hydroxyl radicals is resulting in oxidizing stress for the bacterial cells, our findings of increased expression of superoxide dismutase A (*sodA*) are matching to the literature [17]. NanoTNZ and CP4 titanium allowed higher osteoblast proliferation after 72 h of incubation, leading to already reduced cell proliferation gene activity, higher cell counts and more length of cell shape. Higher BMP7 expression indicates a completed cell proliferation

and an already initiated cell differentiation of hFOB 1.19 [18]. NanoTNZ itself seemed to be as biocompatible as CP grade 4 titanium. In previous studies of Park et al. osteoblasts showed increased proliferation on TNZ [19]. As surface modifications are crucial for osteoblast adhesion and proliferation, nanostructured surfaces are stimulating osteoblasts to proliferate due to increased attachment to integrins [20]. In comparison of the cell count of osteoblasts between Ti64ELI and the other titanium alloys, the lower osteoblast count can be related to the vanadium content of the alloy. It has been reported that vanadium has cytotoxic activity [21].

4. Summery and Outlook

The present study shows that NanoTNZ has the tendency to a lower bacterial growth and increased bacterial cell stress on the surface. NanoTNZ shows higher adhesion and proliferation to an earlier reached confluency of hFOB 1.19 cells. These findings suggest that NanoTNZ may be useful to tackle periprosthetic joint infections when compared to the commonly used Ti64ELI for hip implants. NanoTNZ also seems to have improved antibacterial properties when compared to CP4, which makes it suitable to replace CP4 as a standard material. Therefore, NanoTNZ can be considered as a safe and promising alternative to commercial materials like CP 4 titanium and Ti64ELI. These advantages can also improve hip prosthesis properties. Upscaling the ECAS process and adapt it to an application for prosthetic implants like hip implants should be examined.

5. Support and Partner

We would like to thank ADVANTIQX Dr. Scherer, Gersthofen, Germany for their support during these studies.

6. References

1. Ahmed SS, Haddad FS. *Prosthetic joint infection. Bone Joint Res.* 2019; 8 (11): 570-2.
2. Arciola CR, Campoccia D, Montanaro L. *Nat Rev Microbiol.* 2018;16(7):397-409.
3. Peacock SJ, Paterson GK. *Annu Rev Biochem.* 2015; 84:577-601.
4. Arciola CR, Campoccia D, Ravaioli S, Montanaro L. *Front Cell Infect Microbiol.* 2015;5:7.
5. Derks J, Tomasi C. *J Clin Periodontol.* 2015;42 Suppl 16:S158-71.
6. Albrektsson T, Jemt T, Mölne J, Tengvall P, Wennerberg A. *Clin Implant Dent Relat Res.* 2019; 21(1):183-9.
7. Albrektsson T, Dahlin C, Jemt T, Sennerby L, Turri A, Wennerberg A. *Clin Implant Dent Relat Res.* 2014;16(2):155-65.

8. Trindade R, Albrektsson T, Galli S, Prgomet Z, Tengvall P, Wennerberg A. *Clin Implant Dent Relat Res.* 2018;20(1):82-91.
9. Mouhyi J, Dohan Ehrenfest DM, Albrektsson T. *Clin Implant Dent Relat Res.* 2012;14(2):170-83.
10. Arciola CR, Baldassarri L, Montanaro L. *J Biomed Mater Res.* 2002;59(3):557-62.
11. Haase F, Siemers C, Klinge L. *MATEC Web Conf* 2020. 2020
12. Klinge, L., Siemers, C., Kluy, L. et al. *Journal of Materials Research* 37, 2581–2588. 2022
13. Kluy L, Chi F, Groche P. *WGP Production at the leading edge of technology.* 2021
14. Bright R, Fernandes D, Wood J, Palms D, Burzava A, Ninan N, et al. *An. Mater Today Bio.* 2022;13:100176.
15. Spiegel C, Nogler M, Coraça-Huber DC. *Antibiotics* (Basel). 2022;11(11).
16. Aguilera-Correa JJ, Conde A, Arenas MA, de-Damborenea JJ, Marin M, Doadrio AL, et al. *Biomed Mater.* 2017;12(4):045022.
17. Ballal A, Manna AC. *J Bacteriol.* 2009;191(10):3301-10.
18. Setzer B, Bächle M, Metzger MC, Kohal RJ. 2009;30(6):979-90.
19. Park CH, Lee CS, Kim YJ, Jang JH, Suh JY, Park JW. *Clin Oral Implants Res.* 2011;22(7):735-42.
20. Lopes HB, Freitas GP, Elias CN, Tye C, Stein JL, Stein GS, et al. *J Biomed Mater Res A.* 2019;107(6):1303-13.
21. Niinomi M, Liu Y, Nakai M, Liu H, Li H. *Regen Biomater.* 2016 Sep; 3(3):173-85.

ENHANCED BIOMECHANICAL PERFORMANCE OF ADDITIVELY MANUFACTURED Ti-6Al-4V BONE PLATES AND THEIR CLINICAL APPLICATIONS

Saurabh Kumar Gupta¹, Sathya Vamsi Krishna², Satyam Suwas¹, Kaushik Chatterjee¹

1 Department of Materials Engineering, Indian Institute of Science, Bangalore, India

2 Department of Hand Surgery, Sanjay Gandhi Institute of Orthopaedics and Trauma, Bangalore, India

Additive manufacturing (AM) is a layer-by-layer manufacturing process which can build complicated parts in near net shape. We have utilized selective laser melted implants to treat deformities in upper limb. For this purpose, a workflow was established. Bone models were generated from X-ray computed tomography (CT-scan) data. Bone models were designed along with patient specific surgical guide and bone plates personalized for each patient. The bone plate was subjected to a cyclic heat treatment below β -transus temperature to improve the biomechanical performance of the plate. The heat-treated plate was characterized for microstructural and mechanical characterization before final implantation.

Keywords: Ti-6Al-4V; Bone plates; Selective laser melting; Heat treatment; Mechanical properties

1. Introduction

Titanium and its alloys are the most widely used metallic implants for bone osteosynthesis [1,2]. These implants are typically composed of commercially pure titanium (cp-Ti) and Ti-6Al-4V ELI. The alloys are processed through machining to achieve standard shapes and sizes of implants. The market share of metallic implants is increasing rapidly with growing incidences of trauma. Surgeon uses standard implants available commercially for surgeries. However, certain complex deformities of bone require bone specific plates with bends and twists to match the bone which might be cumbersome with commercially available implants. The manual contouring of the plate will not alone be a imperfect task but weaken the structure of the implant. Owing to poor fit, these surgeries can result in poor/improper healing of the bone tissue resulting in reduced functionality of the recovered bone in the patient even after complete healing of the defect.

Additive manufacturing is a layer-by-layer fabrication process that is broadly divided into two categories namely, selective laser melting (SLM) and directed energy deposition (DED) [3–5]. SLM is of much importance for biomedical applications as it offers geometric tolerance of 100-200 μm to enable fabrication of near net shape parts [6,7]. Additive manufacturing of Ti-6Al-4V is studied enormously in literature as it is a popular alloy in aerospace, chemical, and biomedical industries [8–14]. In short, the microstructure, mechanical behavior, and crystallographic texture of SLM produced Ti-6Al-4V differs from conventionally produced part. Many studies are focused on changing the microstructure of SLMed Ti64 to yield a better microstructure to improve the biomechanical performance of the alloy [8,13,14]. Recent studies from our group reported that martensitic microstructure of as-fabricated Ti-6Al-4V could be converted into bimodal microstructure by thermal cycling

below β -transus temperature for small sample coupons and then in bigger plates [15,16]. All aspects of Ti-6Al-4V were studied such as biological, electrochemical, and mechanical properties to conclude that the heat treatment of the additively manufactured Ti-6Al-4V parts could be a favorable process for the fabrication of patient-specific implants.

With Patient specific implants we are not only able to create customised plates but also ensures the proper fitting of implant over bone additional strength? quality thereby improving the ease of surgery for surgeons and improve overall functional outcome for patients. Recent introductions of several open source and commercially available software have opened new opportunities for designing patient-specific implants by analyzing the X-ray computed tomography (CT-scan) or Magnetic resonance imaging (MRI) data. Most of this technology is being used for the fabrication of maxillofacial and cranial implants [17] and little is reported in the literature for hand surgeries. In addition, this software also allows us to fabricate guides to execute surgical procedure.

This work involved SLM of Ti-6Al-4V ELI powder to fabricate patient-specific implants for treating deformities in the upper limb. The part was characterized after fabrication and following heat treatment. One patient with deformity was treated with virtual surgical planning and patient-specific implant in this study.

2. Materials and methods

2.1. Case report

This study was performed with approvals of the Institutional Review Board and Human Ethics Committee. Consent of the patient/guardian was taken before the surgery. The 12 years old male patient presented to us deformed left elbow following childhood

trauma due to which he was unable to perform his daily activity. There was a cubitus varus deformity at the elbow. After radiographic examination, the elbow had abnormal fusion of proximal radius and ulna bones with deformity limiting his forearm rotations. He is concerned about the bent elbow. After discussion with the patient about various possible options, the patient decided to agreed to treatment of his deformity using the surgical planning with the help of additively manufactured part. For this purpose, raw radiographic data obtained in DICOM format from a CT scan of both the elbows was analyzed in Mimics (Materialise, Leuven, Belgium) to reconstruct bone models using the segmentation (based on Hounsfield units of the bone). Examination of these generated bone models revealed bone deformity, and surgical planning was performed to treat the deformity and achieve perfect alignment of the bone in 3Matic (Materialise, Leuven, Belgium). On comparison of both the joints using 3d models it was realised that the deformity was from proximal forearm bones rather distal humerus. Surgical simulation was done with software and printed models to plan the correct site to perform the surgical cut. The surgical guide was designed to achieve the perfect straight cut of the bone and to drill hole positions of the screws for anchoring the implant. Bone models and surgical guides were printed with poly(lactic acid) (PLA) in the Ultimaker S5 Bundle. After achieving proper alignment, a bone plate was designed for patient-specific surgery. SLM of Ti64 was performed in Supercraft3D, Bangalore, India. As fabricated bone plate was subjected to heat treatment which comprises repeated controlled cyclic heating and cooling below β -transus temperature [15]. The microstructural and mechanical performance of these plates was analyzed by X-ray and optical and scanning electron microscopy along with hardness measurements. Samples for above-mentioned characterization were cut from the as-fabricated (AM) and heat-treated (HT) plates using a wire electrical discharge machine. Samples were mechanically polished following standard metallographic procedure followed by electropolishing.

During surgery day, patient was taken for surgical procedure under regional anaesthesia. Dorsal elbow approach was used to expose the proximal radius and ulna. The 3d fabricated guides were placed on the proximal ulna and pre-determined osteotomy was done. Proximal radio-ulnar synostosis release was performed. The ulna was rotated and fixed the 3D printed plate. Skin was closed in layers and the limb was immobilised in above elbow splint. The movement at the elbow was started at the elbow at 6 weeks. Though the synostosis

recurred, the deformity was corrected restoring the elbow range of motion.

Table 1: Tabulated values of phases and hardness

Condition	Phases	Hardness (HV)
		Mean \pm S.D.
AM	α'	410 \pm 11
HT	α and β	330 \pm 17

3. Results

3.1. Surgical planning

Figure 1a shows the bone models and deformity in the form of the joint between the radius and ulna. For proper alignment, a cut on the bone followed by a rotation of bone was planned on ulna. After achieving proper alignment, the bone plate was designed, as shown in Figure 1b. Figure 1

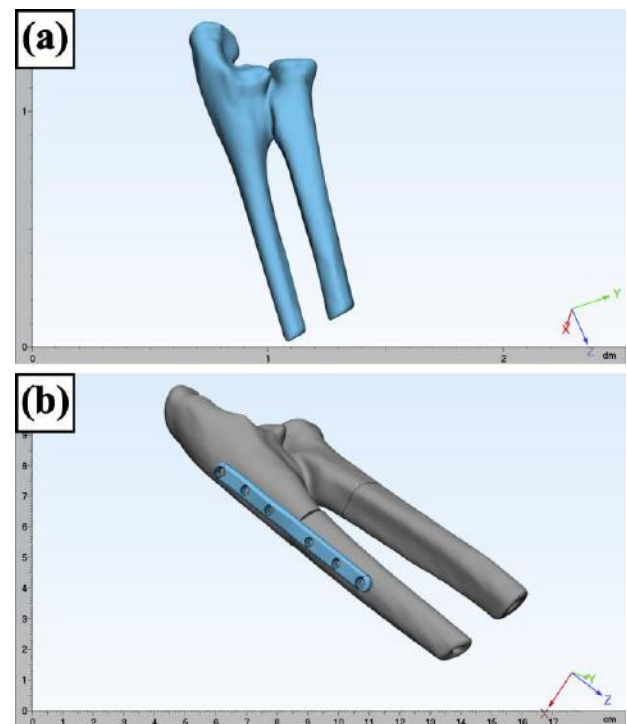


Figure 1 Surgical planning for case (a) bone before surgery, (b) bone in correct alignment with implanted patient-specific bone plate

3.2. X-ray based characterization

Figure 2 shows the X-ray diffraction patterns of AM and HT plates. AM samples do not show any β phase. Fast cooling rate of AM is believed to generate martensitic phase (α') in AM. All the peaks correspond to α titanium. In HT samples, the presence of β phase is seen along with the α -phase.

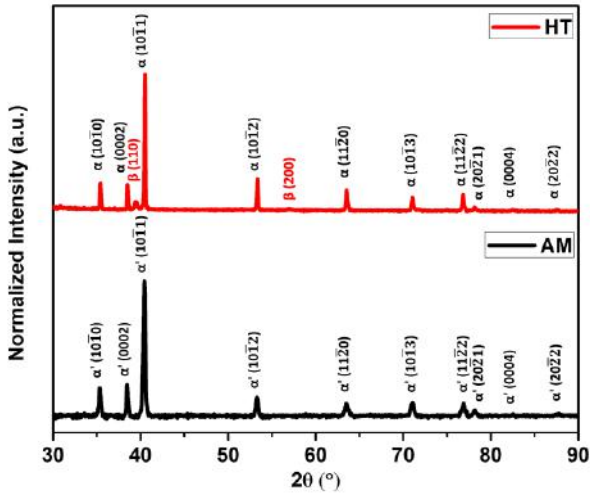


Figure 2 X-ray diffraction patterns for the experimental alloy under AM and HT conditions.

3.3. Microstructural characterization

Figure 2 shows the microstructure of AM and HT samples. The microstructure of AM samples contains fully martensitic laths of α' while that of HT sample consists of bimodal microstructure. Primary α (α_p) and lamellae of secondary α (α_s) and β phases are the constituents of bimodal microstructure.

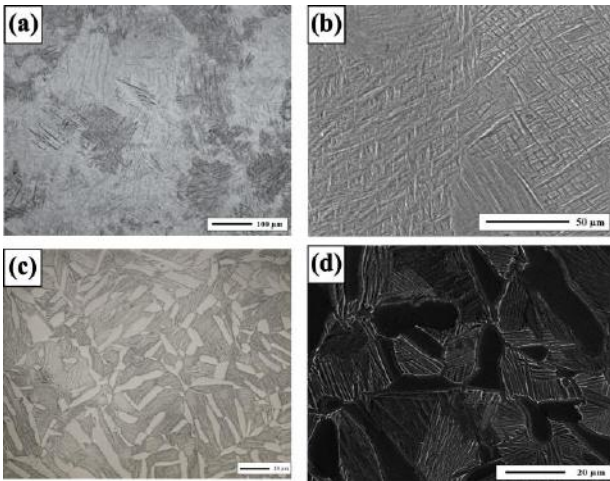


Figure 3 Optical (a, c) and electron (b, d) micrographs of AM (a, b), HT (c, d)

3.4. Mechanical characterization

The hardness of AM and HT samples are included in Table 1. AM samples show higher hardness value, which is attributed to martensitic phase (α') of titanium which is already strained due to the higher cooling rate of SLM. HT samples show lower hardness value as compared to AM samples.

3.5. Surgical implantation

Surgery of the patient was performed in operation theatre at the orthopaedic hospital, and photographs of the surgery is shown in Figure 4. The similarity of the bone model with the tissue confirms the ability of the printed part to recapitulate the shape and dimensions of the tissue using the imaging and virtual planning. The fitting of the surgical guide over the bone is highly sensitive to the spatial location on the bone of the arm. This ensures that cut and drilling on the bone is at the exact location which greatly helps the surgeon to save time and ensure precision during the surgery. Patient-specific bone plate was implanted to achieve best possible alignment and anatomical fit, as designed in surgical planning.

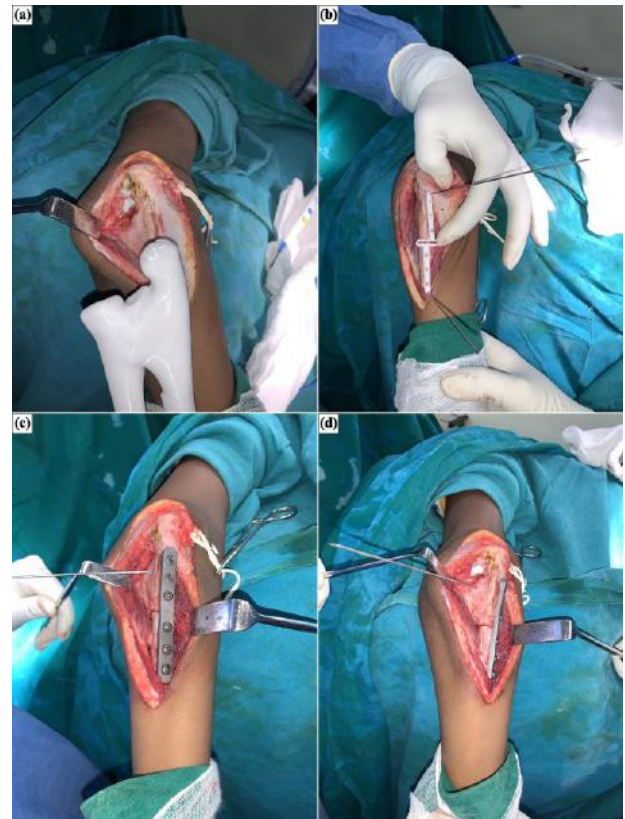


Figure 4 A schematic of surgery steps showing (a) Bone models and bone after cutting the skin, (b) Surgical guide placed over Ulna, (c, d) bone plate implanted on ulna

4. Discussion

Deformities in upper limb require a little complicated surgery to achieve proper alignment of the bone to improve functional outcome of the upper limb. Proper surgical planning is required to perform such surgeries, which renders the surgery challenging and complex, requiring unique skills and extensive training of the surgeon. In this work, we have demonstrated a new approach of using virtual planning and AM to treat cases

related to deformities of the upper limb. After careful examination of X-ray CT scan data, bone models were designed along with bone plates and guides to ensure proper alignment of bone and best anatomical fit.

The surgical guide used in this work reduces the complexity and time of surgery significantly. This not only help the surgeon to cut the bone properly but also ensures the correct angle and location of cutting of the bone. The hole positions were drilled before cutting the bone in such a way that these hole positions match exactly with the hole positions available in the bone plate after accomodating the planned adjustments of the bone to achieve proper alignment. Moreover, this technique reduces radiation hazard to the health personel during the surgery.

It is known in titanium alloys that bimodal microstructure imparts a good combination of strength, ductility, bending, fatigue life, corrosion, and biocompatibility. We have shown a comparison of these properties in our previous work by selecting a simple design of bone plate made of Ti64 using SLM, subsequently heat-treated, and machined from a wrought alloy of the same composition [15]. It was concluded that heat treated bone plate showed similar performance as in implant fabricated by wrought Ti64. So, in this work, we have assessed the microstructure, phases, and hardness of the prepared implant in AM and HT conditions.

In coclusion, HT bone plate was implaned in patient and deformity was corrected restoring the elbow range of motion. Figure 5 shows the bent and corrected elbow of the patient. Qualitative examination of the elbow of the patient revealed the proper alignment of bone and help him to perform his daily work routine.



Figure 5 Preop and postop images of the elbow of the patient

5. Acknowledgements

The authors gratefully acknowledge funding from the Science and Engineering Research Board (SERB) Government of India (Project CRG/2021/006468-G).

6. References

1. Z.Z. Fang, J.D. Paramore, P. Sun, K.S.R. Chandran, Y. Zhang, Y. Xia, F. Cao, M. Koopman, M. Free, *Int. Mater. Rev.* 63 (2018) 407–459.
2. M. Geetha, A.K. Singh, R. Asokamani, A.K. Gogia, T, *Prog. Mater. Sci.* 54 (2009) 397–425.
3. T.D. Ngo, A. Kashani, G. Imbalzano, K.T.Q. Nguyen, D. Hui, methods , applications and challenges, *Compos. Part B.* 143 (2018) 172–196.
4. S. Liu, Y.C. Shin, *Mater. Des.* 164 (2019) 107552.
5. W.E. Frazier, Metal additive manufacturing: A review, *J. Mater. Eng. Perform.* 23 (2014) 1917–1928.
6. M. Leary, M. Mazur, J. Elambasseril, M. McMillan, T. Chirent, Y. Sun, M. Qian, M. Easton, M. Brandt, *Mater. Des.* 98 (2016) 344–357.
7. C. Yan, L. Hao, A. Hussein, D. Raymont, *Int. J. Mach. Tools Manuf.* 62 (2012) 32–38.
8. C. Qiu, N.J.E. Adkins, M.M. Attallah, *Mater. Sci. Eng. A.* 578 (2013) 230–239.
9. S. Cao, R. Chu, X. Zhou, K. Yang, Q. Jia, C.V.S. Lim, A. Huang, X. Wu, *J. Alloys Compd.* 744 (2018) 357–363.
10. P. Tao, H. xue Li, B. ying Huang, Q. dong Hu, S. li Gong, Q. yan Xu, *China Foundry.* 15 (2018) 243–252..
11. M. Simonelli, Y.Y. Tse, C. Tuck, *Mater. Sci. Eng. A.* 616 (2014) 1–11.
12. L. Facchini, E. Magalini, P. Robotti, A. Molinari, S. Höges, K. Wissenbach, *Rapid Prototyp. J.* 16 (2010) 450–459.
13. H. Galarraga, R.J. Warren, D.A. Lados, R.R. Dehoff, M.M. Kirka, P. Nandwana, *Mater. Sci. Eng. A.* 685 (2017) 417–428.
14. J. Liu, Q. Sun, C. Zhou, X. Wang, H. Li, K. Guo, J. Sun, *Mater. Sci. Eng. A.* 766 (2019).
15. S.K. Gupta, N. Shahidsha, S. Bahl, D. Kedaria, S. Singamneni, P.K.D. V Yarlagadda, S. Suwas, K. Chatterjee, *J. Mech. Behav. Biomed. Mater.* 119 (2021) 104552.
16. R. Sabban, S. Bahl, K. Chatterjee, S. Suwas, *Acta Mater.* 162 (2019) 239–254.
17. S. Selvaraj, J. Dorairaj, M. Shivasankar, *Afr. Health Sci.* 22 (2022) 383–390.

PROPERTY AND MICROSTRUCTURE OF TiTaSn ALLOY FOR MEDICAL DEVICE APPLICATIONS

Bernard Li¹, Kathryn Cho¹, Joe Shaw², Hiroshi Matsushima², Takasumi Kubo²

¹ Medtronic 7000 Central Ave. NE Minneapolis, MN 55432 US

² Nippon Piston Ring Co., Ltd. 5-12-10 Honmachi-Higashi, Chuo-Ku Saitama City, Saitama 338-8503 Japan

TiTaSn alloy is a new beta Ti alloy with high potential for medical device applications. Nippon Piston Ring Corporation developed the alloy with a composition approximating Ti-52Ta-4Sn. It demonstrates good biocompatibility, radiopacity, low modulus and excellent formability. The potential applications of this alloy can be orthopedic, dental, implantable electrical stimulators, stents, etc. Referenced in this paper, the TiTaSn alloy was manufactured as a rod utilizing Beta annealing. This report describes the alloy's mechanical properties, microstructure, and biocompatibility.

Keywords: TiTaSn, beta annealed, cold drawn.

1. Introduction

Due to its biocompatibility and low modulus, Beta Titanium alloy has been studied for years as a biocompatible material for implantable medical device applications [1, 2]. Most beta Titanium alloys do not have radiopacity for implant device applications, whereas TiTaSn alloy has better radiopacity than other beta Titanium alloys and meets the beta Ti alloy properties [3]. TiTaSn alloy has high corrosion resistance, is non-magnetic and is radiopaque, as observed via X-ray imaging. The high content Ta used in this alloy has an atomic number of 73, resulting in good radiopacity. Element Ta was chemically stable and exhibited low in vivo toxicity tracking considerable attention as an inert metallic biomaterial for implantable medical devices. This study describes the TiTaSn rod properties, microstructure, and biocompatibility.

2. Materials and Experiment

Nippon Piston Ring manufactured the TiTaSn 2mm rod using vacuum arc remelting technology. The ingot was hot forged into bars and cold drawn into a 2 mm diameter rod, followed by beta annealing and ageing. The alloy's chemical composition is listed in Table 1. The material was tensile tested by MTS servo-hydraulic universal test machine with an extensometer. The gauge length was 25.4 mm, with a 12.7 mm/min test speed. The TiTaSn rod was cross-sectioned and polished, and its microstructure was analyzed in SEM/EBSD. The SEM equipment utilized was Zeiss Ultra with FEG, equipped with an EDAX OIM EBSD system.

Table 1: Chemical composition of the TiTaSn

Alloy	Ti	Ta	Sn, wt%	Fe, wt%	C, wt%	H, wt%	N, wt%	O, wt%
TiTaSn	Balance	51.2	4.701	0.01	0.005	0.0044	0.003	0.116

3. Results and Discussion

3.1. Tensile properties

Figure 1 is a tensile curve of the TiTaSn rod. The curve shows there is a peak of around 2% strain. Since the TiTaSn rod was aged at a low temperature, it will form a Ω phase. The peak formation may be due to the strengthening of the w phase. After peaking, the curve reaches a plateau, indicating the material has formability. Nippon Piston Ring has produced thin wire with a 20 mm diameter, narrow strips 30 mm thick, and microtubes. Due to the ageing process, the alloy is easy to machine. Table 1 shows the average and standard deviation values of the tensile properties of six samples. The alloy demonstrates a relatively high elastic limit.

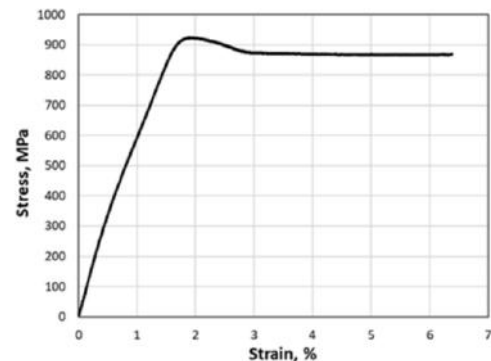


Figure 1. Stress-strain curve of TiTaSn rod. The curve shows a peak at 2% strain.

Table 2 Tensile properties of TiTaSn rod

Sample	UTS, Mpa	TYS, Mpa (0.2% offset)	E, Gpa	Elongation, % (1" gauge)
Average	919.1	626.3	74.2	19.98
SD	5.6	24.5	4.0	3.88

A cyclic tensile test with an extensometer determined the elastic limit of the TiTaSn rod. The test samples were strained to a set value and released (see Fig. 2). The strain was cycled from 0.6 to 1.6% in 0.1% increments. The material was elastic if the recovered

strain was less than 0.02%. Therefore, the elastic range was defined as the highest applied strain when the unload curve with less than 0.02% strain.

Figure 3 shows the resulting cyclic stress-strain curve of the TiTaSn rod with the maximum strain at 1.3%. The plot shows that TiTaSn had a non-linear elastic behavior. The linear range was approximately 0.5%, and the non-linear elastic range was between 0.5 to 1%.

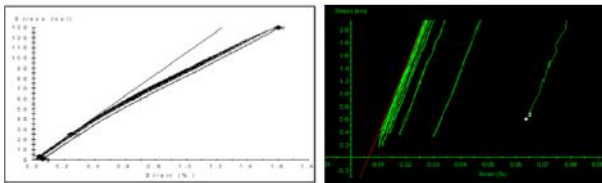


Figure 2. (left) Cyclic stress-strain

Figure 3. (right) Enlarged cyclic tensile curve, the elastic strain limit was 1.3%.

Figure 4 is an enlarged cyclic curve at a lower strain value (lower left corner of Figure 3). The elastic strain limit was 1.2%, and the elastic stress limit was 126 ksi. Figure 4 marked the unload stress-strain curve endpoints, which shows that in a permanent strain (elongation) of less than 0.05%, the highest elastic strain is at 1.2%. The 1.3% strain resulted in a permanent strain above 0.02%.

4. Microstructure

SEM/EBSD analyzed the microstructures of the TiTaSn rod at Medtronic. Transverse direction cross-sections were taken for EBSD analysis. Figure 5 shows the transverse 2 mm TiTaSn rod beta phase grain size image and distribution. The quarter position (QP) location was the quarter of diameter (half radius) location. Colors represent the grain size. The grain size was uniform throughout the diameter of the rod. The bar graph below each grain image shows grain size distribution. Reviewing the QP grain size distributions, the peak grain size for the rod was approximately 11 mm. The distribution of grain size shows a normal distribution. The most prominent grain size is around 20 mm. The rod's small grain size allows the material to be used for thin-wall applications.

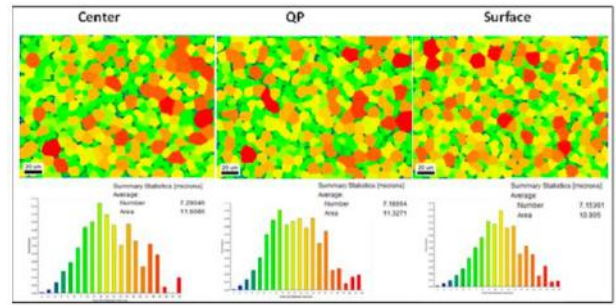


Figure 5. Transverse grain size and grain size distribution of a TiTaSn rod. Blue and green represent small Grains, while red and yellow represent large grains.

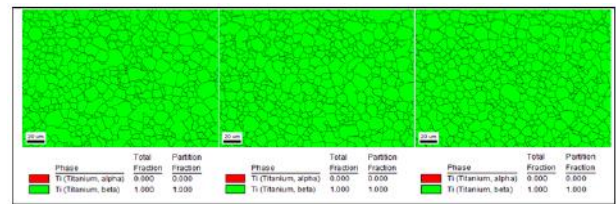


Figure 6. Phase area fraction of 2 mm TiTaSn rod. The alpha phase area fraction is zero.

The alpha phase area fraction was measured by the EBSD method. Figure 6 shows beta phase is 100 per cent. The intensity of texture (the grain orientation the material prefers for TiTaSn rods) was near random, indicating that the TiTaSn rod had a fully recrystallized grain orientation.

5. Biocompatibility

Since TiTaSn contains neither Ni nor Co., It has high corrosion resistance and excellent biocompatibility. Figure 7 shows the cytotoxicity of TiTaSn alloy compared to other alloys used as implantable materials, as the three main elements of the TiTaSn alloy do not dissolve in physiological conditions. Cell mortality was assessed by dissolving low ppm, then added to L929 and U937 cell types at different concentrations. The red lines on the line graph represent Ti-Ta alloy. The chart shows that dissolved material from our Ti-Ta alloy had much less toxicity than other materials tested [4].

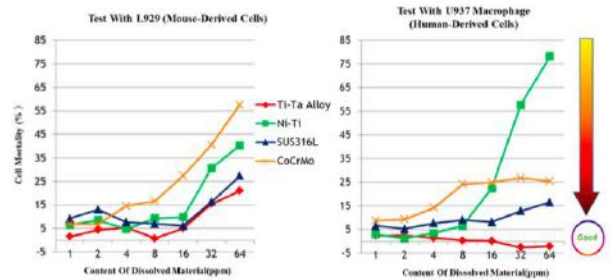


Figure 7. shows that The Cytotoxicity of Ti-Ta alloy is much lower than existing biomaterials because it is Ni and Co free alloy. It exhibits no Cytotoxicity in a human- derived cell.

6. Radiopacity

As a result of the high atomic elements and Ta and Sn concentration, the TiTaSn alloy shows higher radiopacity than NiTi, CoCrMo and 316L [5, 6]. In this study, a ring component of TiTaSn was compared with the PtIr ring with Fluoro X-ray imaging. Figure 8 shows Fluoro X-ray images of two materials: PtIr (dark) and TiTaSn (light grey). Figure 9 shows the contrast of individual TiTaSn rings, which has a lower contrast than PtIr— demonstrating good visibility under Fluoro X-ray. In general, under Fluoro X-ray imaging, TiTaSn alloy revealed good radiopacity.

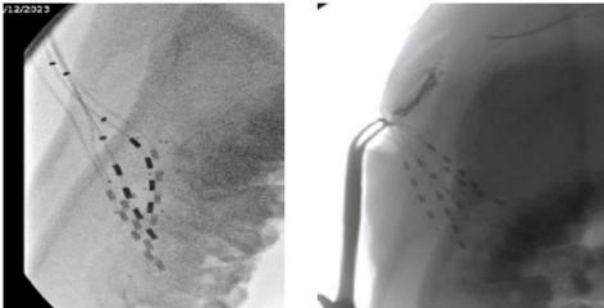


Figure 8 compares the Fluoro X-ray image of PtIr and TiTaSn rings.

7. Summary

TiTaSn beta annealed and aged rod high strength and ductility. After beta annealed and aged, the alloy had a high elastic limit. EBSD analysis showed that the TiTaSn rod has a uniform small grain size, allowing for thin wall applications. The alloy has good formability enabling machining, strip rolling, wire and tube drawing. The alloy possesses better biocompatibility compared to NiTi, CoCrMo and 316L materials. The Fluoro X-ray imaging study shows TiTaSn alloy has comparable radiopacity to Pt based alloy.

8. Acknowledgements

Thanks to Medtronic and NPR providing support on the study of TiTaSn alloy.

9. References

1. Rack, H.J.; Qazi, J.I. Titanium alloys for biomedical applications. *Mater. Sci. Eng. C* 2006, 26, 1269–1277.
2. Niinomi, M. Recent metallic materials for biomedical applications. *Metall. Mater. Trans. A* 2002, 33, 477–486.
3. US10669613B2, Titanium Alloy, Shunsuke Takeuchi; Yoshiki Ishikawa; Takasumi Kubo; Shin Ishida; Hiroki Takahashi; Masafumi Morita; Masahito Miki
4. Masahito Miki and Masafumi Morita: “Evaluation of the Biocompatibility of a Ti-Ta-Sn Alloy Using Cell Cultures,” *Materials Transactions*, Vol. 56, No. 7 (2015) pp. 1087 to 1091 ©2015 The Japan Institute of Metals and Materials
5. M. Miki, M. Morita, S. Takeguchi, Y. Ishikawa and E. Tajima: *Mater. Sci. Techn. Japan* 51 (2014) 117- 121.
6. Y. Ishikawa, T. Kubo, T. Takahashi, S. Takeguchi, M. Miki and M. Morita: *Mater. Sci. Techn. Japan* 51 (2014) 217-221.

LASER POWDER BED FUSION OF A NOVEL TITANIUM ALLOY FOR MEDICAL APPLICATIONS

Fabian Haase, Carsten Siemers, Joachim Rösler

Technische Universität Braunschweig, Institute for Materials Science, Langer Kamp 8, 38106 Braunschweig, Germany

Additive manufacturing e. g. via laser powder bed fusion (LPBF) has gained increased interest regarding implant or osteosynthesis product manufacturing, since complex, near-net shaped, and, possibly, individually tailored parts can be directly produced on the basis of a computer model. However, LPBF-printed conventional titanium alloys are usually textured. Anisotropic mechanical properties are, therefore, presumed. Additionally, LPBF parts could exhibit substantial porosity in the as printed state if the process parameters are poorly chosen. Both is usually unwanted and limits or prevents the usage of additively manufactured titanium parts in medical applications. Therefore, in the present study, LPBF of the $(\alpha+\beta)$ -alloy Ti-0.66O-0.5Fe-0.09C-2.1Mo, recently presented by the authors for use in medical applications regarding conventional product manufacturing, and the influence of 0.05 wt.% boron, added as elemental powder in order to further increase constitutional supercooling, are investigated regarding solidification, microstructure, and the resulting texture. First, a process window for LPBF-printing of the former alloy via a design of experiments was established and high-density cubical samples were achieved in the as printed condition using this method. X-ray diffraction results suggest that both alloys do not exhibit a substantial quantitative anisotropy in the as printed condition. However, the boron-modified alloy exhibits a higher number of prior β -grains as well as more equiaxed β -grains in the as printed condition. The modified alloy is, therefore, promising to achieve more isotropic mechanical properties together with an enhanced biocompatibility compared to conventional $(\alpha+\beta)$ -titanium alloys for medical applications, but the chemical composition has to be further tailored to reduce the notch sensitivity and crack formation susceptibility of the alloy.

Keywords: LPBF, alloy design, process parameters, microstructure, texture, titanium

1. Introduction

Titanium and titanium alloys, conventionally or additively processed, are extensively used as biomaterial for implant or osteosynthesis applications due to, amongst others, their biocompatibility and corrosion resistance [1, 2]. Within this field, additive manufacturing e.g. via laser powder bed fusion (LPBF) has become attractive, since LPBF allows the near-net shaped fabrication of complex geometries and, possibly, of implants individually tailored to patients [2, 3]. However, during LPBF-printing, a β fibre texture or columnar (prior) β -grains usually evolve regarding conventional titanium alloys due to the solidification conditions present [3–6] with a concomitant texture after the (martensitic) β to α transformation due to the Burgers relationship [4]. Consequently, anisotropic mechanical properties are usually expected [2–6]. In order to get more isotropic mechanical properties, equiaxed β -grains have to be present [3, 5, 6]. Different factors to promote this columnar to equiaxed transition (CET) are described in the literature [5, 6]. Amongst others, potent solidification nuclei are needed within the melt pool as well as suitable alloying elements, which lead to a rapid build-up of the constitutionally supercooled zone (high growth restriction factor) [5, 6]. Both has been extensively studied in the past years to obtain LPBF-printed titanium alloys with equiaxed grains and lower anisotropy [6].

In the present study, LPBF-printing of Ti-0.66O-0.5Fe-0.09C-2.1Mo, an $(\alpha+\beta)$ -alloy recently presented by the authors as potential, more biocompatible

alternative for Ti-6Al-4V (ELI) [7], and the influence of a small amount of boron on the microstructure and texture are investigated. Ti-0.66O-0.5Fe-0.09C-2.1Mo was originally developed for conventional implant manufacturing [7], but since it contains higher amounts of oxygen, carbon and iron, which increase constitutional supercooling [5, 6], it is also investigated regarding LPBF-printing in order to obtain a more biocompatible titanium alloy with lower anisotropy. Boron is known as a potent growth restriction solute providing constitutional supercooling [5, 6, 8] and has already been investigated in detail regarding its influence on conventionally and additively processed titanium alloys, as summarized e.g. by Zhang et al. [6] and Singh and Ramamurty [8]. In the present study, first, a design of experiments is used to establish a process window as well as optimized process parameters for LPBF-printing of Ti-0.66O-0.5Fe-0.09C-2.1Mo to minimize porosity. For this alloy as well as for a powder mixture consisting of pre-alloyed Ti-0.66O-0.5Fe-0.09C-2.1Mo powder with 0.05 wt.-% elemental boron powder, specimens were then printed and analysed regarding their microstructure and texture. Additionally, results of tensile tests regarding Ti-0.66O-0.5Fe-0.09C-2.1Mo will be briefly discussed.

2. Methods

2.1. LPBF-printing

Ti-0.66O-0.5Fe-0.09C-2.1Mo EIGA-atomized, raw powder was obtained from GfE Metalle und Materialien GmbH, Germany, with a D50 and D90 value of approx. 32 μm and 64 μm , respectively, using the same

ingot as in [7]. Before the first and after each use, the powder was sieved with a mesh width of 80 μm under protective argon gas. For process window determination, a Doehlert Design [9] was used analogous to the study of Perevoshchikova et al. [10]. The hatch distance, laser power, and scanning speed were varied and the influence on the porosity was determined by printing cubical samples with dimensions 10 x 10 x 10 mm^3 (excluding support structures) on a SLM[®]125 (SLM Solutions Group AG, Germany) LPBF machine using a rotating zig-zag scanning strategy (limitation window: 90°; angle increment: 67°). The layer thickness, gas flow velocity, and temperature of the titanium substrate plate were set to 30 μm , 6.5 m/s (measured within the piping), and 200°C, respectively. After printing, all specimens were sectioned parallel to the building and gas flow direction, hot embedded, ground, polished, and cleaned according to standard metallographic specimen preparation procedures. The porosity was subsequently measured with Fiji software [11] using 9 images for each specimen obtained with a light microscope (ZEISS Axio Imager.M2m) with 100x magnification operated in bright field mode. The border of the specimens was excluded within these analyses in order to eliminate effects of the border process parameters, which can be set independently. Although careful cleaning, small residual Ethanol spots might have remained on the specimens' surfaces prior to taking images, which have led to a certain uncertainty regarding porosity measurements. In order to gain a functional interrelationship (response surface) between the porosity and the hatch distance, laser power, and scanning speed, a multiple linear regression (ordinary least squares) was performed (regarding the coded values of the process parameters, see Doehlert Design [9]). Analogous to for example Perevoshchikova et al. [10], a quadratic function was used containing linear and quadratic terms for each coded process parameter, each product of two coded process parameters, and a constant. The established equation was afterwards transformed to describe the relative density dependant on the three process parameters. All mathematical calculations and the (graphical) evaluation were performed with MATLAB[®] software [12] using a self-written script and existing functions and toolboxes where possible. After establishing the process window, one combination of these three process parameters leading to a low porosity was determined, termed "optimized process parameters" in the following, leading to an energy density of approx. 51 J/ mm^3 . Several cubical specimens with same geometry were printed using these settings (same scanning strategy, layer thickness etc. as already described) and two of them, placed at opposite ends of the

substrate plate regarding gas flow direction during LPBF printing, were subsequently analysed in terms of their porosity.

In order to study the influence of boron on the microstructure, sieved (reused) Ti-0.66O-0.5Fe-0.09C-2.1Mo powder was mixed with approx. 0.05 wt.% elemental boron powder of purity 99.9%. The boron powder initially had a particle size of approx. 2 μm according to the certificate of analysis. Several specimens were printed using this powder mixture, among them one processed with the optimized process parameters of Ti-0.66O-0.5Fe-0.09C-2.1Mo.

2.2. *Microstructure and texture analysis*

Printed specimens were first sectioned parallel to the building and gas flow direction. For microstructure and phase analysis via x-ray diffraction (XRD), one half was hot embedded, ground, polished and etched using standard metallographic specimen preparation procedures. The other half was manually ground with SiC grinding paper with a grit size of P800 and P2500 and used for XRD texture measurements. Microstructure analysis was performed using a tabletop SEM microscope (Hitachi TM3000) equipped with a BSE detector operated in COMPO mode. Phase analysis, also used for the evaluation of the texture degree, and pole figure measurements were performed with a GE XRD 3003 PTS diffractometer ($\text{CuK}\alpha$ -radiation). For phase analysis, specimens were identically oriented and measured regarding a Bragg angle of 34° - 80° with a step with of 0.005° and an integration time of 4 s in Bragg-Brentano setup (line focus of the x-ray tube). A background correction and visualization was performed using OriginPro software [13]. CMPR software [14] and the PDF2 database, release 2005, was used for phase analysis. Pole figures were obtained for the $\{10\bar{1}0\}$, $\{0002\}$, and $\{10\bar{1}1\}$ lattice planes including measurements of the background radiation using a 1 mm pinhole collimator and a receiving slit of 6 mm. The Bragg angle was set to the centre of gravity of the respective peak, measured beforehand using the same beam path and a tilt and rotation angle of 0°. Background correction and visualization was performed with RayfleX software, program ANALYZE [15] and the MTEX toolbox [16] version 5.1.1 for MATLAB[®] [12], respectively.

3. Results and discussion

3.1. *Process parameter optimization*

The 13 specimens printed as part of the Doehlert Design exhibit an average porosity between approx. 0.01% and 1.7%. Some of them exhibit cracks originating from the specimens' border or support structures, which

are not included in the porosity measurements. Only three specimens show an average relative density of less than 99.9%, which suggests that the alloy exhibits a process window, in which it can be LPBF-printed without substantial negative impact on relative density. This finding is further supported by the established response surface, which is depicted in Fig. 1 (a) in terms of the relative density as a function of the scanning speed and laser power for a hatch distance of 0.1 mm. The R^2 value of the performed regression is approx. 0.99. However, only the p-values of the coefficients of the linear and quadratic term of the scanning speed are small (below 0.005), whereas the other values are between approx. 0.16 and 0.99. Since these values indicate whether the corresponding term has a significant effect on the response [17], the influence of the hatch distance and laser power on the porosity are, therefore, not significant within the model. The calculated stationary point of the response surface is a saddle point at a negative laser power with a calculated relative density of 100%. This shows that the response surface cannot describe the conditions beyond the studied experimental domain. For example, porosity due to lower laser power (insufficient melting) is not adequately represented within the model.

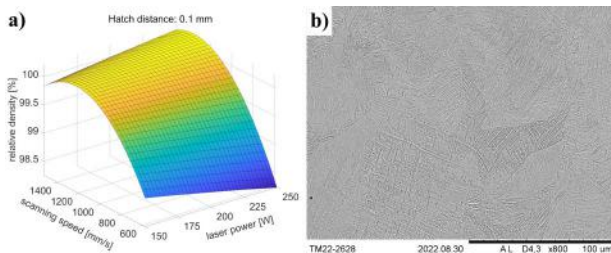


Figure 1: LPBF of Ti-0.66O-0.5Fe-0.09C-2.1Mo: a) Relative density as a function of the scanning speed and laser power for a hatch distance of 0.1 mm, b) As printed microstructure (SEM image, BSE detector) in the centre of the specimen

Despite of these limitations, a set of optimized process parameters with an energy density of approx. 51 J/mm^3 was selected within the studied experimental domain on the basis of the established response surface and several cubical specimens were printed with these settings. Two exemplarily analysed specimens exhibited a porosity of approx. 0.02% and 0.03% (average values) with an empirical standard deviation of approx. 0.01% and 0.04%, respectively. Cracks at the specimens' border or support structures are, again, not included in these results. However, one of these samples contained one rather large porosity with irregular shape at the top, which is also not represented in the determined porosity. It is reasonable to suggest that this isolated defect is not caused by the use of unsuitable process parameters. Nevertheless, subsequently printed tensile specimen

blanks partly exhibited lack of fusion defects. Consequently, other parameters not included in the experimental design, for example the length of the specimens' borders and their orientation regarding the gas flow direction as well as their process parameters, also play an important role in terms of the achievable porosity.

3.2. Microstructure and texture analysis

3.2.1. Ti-0.66O-0.5Fe-0.09C-2.1Mo

Fig. 1 (b) shows the microstructure of Ti-0.66O-0.5Fe-0.09C-2.1Mo in the as printed state (optimized process parameters) in the centre of the specimen with the building direction pointing upwards. As can be seen, the alloy exhibits a fine martensitic microstructure. Prior β -grain boundaries are not always clearly visible, but do show a columnar orientation along the building direction of at least some prior β -grains. Their size varies noticeably with prior β -grains exhibiting a length or width of more than $100 \mu\text{m}$. However, there also exist much finer grains. Despite of the poor identifiability of prior β -grain boundaries, some equiaxed prior β -grains are visible in the region at the transition from the support structures (printed with a layer thickness of $60 \mu\text{m}$ and, partly, different laser power and speed) to the specimen. In these cases, structures were directly printed on top of the powder bed or close to unmolten powder. It is therefore reasonable to assume that these equiaxed β -grains formed due to different cooling conditions, possibly characterized by a lower temperature gradient promoting an equiaxed-dendritic solidification due to heat dissipation across the powder bed. Regarding the last scan tracks at the top of the specimen, prior β -grain boundaries are not clearly visible, so that no clear conclusions are possible regarding the solidification of individual melt pools.

Fig. 2 (a) shows the measured diffractogram of the same sample in the as printed state after background correction together with ideal peak positions and intensities of the α -phase according to PDF2 database (entry number 441294). The ideal intensity of the main α -peak was arbitrarily set to 100 cps. All peaks of the diffractogram consist of the superimposition of the corresponding $K_{\alpha 1}$ - and $K_{\alpha 2}$ -peak, since a large receiving slit had to be used in order to obtain enough intensity. Neglecting this influence on the intensity ratios, it can be seen that the measured peak intensity ratios show a comparable good agreement with the ideal ratios according to database. Consequently, it is reasonable to conclude that the sample does not exhibit a substantial quantitative anisotropy in the as printed state. The incomplete $\{10\bar{1}0\}$, $\{0002\}$, and $\{10\bar{1}1\}$ pole figures, shown in Fig. 2 (b) after background correction for a

plane containing the building (BD) and transverse (TD) direction with TD being the opposite of the gas flow direction, do show poles, but none of these are considerably strong or sharp according to the measured intensities. However, further investigations are necessary for a quantification of the texture degree, since, amongst others, residual stresses as well as defocussing effects had an angle-dependant influence on the measured intensity.

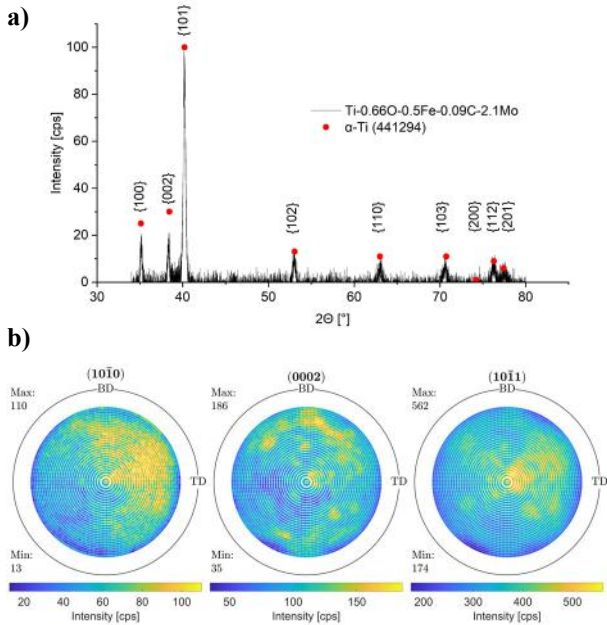


Figure 2: Ti-0.66O-0.5Fe-0.09C-2.1Mo (optimized process parameters) in the as printed state: a) Diffractogram after background correction together with ideal peak positions and intensities of the α -phase according to PDF2 database, b) Incomplete pole figures after background correction. The orientations of the building (BD) and transverse (TD) direction are indicated.

Despite of these promising results, this as well as other samples of the alloy exhibit cracks in the as printed condition, which originate from the surface, suggesting a high strength level of the alloy in this condition and high residual stresses. One specimen printed with optimized process parameters exhibits an average hardness of approx. 431 HV10. Moreover, during initial tensile tests in the heat-treated and milled condition, fracture occurred without significant macroscopic plasticity. Fracture surface analysis, exemplarily performed on two specimens, indicated a microscopic brittle as well as ductile fracture. Regarding one analyzed specimen, the crack originated at a lack of fusion defect and initially mostly propagated microscopically brittle and subsequently transitioned to a ductile propagation mode. Since it has already been established that a high oxygen content leads to embrittlement in titanium [18, 19], specimen failure is probably caused by stress concentrations (notches) in combination with a high notch sensitivity of the alloy and remaining residual stresses.

Consequently, the chemical composition has to be further tailored to achieve sufficient ductility.

3.2.2. *Ti-0.66O-0.5Fe-0.09C-2.1Mo-0.05B*

With the addition of boron, while retaining the same process parameters, the microstructure changed substantially, as can be seen in Fig. 3, which shows the microstructure (SEM image, BSE detector) in the as printed state in the centre of the specimen with the building direction pointing upwards. Martensite as well as former β -grain boundaries are clearly visible as well as some laser tracks. During etching of the metallographic specimen preparation, there was probably an increased corrosive attack along β -grain and some melt pool boundaries leading to pitting corrosion. Compared to Ti-0.66O-0.5Fe-0.09C-2.1Mo, see Fig. 1 (b), the size of former β -grains decreased substantially and there are also some isolated equiaxed-like grains present. However, prior β -grains are still mostly elongated in the building direction or in the solidification direction of individual laser tracks. There are no visible indications of TiB precipitations in the microstructure as well as in a performed XRD phase analysis of a differently printed sample. However, due to the assumed strong segregation of boron during solidification and the very low solubility of boron in α - and β -Ti [20], the presence of TiB precipitations cannot be excluded. It has to be noted that there seem to be unmolten boron particles present within the sample as well as spots with an increased corrosive attack, suggesting a locally different boron content. The latter is further supported by the SEM-analysis performed on the mixed powder, which suggests the formation of agglomerates of boron particles and, possibly, of local boron accumulations as well as spots with fewer particles. Consequently, it might be possible that the boron content is not evenly distributed in the sample, which might explain the uneven corrosive attack visible in Fig. 3.

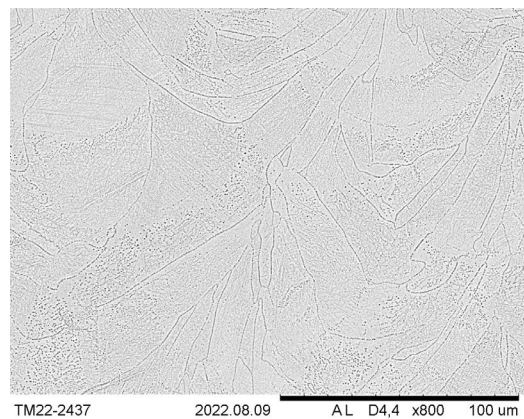


Figure 3: As printed microstructure (SEM image, BSE detector) of Ti-0.66O-0.5Fe-0.09C-2.1Mo-0.05B in the centre of the specimen

In terms of the printed support structures, the specimen numbering printed on top of the specimen, and the last laser tracks, the specimen exhibits, in spots, several equiaxed prior β -grains. Fig. 4 (a) (SEM image, BSE detector) shows this for a region within the printed support structures, which were printed with a layer thickness of 60 μm and, partly, with a different laser power and scanning speed. Within this particular area, several equiaxed prior β -grains are present. Therefore, in these cases, the solidification must have been different compared to the centre of the specimen, see Fig. 3, promoting an equiaxed-dendritic solidification with the formation of many equiaxed β -grains. Several reasons for this are possible, for example a heat transfer through the powder bed resulting in a lower temperature gradient. The microstructure of the laser tracks printed lastly is similar to Fig. 3, showing mostly elongated prior β -grains oriented in building direction or the solidification direction of the laser tracks. However, occasionally, there are equiaxed prior β -grains present at the top of solidified melt pools, as can be seen in Fig. 4 (b).

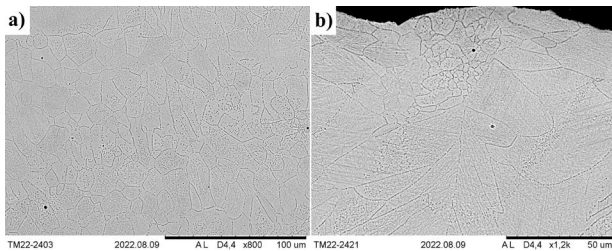


Figure 4: As printed microstructure (SEM image, BSE detector) of Ti-0.66O-0.5Fe-0.09C-2.1Mo-0.05B: a) region within the printed support structures, b) laser track printed lastly

Fig. 5 (a) shows the diffractogram of Ti-0.66O-0.5Fe-0.09C-2.1Mo-0.05B in the as printed state after background correction, but for a specimen printed with different process parameters. Ideal peak positions and intensities of the α -phase according to PDF2 database with the main α -peak set to 100 cps are indicated. Similar to Ti-0.66O-0.5Fe-0.09C-2.1Mo, neglecting the $K_{\alpha 1}$ - and $K_{\alpha 2}$ -peak superimposition, there is visually a comparable good agreement between the measured peak intensity ratios and the ratios according to database. Therefore, a strong anisotropy in the as printed state is not expected. This is, again, supported by the incomplete pole figures displayed in Fig. 5 (b) of the sample printed with optimized process parameters, since no sharp, very pronounced poles are visible. However, as already described, further investigations are needed for a more precise description of the texture or texture degree.

Analogous to the base alloy, specimens of Ti-0.66O-0.5Fe-0.09C-2.1Mo-0.05B exhibit cracks in the as

printed condition, but to a much higher extent. Regarding the specimen printed with optimized parameters of the base alloy, branched cracks are also present, suggesting a crystallographic crack propagation. Although the crack propagation path cannot be traced regarding microstructural features, it seems that the path followed at least partly prior β -grain boundaries. Consequently, the latter might be microstructural vulnerabilities.

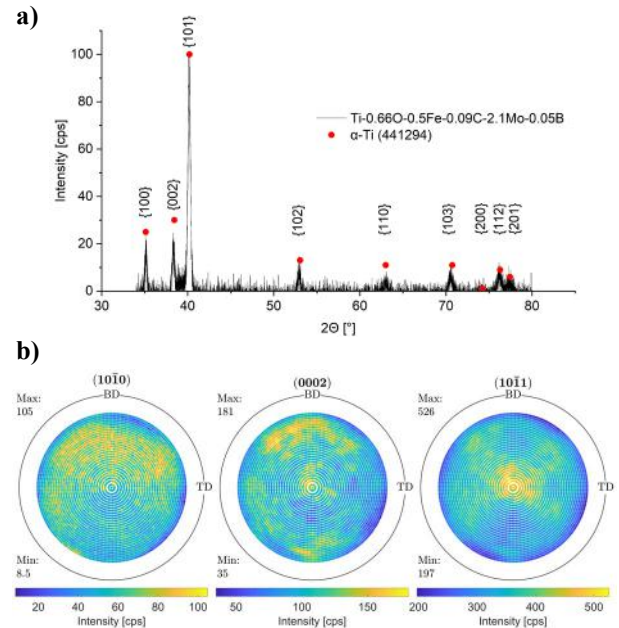


Figure 5: Ti-0.66O-0.5Fe-0.09C-2.1Mo-0.05B in the as printed state: a) Diffractogram (non-optimized process parameters) after background correction together with ideal peak positions and intensities of the α -phase according to PDF2 database, b) Incomplete pole figures (optimized process parameters) after background correction. The orientations of the building (BD) and transverse (TD) direction are indicated.

Fig. 4 (b) indicates that a columnar to equiaxed transition (CET) seem to happen at the top of few melt pools. As described for example by StJohn et al. [5], it can be assumed that these zones had been mostly re-melted during scanning of subsequent powder layers leading to mainly columnar prior β -grains in the sample with only isolated equiaxed-like grains, as can be seen in Fig. 3. The precise reason for the CET remains unknown in the present study. Since the CET only occurred occasionally regarding few laser tracks, it might be the result of a local boron enrichment, whose possibility was described earlier. Generally, either the amount of constitutional supercooling was increased sufficiently to activate existing solidification nuclei within the liquid, or new nuclei with lower required undercooling were introduced [5, 6]. In case of the former, the results would suggest that the increased amount of oxygen, carbon, and iron in the alloy compared to conventional titanium alloys in combination with the addition of a low amount of boron

would be sufficient to, at least occasionally, facilitate an equiaxed-dendritic solidification during LPBF.

Despite of this, more equiaxed prior β -grains might not be strictly necessary in order to obtain a comparable low anisotropy in the as printed state, according to the results presented. Therefore, further studies should primarily focus on obtaining good mechanical properties with higher ductility, lower notch sensitivity, and lower crack formation susceptibility (lower strength of the alloy). In an initial step, the oxygen content of the alloy should be reduced due to its detrimental effects on mechanical properties, as already described. However, since oxygen promotes constitutional supercooling [5, 6], it is subject to further studies whether this adversely affects solidification behaviour and promotes texture.

4. Summary

The present study indicates that Ti-0.66O-0.5Fe-0.09C-2.1Mo, especially with the addition of 0.05% boron, is promising to achieve more isotropic properties after LPBF-printing together with an enhanced biocompatibility compared to conventional biomedical ($\alpha+\beta$)-alloys. The addition of boron led to a significant refinement of prior β -grains. Additionally, equiaxed prior β -grains are, amongst others, occasionally present at the top of solidified laser tracks printed lastly. However, the microstructure still mostly consists of columnar or elongated prior β -grains, together with few isolated equiaxed-like grains. Nevertheless, the chemical composition has to be further tailored to achieve a lower notch sensitivity and crack formation susceptibility of the alloy.

5. Acknowledgements

This study was conducted within project IGF 21671 N of the AiF Arbeitsgemeinschaft industrieller Forschungsvereinigungen "Otto von Guericke" e.V., supported by the Federal Ministry for Economic Affairs and Climate Action on the basis of a decision by the German Bundestag, which is gratefully acknowledged. Furthermore, the authors would like to thank S. Mohamed of the Institute for Materials Science and J. Fritzen of the DECHEMA Research Institute, Frankfurt, Germany, for their help regarding this study.

6. References

1. F.H. (Sam) Froes (2018). In: F.H. Froes, M. Qian (eds) Titanium in Medical and Dental Applications. Woodhead Publishing, Duxford, United Kingdom, pp 3–21
2. E. Davoodi, H. Montazerian, A.S. Mirhakimi, M. Zhanmanesh, O. Ibadode, S.I. Shahabad, R. Esmailizadeh, E. Sarikhani, S. Toorandaz, S.A. Sarabi, R. Nasiri, Y. Zhu, J. Kadkhodapour, B. Li, A. Khademhosseini, E. Toyserkani, *Bioactive Materials* 15 (2022) 214–249
3. T. DebRoy, H.L. Wei, J.S. Zuback, T. Mukherjee, J.W. Elmer, J.O. Milewski, A.M. Beese, A. Wilson-Heid, A. De, W. Zhang, *Progress in Materials Science* 92 (2018) 112–224
4. P. Barriobero-Vila, J. Gussone, A. Stark, N. Schell, J. Haubrich, G. Requena, *Nature Communications* 9 (2018) 3426
5. D.H. StJohn, S.D. McDonald, M.J. Birmingham, S. Mereddy, A. Prasad, M. Dargusch, *Key Engineering Materials* 770 (2018) 155–164
6. D. Zhang, A. Prasad, M.J. Birmingham, C.J. Todaro, M.J. Benoit, M.N. Patel, D. Qiu, D.H. StJohn, M. Qian, M.A. Easton, *Metallurgical and Materials Transactions A* 51 (2020) 4341–4359
7. F. Haase, C. Siemers, J. Rösler, *Journal of Materials Research* 37 (2022) 2589–2603
8. G. Singh, U. Ramamurty, *Progress in Materials Science* 120 (2021) 100815
9. D.H. Doehlert, *Journal of the Royal Statistical Society. Series C (Applied Statistics)* 19 (1970) 231–239
10. N. Perevoshchikova, J. Rigaud, Y. Sha, M. Heilmair, B. Finin, E. Labelle, X. Wu, *Rapid Prototyping Journal* 23 (2017) 881–892
11. J. Schindelin, I. Arganda-Carreras, E. Frise, V. Kaynig, M. Longair, T. Pietzsch, S. Preibisch, C. Rueden, S. Saalfeld, B. Schmid, J.-Y. Tinevez, D.J. White, V. Hartenstein, K. Eliceiri, P. Tomancak, A. Cardona, *Nature Methods* 9 (2012) 676–682
12. MATLAB (2022) version 9.12 (R2022a). The MathWorks, Inc., Natick, MA
13. OriginPro (2023) version 2023. OriginLab Corporation, Northampton, MA, USA
14. B.H. Toby, *Journal of Applied Crystallography* 38 (2005) 1040–1041
15. RayfleX, program ANALYZE (2005) version 2.363. GE Inspection Technologies GmbH, Ahrensburg, Germany
16. F. Bachmann, R. Hielscher, H. Schaeben, *Solid State Phenomena* 160 (2010) 63–68
17. The MathWorks, Inc. (2022) Statistics and Machine Learning Toolbox Documentation, for MATLAB version R2022a. The MathWorks, Inc., Natick, MA
18. A. Amherd Hidalgo, T. Ebel, W. Limberg, F. Pyczak, *Key Engineering Materials* 704 (2016) 44–52
19. T. Ebel, O.M. Ferri, W. Limberg, M. Oehring, F. Pyczak, F.-P. Schimansky, *Key Engineering Materials* 520 (2012) 153–160
20. J.L. Murray, P.K. Liao, K.E. Spear (1986). In: T.B. Massalski (ed) Binary Alloy Phase Diagrams, 1st edn., volume 1. American Society for Metals, Metals Park, Ohio

ADDITIVELY MANUFACTURED Ti2Mo FOR BIOMEDICAL APPLICATIONS: SURFACE ENGINEERING AND CORROSION PROPERTIES

Julian P. Zander¹, Stephan Lederer¹, Wolfram Fürbeth¹

¹ DEHEMA Research Institute, Frankfurt am Main, GER.

Additive manufacturing allows the fast production of small and complex parts with minimum waste for biomedical applications made of titanium alloys. However, the cytotoxicity of certain elements being widely used in these alloys has become a concern, initiating the development of new alloys avoiding their use as alloying elements. In this publication, surface engineering techniques like blasting and plasma electrolytic polishing have been applied to a new Ti2Mo alloy obtained by Selective Laser Melting (SLM) in order to enhance its surface properties. First aim of such surface engineering processes is to develop standardized surfaces for additively manufactured parts, comparable to conventionally produced parts. Residual stresses that arise due to the additive manufacturing process are examined as well as their potential impact on the mechanical and corrosion properties of the alloys. Via suitable heat treatment residual stresses can be lowered and adjusted. Additionally, the corrosion properties are determined using potentiodynamic polarization and tribocorrosion testing.

Keywords: Titanium alloy, additive manufacturing, SLM, surface engineering, corrosion properties, residual stress analysis.

1. Introduction

Among commonly used metals in the biomedical field, titanium (Ti) alloys possess favourable mechanical properties, biocompatibility, and corrosion resistance, making them an ideal choice for the fabrication of medical implants [1-2]. One of the most commonly used titanium alloy for biomedical implants is Ti6Al4V [2]. However, this alloy contains aluminium and vanadium, both cytotoxic elements that can potentially cause adverse reactions in the human body [3]. Hence, in the biomedical field the demand for new titanium alloys, which are cytotoxic-free as well as suitable for AM processing has been increasing. The titanium-molybdenum alloy Ti2Mo is a promising candidate for these purposes, offering an optimal combination of mechanical strength and biocompatibility [4].

Additive manufacturing (AM) has rapidly evolved into a major technological breakthrough in the medical industry, offering unlimited possibilities to produce implants fast and with less waste [5]. Selective Laser Melting (SLM), one of the most widespread AM techniques, is a powder bed fusion (PBF) technique that uses a high-intensity laser beam to selectively melt and solidify metallic powder layer by layer. The microstructure of the printed metal parts varies with the applied processing parameters, such as laser power density and scanning velocity, which significantly influence the mechanical and physical properties of the final product. SLM can develop complex-shaped, small structures with tight tolerances, resulting in implants that minimize the risk of post-operative complications [8-9].

The mechanical properties of SLM-manufactured Ti2Mo are superior to Ti6Al4V and cp-Ti, with a yield strength of 1006 MPa, ultimate tensile strength of 1016 MPa, and an elongation at break of

17 % [4], making it an excellent choice for load-bearing applications.

This study focuses on the surface engineering of AM Titanium alloys, in specific Ti2Mo, to generate smooth surfaces, which can be a good basis for coatings and functional structuring. Blasting with alumina removes residual particles from the AM parts and guarantees a uniformly rough surface, even for complex structures. With plasma electrolytic polishing (PEP) the micro roughness is minimized, so that the surface is smoothed [10-11]. Moreover, residual stresses are determined non-destructively by XRD and the $\sin^2\psi$ -method [12-13] in the "As Received" (AsRe), as well as in the annealed, blasted and plasma polished condition. Since the alloy Ti2Mo has been developed for biomedical applications, corrosion tests, like potentiodynamic polarization and tribocorrosion, are carried out in simulated body fluid at body temperature (37 °C).

2. Materials and Methods

2.1. Additive Manufacturing and sample preparation

Samples are additively manufactured by the Selective Laser Melting (SLM) process. Using Design of Experiments (DoE), the parameters of the process were optimized, to generate dense parts. The standard sample size was 20×15×4 mm (w×h×d) after the support structure had been removed. For the AM process, cp-Ti grade 2 and Ti2Mo (Ti 0.44O 0.08C 0.50Fe 2.00Mo) [4] powder was used. As a comparison, conventionally produced (cast) samples with the same compositions were tested. All samples were cleaned ultrasonically in ethanol and then dried with compressed air. Cleaning steps were carried out after every surface treatment. In order to lower residual stresses and transform the alpha-martensitic into an α or $\alpha+\beta$ microstructure, the AM samples were annealed for 90 minutes using an argon atmosphere in a

tube furnace at 900 °C and/or 700 °C followed by furnace cooling.

2.2. Surface engineering

2.2.1. Blasting

Samples were blasted in the blasting machine “Sigg TR60” at 3 bar compressed air. As a blasting material high-class corundum grit with a particle size distribution of 63-109 μm (according to the manufacturer) was used. Samples were blasted until a uniform surface in colour forms, at least 30 s for each side.

2.2.2. Plasma electrolytic polishing (PEP)

The surface of the AM parts was polished at a voltage of 300 V using an ITECH AC/DC power supply (IT7809-350-90). The current density was set to about 0.1 A/cm². With a heating plate the electrolyte temperature was set to 85 °C. During the PEP process the temperature rises up to 96 °C. The aqueous electrolyte consisted of NaF (1.5 %–3.0 %) and NH₄Cl (1.5 %–3.0 %) and was stirred during the process. The influence of the process time was tested between 5 to 10 minutes. Parameters were determined using a ‘Design of Experiments’ (DoE) approach targeting a minimum surface roughness (Ra).

2.3. Corrosion investigations

2.3.1. Potentiodynamic polarization

Potentiodynamic polarization tests were realized in simulated body fluids (Hanks’ solution) at 37 °C (body temperature). Temperature was set inside a heating chamber. In total, four cells equipped with a conventional three electrode setup and a volume of 200 ml each were used. The electrolyte was stirred at 400 rpm. Samples were countered against the cell opening (exhibiting an area of 0.28 cm² to the electrolyte) and connected as the working-electrode (WE) with a brass screw. Like the WE, the reference- (RE, calomel +245 mV) and counter-electrode (AE, Platinum 3-5 cm²) were connected to the OrigaFlex potentiostat. Data was analysed with the OrigaMaster5 software. Each test sequence involved a measurement of the open circuit potential (OCP) for at least 20 h followed by potentiodynamic polarization from -200 mV to +3500 mV vs. OCP.

2.3.2. Tribocorrosion

Tribocorrosion tests were realized in simulated body fluid (Hanks’ Solution) at 37 °C in a self-constructed cell (three electrode setup). The exposed sample area (WE) was 3.5 cm². Temperature was set with a flow system connected to a thermostat (Lauda ECO E4 Gold). Electrodes were connected to the OrigaFlex potentiostat. Data was analysed with the OrigaMaster5

Software. Open circuit potential (OCP, at least 20 h) and polarization resistance measurements (-20 mV to +20 mV against OCP) were performed in this setup. Tribometry tests were implemented using a Nanovea TRB (T-16-0148) pin on disc setup. The wear track of 5 mm (transversal friction) was rubbed with an alumina ball (\varnothing 6 mm) at 1 Hz frequency for a sliding distance of 40 m.

2.4. Materials characterization

2.4.1. X-ray diffraction

For phase analysis and to determine residual stresses, XRD (Bruker D8 Advance with a Cu-Cathode) was used. Measurement parameters were set with the Diffrac Commander software. For the phase analysis, 2θ angles ranged from 30° to 90° (coupled $2\theta/\theta$). Data was analyzed by the Diffrac EVA software. Residual stresses were measured with the $\sin^2\psi$ -method at $2\theta=139.8^\circ$ ($(hkl)=213$). As a calibration for the new Ti₂Mo alloy, a stress-free sample was produced by annealing at 700 °C for 90 minutes in argon atmosphere, to determine d_0 . The reflex shift was measured from $2\theta=137.5^\circ$ to 142.5° at nine different ψ -angles ($\sin^2\psi$ from (-0.4) to (+0.4), step size 0.1) and three φ -angles (0°, 45° and 90°, 0° corresponding to build-up direction). ψ -angles were set with the offset/coupled 2θ setting. For all measurements a fixed sample illumination of 10×5 mm was used. A z-scan prior each measurement ensured the exact height. Data was analysed with the Leptos7 software.

2.4.2. SEM

Surface images of the additively manufactured samples were captured using a Hitachi SU1000 – FlexSEM 1000II. For topographic information SE- and for material contrast BSE-mode was used at magnifications ranging from $\times 100$ to $\times 5000$. Phase-ratio was analysed with the software “ImageJ”.

2.4.3. Roughness

Roughness was measured by a tactile contour measuring station (MarSurf XR 1, model CT 120, equipped with a stylus BFW A 10-45-2/90, amplitude $\pm 250 \mu\text{m}$). For each sample three positions (left, middle, right) with a test track of 4 mm were measured and analysed with the MarWin software (V. 10.00-21.1) according to ISO 21920.

3. Results and discussion

3.1. Surface engineering

Figure 1 shows a comparison of the XRD patterns of SLM-produced cpTi (as received) and Ti₂Mo (as received and annealed) from $2\theta=38^\circ$ to 41° .

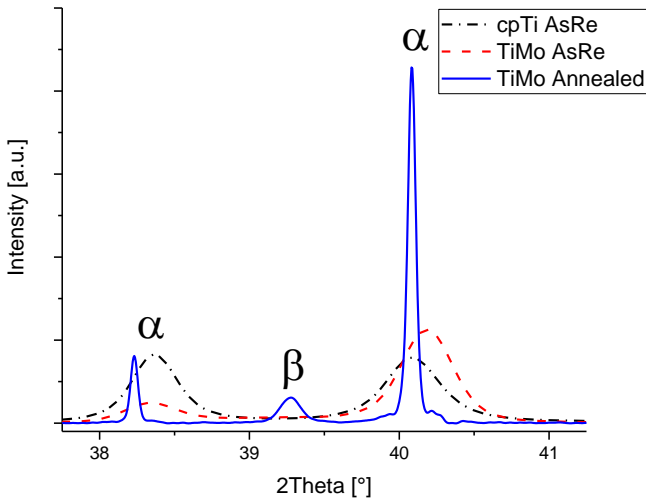


Figure 1 XRD pattern: Comparison of AM cpTi - as received vs. AM Ti2Mo - as received and annealed at T = 900 °C, 90 min.

Through the high temperatures and fast cooling rates of the selective laser melting process, the Ti2Mo alloy solidifies in an alpha martensitic state. Therefore, no beta-phase is seen in the as received state, for both cpTi and Ti2Mo alloys. After annealing at T=900 °C for 90 minutes, a titanium beta phase forms because of the beta stabilization effect of Molybdenum [14].

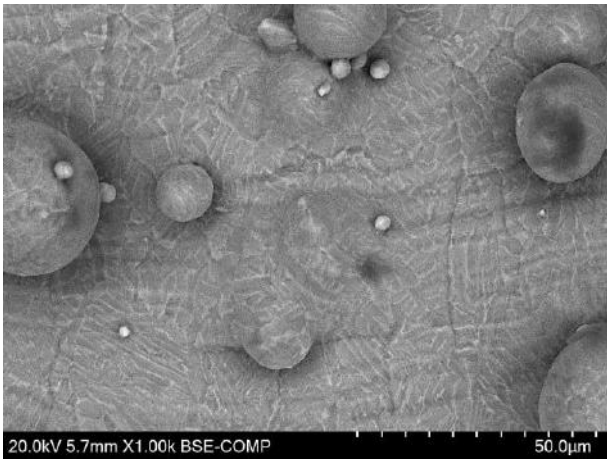


Figure 2 SEM - BSE picture, x1000 magnification. Surface and phases of AM Ti2Mo - as received, annealed at 900 °C for 90 min.

In

Figure 2 the $\alpha+\beta$ microstructure is represented in BSE mode by dark (α -Ti) and light (β -Ti) areas. Moreover, the surface of the additively manufactured Ti2Mo-alloy is shown in the as received state, after annealing at 900 °C for 90 minutes. There is no homogeneous or even surface, due to the laser tracks and sintered spherical particles as a result of the laser melting process.

To guarantee a homogeneous and smooth surface, in the first step the samples were blasted using a high-class corundum with a small particle size distribution (63–106 μm) and a sharp form of the blasting material, as presented in

Figure 3.

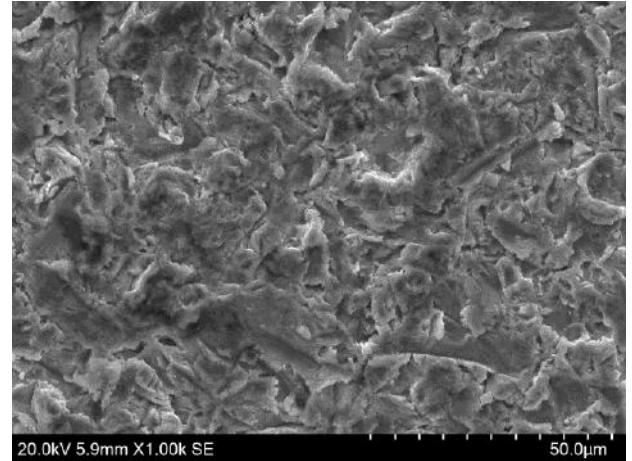


Figure 3 SEM - SE picture, surface of AM Ti2Mo - blasted with high class corundum grit of 63-106 μm in size, x1000 magnification.

Figure 4 shows the smoothed surface of the AM Ti2Mo after using the PEP process on blasted samples for 10 minutes at 85 °C (T_{Start}).

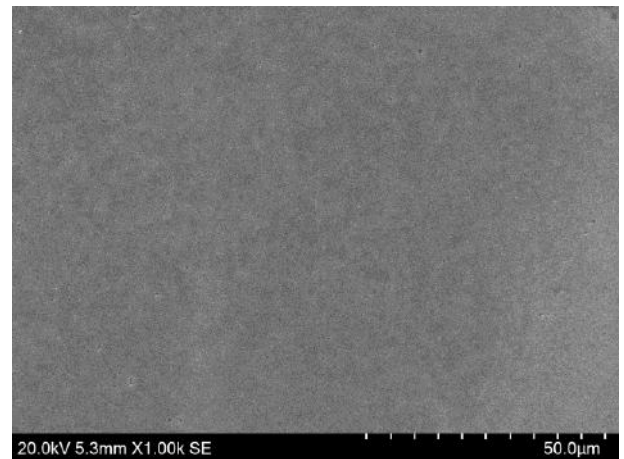


Figure 4 SEM - SE picture, surface of AM Ti2Mo – after plasma electrolytic polishing for 10 minutes at 85-96 °C, x1000 magnification.

During the PEP process the temperature increases up to 96 °C. The current density is built up until a constant value of 0.1 A/cm² is reached. The voltage is set to a constant value of 300 V. As the electrolyte an aqueous, low concentrated salt solution is used [16-18]. Sodium fluoride (NaF) and ammonium chloride (NH₄Cl) are dissolved in deionized water and are stirred constantly during the process. The chosen electrolyte composition, for the lowest roughness and highest optical mirror finish, is 1.5 % NaF + 1.5 % NH₄Cl.

Figure 5 shows the obtained average roughness (R_a , R_z) and waviness (W_a , W_q) of blasted (black) and additionally plasma electrolytically polished (red) AM Ti2Mo samples. Roughness is correlating with process time (the longer, the smoother) and NaF-concentration in the electrolyte. NaF-concentrations higher than 1.5 % cause pitting on the surface, which leads to higher R_a - and R_z -values. Concentrations lower than 1.5 % NaF lead to an unfinished smoothed surface. The resolution of the profilometer is at 20 nm. Values of the PEP-samples, which are below this resolution, need to be verified with an optical measurement system.

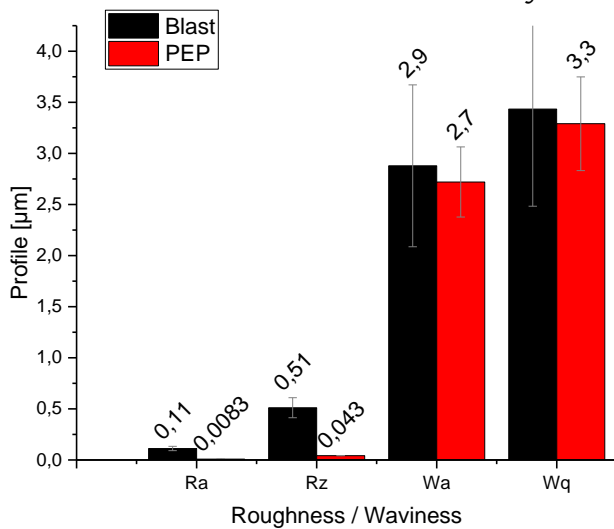


Figure 5 Mean Roughness (R_a , R_z) and Waviness (W_a , W_q) of blasted (black) and plasma electrolytically polished (red) AM Ti2Mo samples.

Since the PEP process minimizes just the micro roughness and not the overall shape of the part being polished (

Figure 6), R_a and R_z values are determined in a range of 100 µm. W_a and W_q values are determined over 4 mm test length [17]. The overall waviness of the polished samples compared to the blasted ones is not changing. Only the standard deviations of the W_a and W_q values get significantly smaller by the PEP process. In contrast to the waviness, the roughness of the polished parts gets significantly smaller compared to the blasted ones. The R_a and R_z values decrease more than 90 % with very low standard deviations.

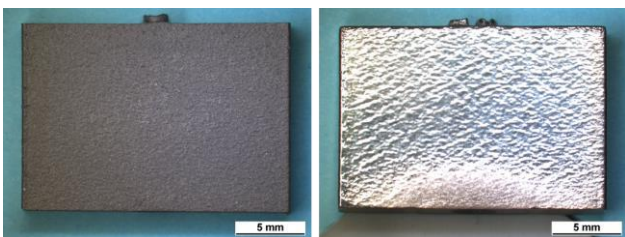


Figure 6 Left: macroscopic picture of a blasted AM Ti2Mo sample. Right: macroscopic picture of a plasma electrolytically polished sample, slightly tilted to demonstrate mirror finish and the shielding edge (side of electrical contact).

The mass loss during the PEP process depending on the process time and the electrolyte salt concentration of NH_4Cl is shown in

Figure 7. The slope of the regression line presents the mean mass loss rate, which is about 8.2 ± 0.4 mg min^{-1} .

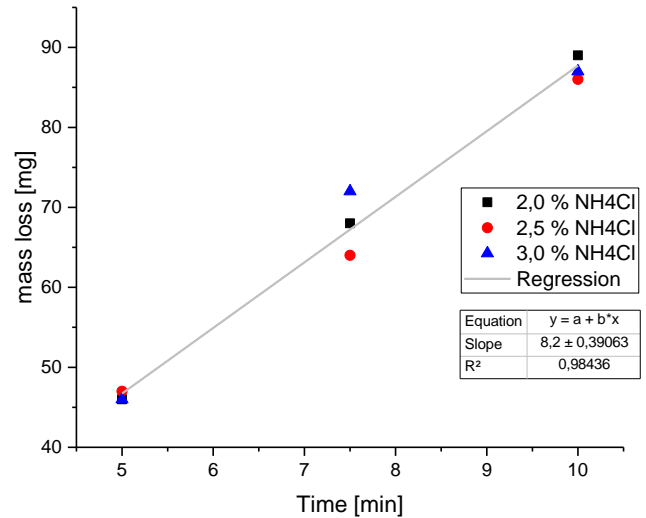


Figure 7 PEP mass loss depending on NH_4Cl concentration and process time. Mean mass loss rate about 8 mg min^{-1} .

There is no significant correlation between the mass loss and the NH_4Cl concentration of the electrolyte. Depending on the NH_4Cl concentration and process time, the shielding edge of the plasma polished samples, which is shown in

Figure 6, varies. At 5 minutes and 3 % NH_4Cl the shielding edge is the largest and at 10 minutes and 1.5 % NH_4Cl the smallest.

Residual stresses, generated by the high temperatures and cooling rates of the directional AM process [19] have to be controlled in order to prevent mechanical failure.

Figure 8 shows the residual stresses of a Ti2Mo sample additively manufactured by the selective laser melting process after different surface modifications. Residual stresses of the surface can be adjusted, lowered, or increased using different techniques. In the ‘as received’ state, the Ti2Mo samples show an anisotropic stress state, with high tensile stresses >450 MPa in built up direction (φ -angle 0°) and lowest stresses at 90° (~ 150 MPa). Positive values represent tensile and negative values compressive stresses. To ensure the accuracy of the stress values, a stress-free sample was produced previously by annealing at $700^\circ C$ for 90 minutes in argon atmosphere followed by furnace cooling. The d-spacing of the stress-free sample provides

a comparison for the residual stress measurement of the AM Ti2Mo alloy.

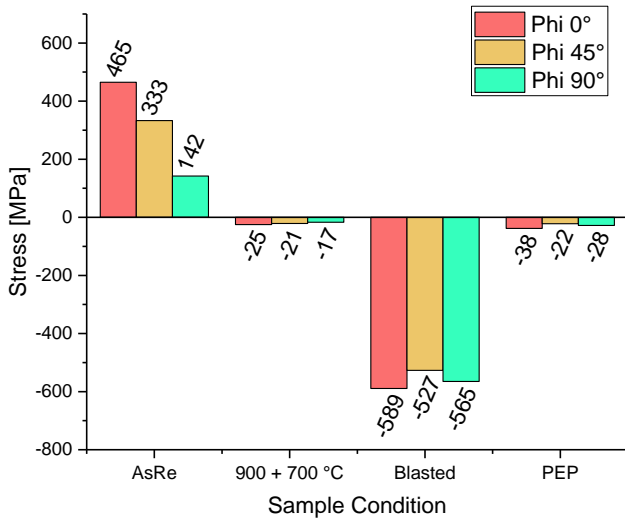


Figure 8 XRD Residual stress analysis – $\sin^2\psi$ -methode. Comparison of the stresses (ϕ -angle 0° , 45° , 90°) of AM Ti2Mo in four different successive conditions/preparation steps: 1. As received, 2. Annealed at $900 + 700^\circ\text{C}$, 3. blasted with high class corundum grit, 4. Plasma electrolytically polished.

After annealing at 900°C for 90 minutes in argon atmosphere (furnace cooling), a more isotropic stress state is reached. A low compressive stress is formed, which can be explained by the formation of the beta phase at 900°C resulting into a shift of the alpha titanium ($(hkl) = 213$) reflex. Additional annealing at 700°C lowers the compressive stress slightly. After blasting with high class corundum grit at 3 bar, a high compressive stress on the surface up to $\sim 600\text{MPa}$ is formed. Through plasma electrolytic polishing the top surface is removed and residual stresses of the bulk material, comparable to the ones after the annealing step are obtained.

3.2. Corrosion investigations

Figure 9 presents the comparison of the potentiodynamic polarization curves of conventionally produced (cast) and additively manufactured (SLM) cpTi and Ti2Mo, measured in simulated body fluid (Hanks' solution) at 37°C . All samples were blasted and cleaned before the measurement. The open circuit potential (OCP) is slightly higher for the AM samples in comparison to the conventionally produced alloy in both cases. In addition to this, the AM samples show lower current densities compared to the casted samples. The AM Ti2Mo samples show the highest resistance against polarization in simulated body fluid at 37°C . Due to the fine lamellar α -martensitic microstructures, that occur by the additive manufacturing process, passive films on the titanium

samples can form faster which leads to higher corrosion resistance [21].

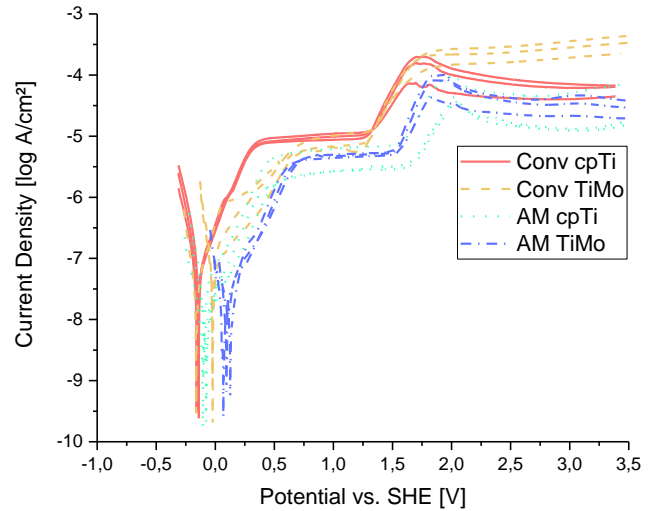


Figure 9 Potentiodynamic polarization measurements in simulated body fluid (Hanks' solution) at 37°C . Comparison between cpTi and Ti2Mo, conventionally (cast) and additively (SLM) produced.

In addition to the potentiodynamic polarization, tribocorrosion tests have been carried out for cpTi and Ti2Mo, both conventionally produced (cast) and additively manufactured (SLM). In

Figure 10 the OCP without, while (potential drop) and after (potential recovery) the friction is presented by the chronopotentiometric curves. Ti2Mo alloys show the highest starting OCP, both additively and conventionally manufactured. The AM cpTi shows a 100 mV higher starting OCP compared to the conventionally produced cpTi.

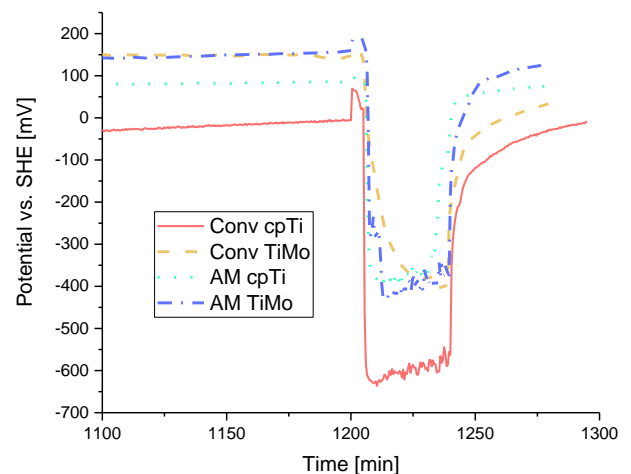


Figure 10 Electrolytic tribocorrosion measurement in simulated body fluid (Hanks' solution) at 37°C . Comparison of OCP between cpTi and Ti2Mo, conventionally (cast) and additively produced (SLM).

During friction the potential on both Ti2Mo alloys drops similarly by about 550 mV. The highest

potential drop of 650 mV is observed for the cast cpTi while the lowest one of 475 mV is obtained for the SLM cpTi. The AM samples show a fast OCP recovery reaching almost the starting value in only 30 minutes after friction has been stopped. The conventional cpTi shows a slightly lowered recovery potential compared to the AM samples while with a difference of 125 mV the cast Ti2Mo shows the lowest recovery potential.

4. Conclusion

The aim of this work with respect to surface engineering has been to design a process route towards smooth and homogeneous surfaces of additively manufactured parts, that can be compared to mechanically produced surfaces. The plasma electrolytic polishing (PEP) process in combination with previous blasting provides such a smooth surface without changing the general shape of the part. Depending on the application, like e.g. dental implant abutments or hip joint sockets, the plane surface may be used as an antibacterial one [15] or for further surface treatments such as structuring and/or coatings. Residual stresses occurring due to the AM process can be lowered and adjusted through heat treatments and surface modifications. The additively manufactured Ti2Mo alloys have proven suitable for medical implants in terms of corrosion properties since they show similar or even better corrosion resistance compared to conventionally produced cpTi and Ti2Mo.

5. Acknowledgements

The authors gratefully acknowledge the German Federal Ministry for Economic Affairs and Climate Action (BMWK) for the financial support of the project under grant number 21671 N via the German Federation of Industrial Research Associations (AiF) based on a decision of the German Bundestag. Samples were manufactured by Fabian Haase and Carsten Siemers (TU Braunschweig, Germany). Corrosion cells have been constructed by Jano Bender, Yvonne Hohmann and Heinrich Kopietz (mechanical workshop at DECHEMA Research Institute). Installation of the corrosion testing setup was supported by technician Antonio Pereira (DECHEMA Research Institute).

6. References

- Breme et al., Titanium and its Alloys for Medical Applications, *Wiley* (2003), 423-451.
- Geetha et al., Ti based biomaterials, the ultimate choice for orthopaedic implants – A review, *Progress in Materials Science, Elsevier* (2009).
- Elias et al, Biomedical Applications of Titanium and its Alloys, *JOM60*, No. 3 (2008) 46-49.
- Haase et al., Aluminum- and Vanadium-free Titanium Alloys for Medical Applications, *MATEC Web of Conferences* 321, 05008 (2020).
- Duda et al., 3D Metal Printing Technology, *ScienceDirect, Elsevier* (2016).
- Zhang et al., Powder bed fusion manufacturing of β -type titanium alloys for biomedical implant applications: A review, *Journal of Alloys and Compounds, Elsevier* (2023)
- Revilla-León et al., A Review of the Applications of Additive Manufacturing Technologies Used to Fabricate Metals in Implant Dentistry, *Journal of Prosthodontics* (2020)
- Gibson et al., Additive Manufacturing Technologies, 3rd edition, *Prosthetics and Implants, Springer* (2021) Chapter 21.3.2.
- ASTM F2792-12a: Standard terminology for additive manufacturing technologies, Geneva, Switzerland: *International Organization for Standardization* (2012).
- Zeidler et al., Plasma-Electrolytic Polishing as a Post-Processing Technology for Additively Manufactured Parts, *CIT-journal, Wiley-VCH* (2022).
- Belkin et al., Mechanism and technological opportunity of plasma electrolytic polishing of metals and alloys surfaces, *Applied Surface Science Advances, Elsevier* (2020).
- Prevéy, X-Ray Ddiffraction Residual Stress Techniques, *Metals Handbook. 10. Metals Park: American Society for Metals* (1986) 380-392.
- Luo et al., High-precision determination of residual stress of polycrystalline coatings using optimised XRD-sin 2ψ technique, *Surface & Coatings Technology, Elsevier* (2010).
- Goldberg et al., An Evaluation of B Titanium Alloys for Use in Orthodontic Appliances, *J Dent Res.* (1979)
- Seddiki et al., Evidence of antibacterial activity on titanium surfaces through nanotextures, *Applied Surface Science, Elsevier* (2014).
- Willett et al., Smoothing the surface finish of rough metal articles, EP 3 359 712 B1, *EUROPEAN PATENT SPECIFICATION* (2022)
- Nestler et al., Plasma Electrolytic Polishing – an Overview of Applied Technologies and Current Challenges to Extend the Polishable Material Range, *Science Direct, Elsevier* (2016).
- Aliakseyeu et al., Plasma Electrolyte Polishing of Titanium and Niobium Alloys in Low Concentrated Salt Solution Based Electrolyte, *MECHANIKA* (2021) Volume 27(1): 88-93
- Teixeira et al., A Review of Heat Treatments on Improving the Quality and Residual Stresses of the Ti–6Al–4V Parts Produced by Additive Manufacturing, *MDPI* (2020).
- Jáquez-Muñoz et al., Electrochemical Behavior of Titanium Alloys Using Potentiodynamic Polarization, *ECS Trans.* 101 173 (2021).

21. Maleki-Ghaleh et al., Electrochemical and cellular behavior of ultrafine-grained titanium in vitro, *Materials Science and Engineering C, Elsevier* (2014).

MECHANICAL PROPERTIES OF Ti–Mo–Al SHAPE MEMORY ALLOY AGED AT α'' REGION

Naoki Nohira, Wan-Ting Chiu, Akira Umise, Masaki Tahara, and Hideki Hosoda

Institute of Innovative Research, Tokyo Institute of Technology, 4259 Nagatsuta-cho, Midori-ku, Yokohama, 226-8503, Japan

β -Ti based shape memory alloys (SMAs) often become brittle by heat treatment at intermediate temperatures, known as ω embrittlement. In order to produce β -Ti SMAs without suffering from the ω embrittlement, Ti–Mo–Al alloys containing higher Al content than those reported were designed for further suppression of the undesired ω phase. As a part of our systematic investigation of the Ti–Mo–Al SMAs, the effect of the aging heat treatment below their reverse martensitic transformation start temperature (A_s) from α'' martensite to parent β on mechanical properties was clarified in this study. Several Ti–Mo–Al alloy solution treated (ST) specimens were aged below A_s up to 100 ks. Yield stress increased after aging, while fracture strain decreased with increasing aging time. When the aging time exceeded 10 ks, the specimens became brittle. However, the ω phase was not detected, but only a single α'' phase in the aged specimens as expected. This brittleness is discussed in connection with isothermal α'' phase formation from the α'' martensite.

Keywords: α'' phase, aging, martensite aging, mechanical property, shape memory effect, Ti–Mo–Al

1. Introduction

The potential applications of β -Ti based shape memory alloys as actuators and biomedical materials have been gaining significant attention in recent years. However, the formation of the ω phase has been a major issue with these alloys. The use of metastable phases in β -Ti based shape memory alloys makes them susceptible to aging and the formation of the ω phase, which is another metastable phase. This phase can cause degradations of ductility and shape memory behaviours, resulting in property degradation upon aging. As a result, it is essential to find ways to suppress the formation of the ω phase in order to improve the long-term performance of these alloys. Recent studies have shown that the use of Al-rich composition alloys with higher aluminium content than conventionally used ones can effectively suppress the formation of the ω phase, leading to the development of promising alloys with superelasticity[1] and high-temperature shape memory properties[2]. In this study, an Al-rich alloy with 10 mol% or more of Al was prepared to investigate whether aging to the α'' single-phase composed alloy causes property degradation or not when the ω phase is absent. Previous studies have reported that the ω phase was not formed inside the α'' phase[3], suggesting that aging in the α'' single-phase alloy may not cause property degradation. However, up to date, only limited studies have worked on the effect of aging on the mechanical properties of the α'' single-phase alloy possessing relatively high Al content. Therefore, the aim of this study is to clarify the effect of aging below the A_s temperature on the deformation behaviour and ductility of the α'' single-phase alloy.

2. Experimental

In this study, titanium (purity 99.99%), molybdenum (purity 99.9%), and aluminium (purity 99.99%) were selected as starting elements for

synthesizing Ti–3.5Mo–11Al and Ti–3.5Mo–14Al (mol%) alloys. The ingots were produced by the arc melting method using a non-consumable tungsten electrode under an Ar atmosphere. The obtained ingots were homogenized at 1273 K for 7.2 ks and then hot-rolled. Subsequently, the samples were subjected to solution treatment (ST) at 1273 K for 1.8 ks under a high-purity Ar atmosphere and quenched in ice water. The oxygen content of the ST specimens was measured by inert gas fusion, and the maximum content was found to be 0.06 mass%. The influence of oxygen content was thus not considered in subsequent analysis. Some of the ST samples were aged at 573 K, where an α'' single-phase state was expected. X-ray diffraction (XRD) measurements were performed to examine the phase constituent range from 20° to 120° in 2θ . Scanning electron microscopy (SEM) observations were also conducted to investigate the microstructure using electro-polished ST specimens. The aged specimens were directly observed without any surface treatment in order to observe microstructural changes, such as surface relief generated during aging. Tensile testing was performed at a strain rate of $8.3 \times 10^{-4} \text{ s}^{-1}$, with the displacement of the specimen measured using a non-contact digital video extensometer attached to the testing machine. Micro-Vickers hardness tests were performed under a load of 500 g with a dwell time of 10 s. All tests were conducted at room temperature (295 K).

3. Results and Discussion

3.1. Phase constituent

The XRD profiles of the phase constituent of the ST specimens and the aged specimens after 3.6 ks aging at 573 K (AT573K-3.6ks) are displayed in Figure 1. As demonstrated in Figure 1, both alloys of the ST specimens were comprised of α'' martensite single-phase. No alterations in phase constituent were observed in either

alloy of the aged materials, and the α'' single phase was maintained.

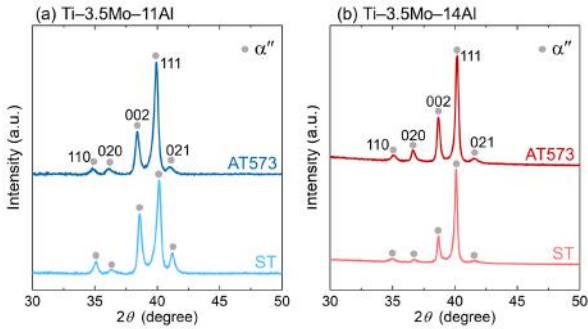


Figure 1. XRD profiles of ST and AT573K-3.6ks specimen: (a) Ti-3.5Mo-11Al alloy and (b) Ti-3.5Mo-14Al alloy.

3.2. Microstructure

Typical self-accommodating microstructures[4] of martensite were observed in both alloys of the ST specimens (not shown). Furthermore, it was discovered that the AT573K-3.6ks specimens, which were confirmed by XRD measurements to be an α'' martensite single-phase, did not undergo any structural changes in the Ti-3.5Mo-11Al alloy after aging. However, in the Ti-3.5Mo-14Al alloy, besides the self-accommodating microstructures in the ST alloy, fine undulations were further observed after aging, as shown in Figure 2. In Ti-3.5Mo-11Al alloy, a similar undulation was observed when the AT573K-54ks specimen, which had been aged for a longer time, was examined.

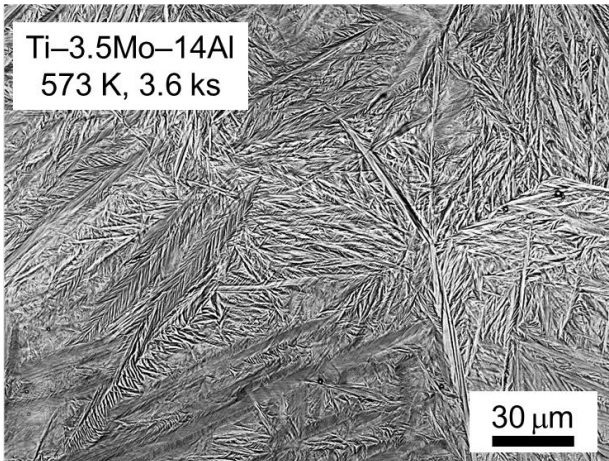


Figure 2. SEM micrograph of Ti-3.5Mo-14Al alloy AT573K-3.6ks specimen exhibited self-accommodating microstructures and fine undulations.

3.3. Deformation behaviour

The stress-strain curves for the ST specimens and AT573K-3.6ks specimens are shown in Figure 3. In the Ti-3.5Mo-11Al alloy, the ST specimens demonstrated a two-stage yielding behaviour, which is typical in shape memory alloys. However, the AT

specimen exhibited an unclear two-stage yielding behaviour, with an increase in yield stress. In the Ti-3.5Mo-14Al alloy, the ST specimen displayed two-stage yielding behaviour, while the AT specimen exhibited a substantial increase in yield stress, resulting in a remarkable reduction in ductility. As these aged materials are considered to be α'' single-phase and do not contain ω phase, it is believed that the deformation behaviours were altered due to a mechanism different from ω embrittlement.

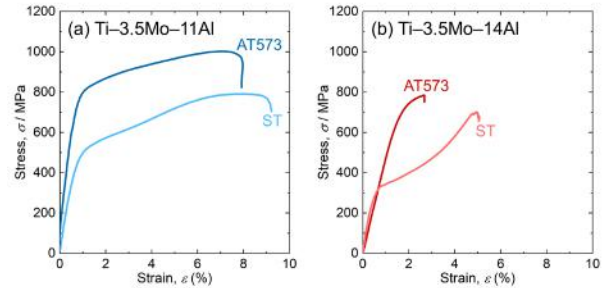


Figure 3. Stress-strain curves of ST and AT573K-3.6ks specimen: (a) Ti-3.5Mo-11Al alloy and (b) Ti-3.5Mo-14Al alloy.

3.4. Aging time dependency

For the Ti-3.5Mo-11Al alloy, aging was carried out at 573 K for different durations, and the Vickers hardness was measured. The results are illustrated in Figure 4. The hardness gradually increased from about 1 ks and reached a maximum at around 3.6 ks, followed by a slight decrease. As shown in Figures 3 and 4, although no structural change was observed in the AT573K-3.6ks specimen, its mechanical properties changed due to aging. Furthermore, the change in mechanical properties because of aging was dependent on the aging time. Therefore, this phenomenon may involve diffusion. Recently, the isothermal α'' phase has been discovered in β -Ti based shape memory alloys, which are formed within the β phase through aging via diffusion and thermal activation processes[5]. The isothermal α'' phase is characterized by its fine size, while it is typically found in several hundred nanometres. And also, alloys contain this phase exhibiting a surface relief[6]. Importantly, these alloys exhibit almost imperceptible compositional variations. While the alloys analysed in this study do not contain a β phase, there are striking similarities in microstructure changes and compositional variations with the isothermal α'' phase. Thus, it may be worthwhile to discuss the brittleness with the formation of the isothermal α'' from the α'' martensite.

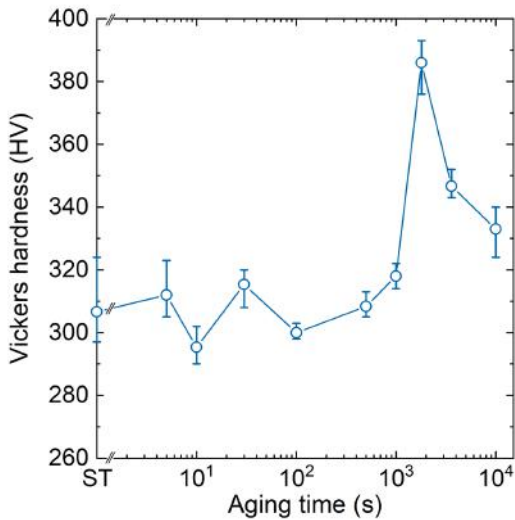


Figure 4. Vickers hardness as a function of aging time for Ti-3.5Mo-11Al alloy. The plot shows the average of five measurements.

Tensile tests were conducted on the Ti-3.5Mo-11Al alloy after aging for different durations at 573 K. The yield stress and fracture strain were measured, and the results are shown in Figure 5. The yield stress increased with increasing aging time while the ductility decreased. Thus, it was found that in the Ti-3.5Mo-11Al alloy, as well as in the Ti-3.5Mo-14Al alloy, aging caused a decrease in ductility. Moreover, a comparison of the two alloys indicated that the Ti-3.5Mo-14Al alloy, possessing a higher Al content, exhibited more degradation in a shorter time. The dependence on Al concentration will be further investigated in detail.

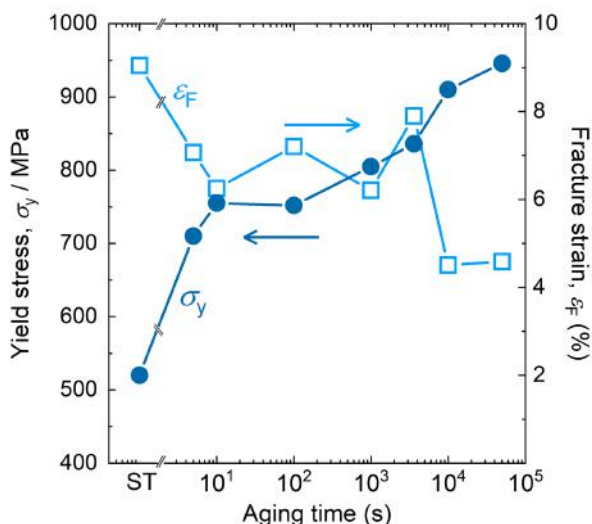


Figure 5. Yield stress (σ_y) and fracture strain (ϵ_f) as a function of aging time for Ti-3.5Mo-11Al alloy. The left y-axis shows the values of σ_y , and the right y-axis shows the value of ϵ_f .

4. Conclusions

Based on the results of this study, it can be concluded that Ti-3.5Mo-11Al and Ti-3.5Mo-14Al alloys exhibit different microstructures and mechanical properties upon aging below A_s temperature. The α'' martensitic single-phase of both alloys remained unchanged after aging, but Ti-3.5Mo-14Al alloy aged specimens exhibited fine undulations in addition to self-accommodating microstructures shown in ST specimens. The two-stage yielding behaviour observed in ST specimens of both alloys was affected by aging below A_s temperature, resulting in increased yield stress and reduced ductility, especially in Ti-3.5Mo-14Al alloy. These changes were aging-time-dependent. The observed changes in microstructure and mechanical properties due to aging may involve diffusion, and the deformation behaviour of the alloys may be influenced by a mechanism different from ω embrittlement.

5. Acknowledgements

This work is supported by the Japan Society for the Promotion of Science (JSPS) (KAKENHI 19H02417, 20K20544, and 22H00256).

6. References

- [1] N. Nohira, W.-T. Chiu, A. Umise, M. Tahara, H. Hosoda, *Materials* 15(3) (2022) 861. DOI: 10.3390/ma15030861.
- [2] N. Nohira, Y. Oshita, W.-T. Chiu, A. Umise, M. Tahara, H. Hosoda, *Material Characterization* (2023) 112850. DOI: 10.1016/j.matchar.2023.112850.
- [3] D.L. Moffat, D.C. Larbalestier, *Metallurgical Transactions A* 19 (1988) 1677–1686. DOI: 10.1007/BF02645135.
- [4] T. Inamura, J.I. Kim, H.Y. Kim, H. Hosoda, K. Wakashima, S. Miyazaki, *Philosophical Magazine* 87 (2007) 3325–3350. DOI: 10.1080/14786430601003874.
- [5] M. Tahara, K. Hasunuma, R. Ibaki, T. Inamura, H. Hosoda, *Advanced Engineering Materials* 21 (2019) 1900416. DOI: 10.1002/adem.201900416.
- [6] Y. Takemoto, M. Yasuno, M. Ikemoto, H. Ando, I. Shimizu, *Materials Transactions* 63 (2022) 489–496. DOI: 10.2320/matertrans.MT-M2021214.

HEAT TREATMENT TO FABRICATE BETA-TYPE TITANIUM ALLOY ROD PARTIALLY DIFFERENT YOUNG'S MODULUS FOR SPINAL FIXATION APPLICATIONS

Masaaki Nakai¹, Kengo Narita², Mitsuo Niinomi³⁻⁴

1 Department of Mechanical Engineering, Faculty of Science and Engineering, Kindai University, Higashiosaka 577-8502, Japan

2 Maruemu Works Co., Ltd., Daitou 574-0015, Japan

3 Institute for Materials Research, Tohoku University, Sendai, 989-8577, Japan

4 Department of Materials and Manufacturing Science, Graduate School of Engineering, Osaka University, Suita 565-0871, Japan.

Spinal implants using rods and screws are being widely used to treat spinal deformities and other diseases. The rods are used for fixing movements of a part of spine. However, the rods sometimes break under load occurring in daily life of patients, and thus they are required to have high strength. On the other hand, if the rigidity of the rod is too high, stress will concentrate on the intact parts without fixation by the rods, and secondary fractures and adjacent intervertebral disorders are likely to occur. Therefore, a part of rod for fixing the lower side of the lumbar vertebra should be strengthened, while the other part for fixing the upper side should have low stiffness. To meet these requirements, we propose a heat treatment process for fabrication of titanium alloy rods. Ti-29Nb-13Ta-4.6Zr alloys with oxygen contents of 0.2 and 0.4% were used as the materials. The rods with partially different Young's moduli were fabricated by aging treatment at 723 K, followed by partial heating up to above the β -transus temperature and quenching by high-frequency induction heating (IH-treatment). A single β -phase, which has low Young's modulus, was obtained by IH-treatment. With regard to the as-aged parts, the precipitated condition of the α -phase can be changed by varying the aging time. The obtained Young's modulus and strength reflect this change. Near the boundary between the as-aged and IH-treated parts, the hardness is gradually changed, and it is possible to gradually soften the material from the as-aged part to the IH-treated part.

Keywords: Biomedical titanium alloy, heat treatment, Young's modulus, implant, Spinal fixation.

1. Introduction

Titanium alloys are being used for spinal fixation devices such as rods, screws, and plugs. Such the rods may break under load during use, and must have high strength to prevent fractures. Generally, high strength is associated with high rigidity. However, if the rigidity of the rod is too high, stress will concentrate on the normal area adjacent to the fixation site, and secondary fractures and adjacent intervertebral disorders are likely to occur. Therefore, the desirable properties of rods are difficult because they must have high strength to prevent fractures while low stiffness to prevent secondary fractures and adjacent intervertebral disorders.

As an effective method for achieving low stiffness, the adoption of materials with low Young's modulus, close to that of bone (approximately 10–30 GPa), has been proposed. Particularly, titanium alloys with Young's modulus of approximately 40–80 GPa, which is approximately 1/4 of that of stainless steel and cobalt alloys and approximately 1/2 of conventional titanium alloys, have been newly developed for biomedical applications and are expected to be used in practice [1,2]. However, since the strength of these alloys is lower than that of conventional titanium alloys, their strength must be increased for practical use. Many studies have attempted to increase the strength of titanium alloys with low Young's modulus. Since these titanium alloys are classified as metastable β -type titanium alloys, the most typical method for increasing their strength is to use precipitation strengthening by thermomechanical treatment. However, since the precipitated phase

(typically, the α -phase) has higher Young's modulus than the β matrix, the precipitation greatly increases the strength but also increases Young's modulus [3–5]. Recent studies have effectively used oxygen as an alloying element, even though oxygen is an impurity of titanium and its removal, to the extent possible, has been previously recommended [6–8]. Since oxygen is an interstitial element, it is expected to provide significant solid solution strengthening and significantly change the phase stability of the β matrix, which in turn affects the precipitation behavior. Interestingly, for β -type Ti-29Nb-13Ta-4.6Zr (TNTZ)-(0.1-0.7)O alloys (mass%), oxygen addition not only enhanced the tensile strength monotonically with increasing oxygen content, but also posed an unusual effect on the elongation, which first decreased at the moderately increased oxygen content of 0.3 mass%, but recovered to a high level with further increasing the oxygen content up to 0.7 mass% under solution-treated conditions [7,9]. Further, oxygen plays a role in stabilizing α phase, and thus it has been reported that the precipitation of α -phase during aging after solution treatment is enhanced by oxygen addition to β -type TNTZ-(0.1-0.4)O [6] and Ti-35Nb-7Zr-5Ta(TNZT)-(0.06-0.68)O [10] alloys (mass%). In that duration, oxygen is partitioned into precipitated α -phase from β matrix [11,12]. Qi et al. observed that the coherent interface between β -matrix and α -precipitate in a β -type Ti-24Nb-4Zr-8Sn alloy (mass%) aged at 723 K [13]. On the other hand, Chou et al. found that oxygen-concentrated ω precipitate may behave as a non-shearable particle in a β -type Ti-32.7Nb alloy (mass%) including oxygen, while small ω precipitate is conventionally

known to be a coherent particle that is sheared by moving dislocations [14]. Mantri et al. obtained high volume-fraction of non-shearable super-refined α precipitates in β -type titanium alloys through two-step heat treatment, and have suggested that the difficulty in shearing of α precipitates by dislocations accounts for the exceptionally high strength [15]. According to the analogy with these reports, it is expected that oxygen-concentrated α precipitate is likely to lead to higher strength for aged β -type titanium alloys.

Recently, the partial heat treatment of artificial hip joint stems made of titanium alloys with low Young's modulus has been proposed as a method for fabricating medical devices [16]. In an artificial hip joint stem, the required performance of the product is considered separately for each part, and aging treatment is applied only to parts that are frequently broken to achieve high strength for the prevention of fractures and low stiffness for the suppression of stress shielding.

This study applied this concept to spinal fixation devices, and fabricated rods for which the lower side of the lumbar vertebrae, which is the most likely to be broken, was aged for precipitation strengthening, while the upper side of the lumbar vertebrae was solution-treated to achieve low Young's modulus. Details have already been reported previously [17] and the main aspects are reviewed in this paper.

2. Experimental procedure

Two β -type Ti-Nb-Ta-Zr-O alloys with different oxygen contents, namely, Ti-29Nb-13Ta-4.6Zr-0.2O and Ti-29Nb-13Ta-4.6Zr-0.4O alloys (mass%), were prepared. Hot-forged round bars were prepared as the received materials. The bars were cold-swaged and then were solution-treated at 1073 K for 3.6 ks followed by water quenching. The solution-treated bars were cold-swaged again and subsequently were subjected to centerless polishing, and then aged at 723 K for 86.4 ks or 259.2 ks. After aging, the rods were partially solution-treated by applying high-frequency induction heating to a part of the rods using a coil to rapidly heat them to temperatures above the β -transus temperature, followed by water quenching without keeping the heated condition (IH-treatment), as shown in Fig. 1. For the IH-treatment, temperature on the surface of rod was measured by a radiation thermometer during heating.

The microstructures of the fabricated rods were analyzed by X-ray diffraction (XRD) and observed using a field emission scanning electron microscopy (FE-SEM). Specimens were machined from the as-aged and IH-

treated parts of the rods for XRD and FE-SEM analysis. In the XRD analysis, the polished cross-section of the rods perpendicular to the longitudinal direction was analyzed using a Co-K α radiation. In the FE-SEM analysis, the plane parallel to the longitudinal direction of the rods was polished and chemically etched, and it was observed with an acceleration voltage of 5 kV.

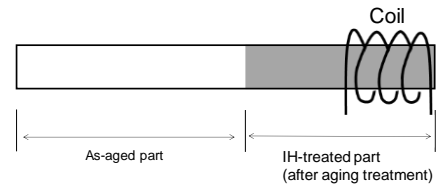


Figure 1. Schematic drawing of partially IH-treated rod after aging treatment [17].

The mechanical properties of the fabricated rods were evaluated using a three-point bending test and a Vickers hardness test. Specimens with a diameter of $d = 3.0 \pm 0.1$ mm and length of around 40 mm were machined from the core of the rods. The specimens were polished with emery paper up to #600 and subjected to a three-point bending test at a crosshead speed of 1.7×10^{-2} mm/s in air at room temperature up to the maximum deflection of 5.0 mm using an Instron-type universal testing machine. The distance between the fulcrums in the test was $L=30$ mm. A Vickers hardness test was conducted to determine the hardness distribution in the transition zone between the as-aged and IH-treated parts of the rod. Five points of hardness in the plane parallel to the longitudinal direction (the same plane as that in the XRD and FE-SEM analyses) were measured at each position with reference to the boundary between the as-aged and IH-treated parts, and the average values and standard deviations were obtained. The test conditions were a load of 4.9 N and a holding time of 10 s.

3. Results and discussion

3.1. Microstructures in fabricated rods

Fig. 2 shows the XRD profiles of the specimens machined from the as-aged and IH-treated parts of the Ti-29Nb-13Ta-4.6Zr-0.2O and Ti-29Nb-13Ta-4.6Zr-0.4O rods. For the as-aged parts of the rods made of different alloys after aging treatments at 723 K for 86.4 ks and 259.2ks, the peaks of the α -phase are detected in addition to those of the β -phase. In contrast, for the IH-treated parts, only β -phase peaks are detected in both alloy rods. Furthermore, strong 110_{β} and 220_{β} peaks are detected as the β -phase peaks in both the as-aged and IH-treated parts. This result indicates that a strong crystallographic texture along $\langle 110 \rangle_{\beta}$ parallel to longitudinal direction forms by cold swaging and does not

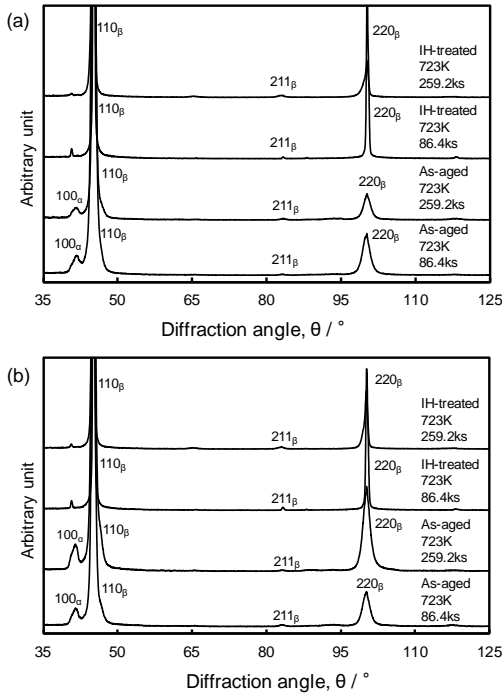


Figure 2. XRD profiles of as-aged and IH-treated parts of (a) Ti-29Nb-13Ta-4.6Zr-0.20 and (b) Ti-29Nb-13Ta-4.6Zr-0.40 rods [17].

disappear even after aging treatment at 723 K and even IH-treatment.

Fig. 3 shows the FE-SEM micrographs of the specimens machined from the as-aged parts of the Ti-29Nb-13Ta-4.6Zr-0.20 and Ti-29Nb-13Ta-4.6Zr-0.40 rods subjected to aging treatments at 723 K for 86.4 ks and 259.2 ks. Fine precipitates with a size of less than 100 nm form in high number density in the as-aged parts of the rods made of both alloys after aging treatments for 86.4 ks. However, in this aged condition, the precipitates are plate-like in the Ti-29Nb-13Ta-4.6Zr-0.20 rod and grain-like in the Ti-29Nb-13Ta-4.6Zr-0.40 rod. According to the XRD profiles shown in Fig. 2, these precipitates were identified as the α -phase. On the other hand, plate-like precipitates, which were detected as the α -phase by XRD analysis (Fig. 2), are observed in the as-aged parts of the rods made of both alloys after aging treatments for 259.2 ks. For each alloy rod, the size and the number density of these precipitates are larger and lower respectively than those of the precipitates after aging treatment for 86.4 ks. The grainy α -phase, which is observed in the Ti-29Nb-13Ta-4.6Zr-0.40 rod subjected to aging treatment for 86.4 ks, is finer than the plate-like α -phase in the Ti-29Nb-13Ta-4.6Zr-0.20 rod under the same aging condition, and its morphology is changed to plate-like by extending the aging duration up to 259.2 ks. Therefore, the grainy morphology is considered to

represent a preliminary stage of plate-like growth. Namely, these results indicate that increasing the oxygen content delays precipitation initiation or growth in Ti-29Nb-13Ta-4.6Zr alloy.

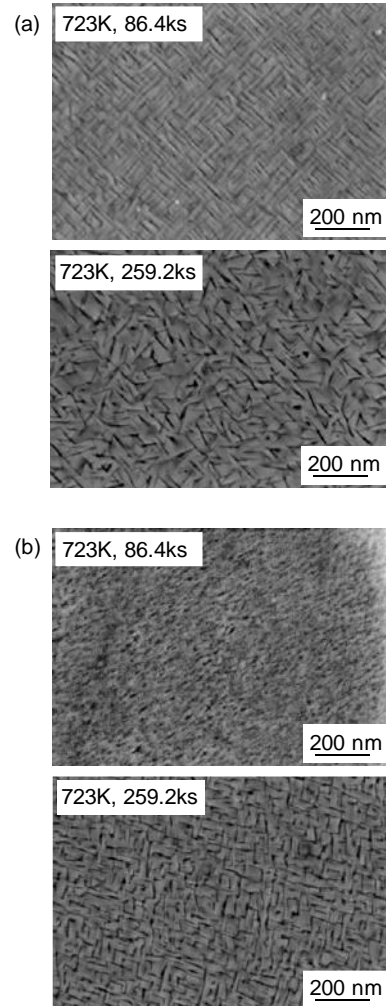


Figure 3. FE-SEM micrographs of (a) Ti-29Nb-13Ta-4.6Zr-0.20 and (b) Ti-29Nb-13Ta-4.6Zr-0.40 rods subjected to aging treatments [17].

3.1. Mechanical properties of fabricated rods

Fig. 4 shows the bending stress–deflection curves of the specimens machined from the as-aged and IH-treated parts of the Ti-29Nb-13Ta-4.6Zr-0.20 and Ti-29Nb-13Ta-4.6Zr-0.40 rods. By comparing the results of the IH-treated parts, it is found that the bending strength of the Ti-29Nb-13Ta-4.6Zr-0.40 rod is higher than that of the Ti-29Nb-13Ta-4.6Zr-0.20 rod. This result is derived from the solid–solution strengthening of the β -phase by oxygen in the Ti-29Nb-13Ta-4.6Zr alloy. The bending strengths of the as-aged parts are higher than those of the IH-treated parts in the rods made of both alloys. The as-aged part of the Ti-29Nb-13Ta-4.6Zr-0.20 rod treated for 86.4 ks causes a fracture, while that of the

Ti-29Nb-13Ta-4.6Zr-0.2O rod treated for 259.2 ks does not. This result suggests that the treatment time of 259.2 ks leads to over-aging, which decreases the bending strength of the Ti-29Nb-13Ta-4.6Zr-0.2O alloy. In our previous report, the aging treatment at 723 K for 259.2 ks was not shown as over-aging for the Ti-29Nb-13Ta-4.6Zr-0.2O alloy [6]. However, in that case, aging treatment was carried out after solution treatment, and age hardening of Ti-29Nb-13Ta-4.6Zr alloy is likely to be enhanced by cold working in comparison to solution treatment before aging treatment for Ti-29Nb-13Ta-4.6Zr alloy [18]. Therefore, it is considered that the Ti-29Nb-13Ta-4.6Zr-0.2O alloy subjected to aging treatment at 723 K for 259.2 ks reached an over-aging condition because of cold swaging before aging treatment in this study. In contrast, for the Ti-29Nb-13Ta-4.6Zr-0.4O rod, the bending strength of the as-aged parts continued to increase as the treatment time increased up to 259.2 ks. This result reflects the possibility of delay in the precipitation initiation or growth, owing to the increase in the oxygen content of the Ti-29Nb-13Ta-4.6Zr alloy, as indicated by the FE-SEM observations.

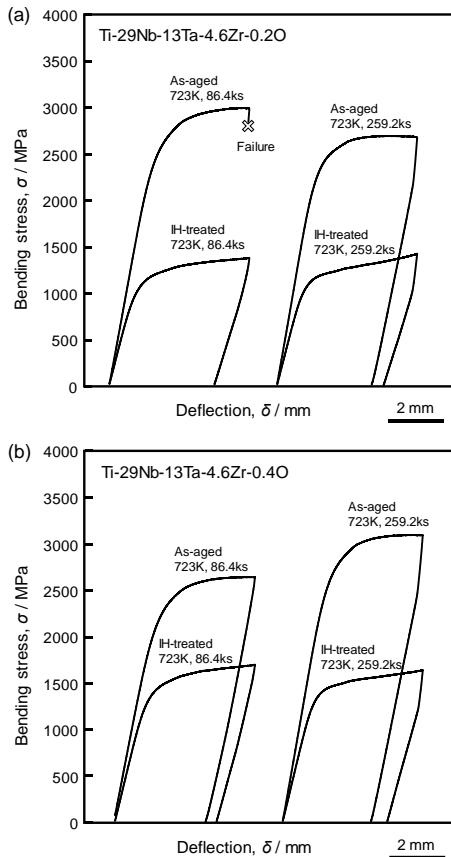


Figure 4. Bending stress–deflection curves of specimens machined from as-aged and IH-treated parts of (a) Ti-29Nb-13Ta-4.6Zr-0.2O and (b) Ti-29Nb-13Ta-4.6Zr-0.4O rods [17].

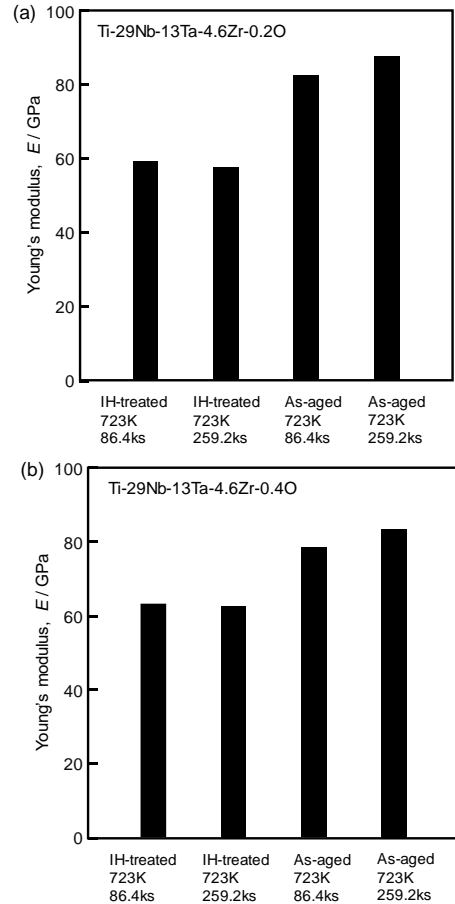


Figure 5. Young's moduli obtained by bending tests for specimens machined from as-aged and IH-treated parts of (a) Ti-29Nb-13Ta-4.6Zr-0.2O and (b) Ti-29Nb-13Ta-4.6Zr-0.4O rods [17].

Fig. 5 shows Young's modulus obtained by the bending test for the specimens machined from the as-aged and IH-treated parts of the Ti-29Nb-13Ta-4.6Zr-0.2O and Ti-29Nb-13Ta-4.6Zr-0.4O rods. For both rods made by different alloys, the Young's moduli of the IH-treated parts are lower than those of any as-aged parts, and their values are approximately 60 GPa, but a slight increase with increasing oxygen content is observed. Among Young's moduli of the as-aged parts for each alloy, the highest value of approximately 90 GPa is obtained from the Ti-29Nb-13Ta-4.6Zr-0.2O rod aged for 259.2 ks. The Young's moduli of the as-aged parts tend to be higher for the Ti-29Nb-13Ta-4.6Zr-0.2O rod compared with the Ti-29Nb-13Ta-4.6Zr-0.4O rod. This result suggests that the increase in the oxygen content contributes to the delay in the precipitation initiation or growth in the Ti-29Nb-13Ta-4.6Zr alloy. For the Ti-29Nb-13Ta-4.6Zr-0.2O rod, the bending strength was influenced by over-aging as the aging time increases, but Young's modulus continues to increase. Since Young's modulus does not depend on the size and morphology of the precipitated phase, but instead only depends on the volume fraction, it is considered that

the volume fraction itself increases beyond 86.4 ks in the Ti-29Nb-13Ta-4.6Zr-0.2O rod by aging treatment at 723 K. At the same time, however, the α -phase coarsens and its number density decreases. Further, the Young's moduli of the as-aged parts of the Ti-29Nb-13Ta-4.6Zr-0.2O rods are higher than those of the Ti-29Nb-13Ta-4.6Zr-0.4O rods at each aging time. This is the opposite trend from the previous report; the Young's modulus of Ti-29Nb-13Ta-4.6Zr-0.2O alloy aged at 723 K for 259.2 ks was lower than that of Ti-29Nb-13Ta-4.6Zr-0.4O alloy aged at the same condition [6]. As already mentioned, the degree of aging progress is different between the previous report and this study, depending on the specimen condition before aging treatment, which is solution treated or cold worked. The aging treatment at 723 K for 259.2 ks after cold swaging is as over-aging for Ti-29Nb-13Ta-4.6Zr-0.2O alloy, but is in progress of aging for Ti-29Nb-13Ta-4.6Zr-0.4O alloy, resulting in the dependence of Young's modulus on oxygen content in Ti-29Nb-13Ta-4.6Zr alloy opposite from the previous study.

Fig. 6 shows the hardness distributions of the Ti-29Nb-13Ta-4.6Zr-0.2O and Ti-29Nb-13Ta-4.6Zr-0.4O rods subjected to aging treatment at 723 K for 86.4 ks and 259.2 ks, followed by IH-treatment. The hardness of the as-aged parts is 1.5–2.1 times higher than that of the IH-treated parts, regardless of the oxygen content of the alloys. Moreover, the change in hardness from the as-aged part to the IH-treated part is gradual and progressively decreases. The fact that the change in hardness is not abrupt is considered as the reason for the suppression of stress concentration at the boundary between the treated parts.

4. Summary

This study proposes a heat treatment process for fabrication of titanium alloy rods for spinal fixation. A part of rod for fixing the lower side of the lumbar vertebrae, which is the most likely to be broken, is strengthened, while the other part for fixing the upper side of the lumbar vertebrae has low stiffness to prevent secondary fractures and adjacent intervertebral disorders. The rods made of Ti-29Nb-13Ta-4.6Zr alloys with oxygen content up to 0.4% were subjected to aging treatment at 723 K, followed by rapid heating and quenching with high-frequency induction heating (IH-treatment) to produce a partially solution-treated rod. The microstructures were observed and analyzed, and the mechanical properties of the as-aged and IH-treated parts of the rods were evaluated. The following conclusions were drawn from this study:

(1) The IH-treated parts of rods made of Ti-29Nb-13Ta-4.6Zr alloys with oxygen contents of 0.2 and 0.4% consist of a single β -phase. In contrast, the α -phase precipitates in the as-aged parts.

(2) The IH-treated parts of both rods made of Ti-29Nb-13Ta-4.6Zr alloys with oxygen contents of 0.2 and 0.4% have lower bending strength and lower Young's modulus (approximately 60 GPa) compared with the as-aged parts. For the as-aged parts of both rods made of two different alloys mentioned above, Young's modulus increases with the aging time. However, the trend of strength is not necessarily the same as that of Young's modulus.

(3) The hardness near the boundary between the as-aged and the IH-treated parts gradually decreases from the as-aged part to the IH-treated part. The change in hardness is not abrupt and is considered to have had a suppressing effect on the stress concentration at the boundary between the as-aged and IH-treated parts.

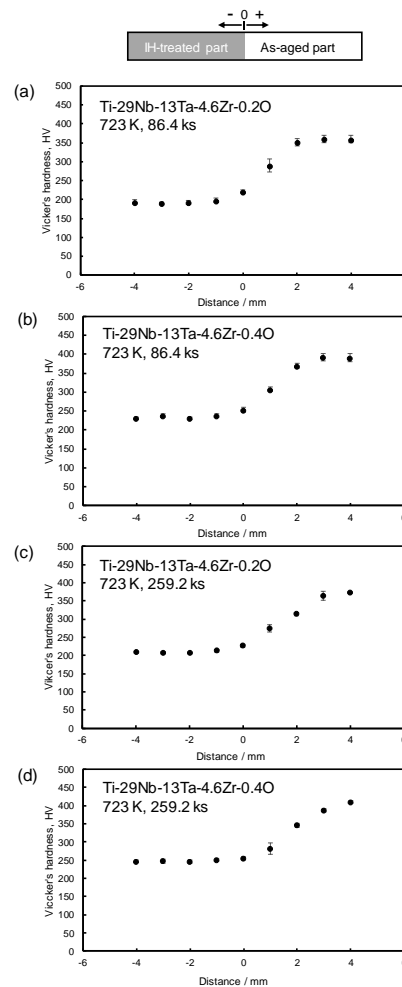


Figure 6. Vickers hardness distributions near boundary between as-aged and IH-treated parts in (a), (c) Ti-29Nb-13Ta-4.6Zr-0.2O and (b), (d) Ti-29Nb-13Ta-4.6Zr-0.4O rods subjected to aging treatment followed by partial IH-treatment. (Aging treatments were carried out at 723 K for (a), (b) 86.4 ks and (c), (d) 259.2 ks) [17].

5. References

1. M. Niinomi, M. Nakai, J. Hieda, *Acta Biomater.* 8 (2012) 3888–3903.
2. D. Banerjee, J.C. Williams, *Acta Mater.* 61 (2013) 844–879.
3. Y.L. Hao, R. Yang, M. Niinomi, D. Kuroda, Y.L. Zhou, K. Fukunaga, A. Suzuki, *Metall. Mater. Trans. A* 34 (2003) 1007–1012.
4. T. Akahori, M. Niinomi, H. Fukui, M. Ogawa, H. Toda, *Mater. Sci. Eng. C* 25 (2005) 248–254.
5. K. Narita, M. Niinomi, M. Nakai, J. Hieda, K. Oribe, *J. Mech. Behav. Biomed. Mater.* 9 (2012) 207–216.
6. M. Nakai, M. Niinomi, T. Akahori, H. Tsutsumi, M. Ogawa, *Mater. Trans.* 50 (2009) 2716–2720.
7. F. Geng, M. Niinomi, M. Nakai, *Mater. Sci. Eng. A* 528 (2011) 5435–5445.
8. H. Liu, M. Niinomi, M. Nakai, S. Obara, H. Fujii, *Mater. Sci. Eng. A* 704 (2017) 10–17.
9. H. Liu, M. Niinomi, M. Nakai, X. Cong, K. Cho, C.J. Boehlert, V. Khademi, *Metall. Mater. Trans. A* 48 (2017) 139–149.
10. J.I. Qazi, B. Marquardt, L.F. Allard, H.J. Rack, *Mater. Sci. Eng. C* 25 (2005) 389–397.
11. M. Niinomi, M. Nakai, M. Hendrickson, P. Nandwana, T. Alam, D. Choudhuri, R. Banerjee, *Scripta Mater.* 123 (2016) 144–148.
12. T. Homma, A. Arafah, D. Haley, M. Nakai, M. Niinomi, M.P. Moody, *Mater. Sci. Eng. A* 709 (2018) 312–321.
13. L. Qi, S. He, C. Chen, B. Jiang, Y. Hao, H. Ye, R. Yang, K. Du, *Acta Mater.* 195 (2020) 151–162.
14. K. Chou, N. Li, E.A. Marquis, *Acta Mater.* 220 (2021) 117302.
15. S.A. Mantri, D. Choudhuri, T. Alam, G.B. Viswanathan, J.M. Sosa, H.L. Fraser, R. Banerjee, *Scripta Mater.* 154 (2018) 139–144.
16. S. Hanada, N. Masahashi, T.-K. Jung, N. Yamada, G. Yamako, E. Itoi, *J. Mech. Behav. Biomed. Mater.* 30 (2014) 140–149.
17. M. Nakai, K. Narita, K. Kobayashi, K. Sasagawa, M. Niinomi, K. Hasegawa, *Mater. Trans.* 64 (2023) 147–154.
18. T. Akahori, M. Niinomi, K. Ishimizu, H. Fukui, A. Suzuki, *J. Japan Inst. Metals* 67 (2003) 652–660.

HIGH STRENGTH, LOW-MODULUS NANOSTRUCTURED Ti 13Nb 13Zr FOR DENTAL IMPLANT APPLICATION

Lina Klinge¹, Lukas Kluy², Christopher Spiegel³, Carsten Siemers¹

1 Institute for Material Science, TU Braunschweig, Langer Kamp 8, 38106 Brunswick, Germany.

2 Institute for Production Engineering and Forming Machines, TU Darmstadt, Otto-Berndt-Straße 2, 64287 Darmstadt, Germany.

3 Research Laboratory for Biofilms and Implant Associated Infections (BIOFILM LAB), Medical University of Innsbruck, Schöpfstraße 41, 6020 Innsbruck, Austria.

In dentistry, a high strength, low-modulus nanostructured titanium alloy is the key to a successful tooth replacement. High strengths avoid an implant and abutment breakage due to a minimized wear, whereby the abrasion is also diminished. Abrasion, and therefore the release of metal particles, is a critical factor in case conventional titanium alloys such as Ti 6Al 4V (ELI) or Ti 6Al 7Nb are used as these alloys contain critical alloying elements like aluminum (Al) and vanadium (V) which are cytotoxic and might be harmful to the human health; e.g., higher concentrations of Al are associated with dementia, the Alzheimer disease and breast cancer.

Therefore, the second-generation β -rich ($\alpha+\beta$)-titanium alloy Ti 13Nb 13Zr (TNZ) is investigated for the use as a dental implant material. In addition to α - and β -phase, in TNZ alloy, the orthorhombic α'' -martensite phase can form after rapid cooling, i.e., water quenching. The α'' -martensite phase is very soft and good formable (strength of approx. 630 MPa at an elongation at fracture of 25 %) and possesses a very low Young's modulus of approx. 60 GPa which in turn leads to a reduced occurrence of stress shielding.

As a nanostructured implant surface is important for good osseointegration and further growth of bone cells, whereby a bacterial colonization could be prevented simultaneously, Severe Plastic Deformation (SPD) processes like Equal Channel Angular Swaging (ECAS) are used to allow grain refinement and an increase in strength of TNZ. Additional heat treatments (i.e., recrystallization and ageing) reduce work hardening and due to an α'' -martensite decomposition ($\alpha'' \rightarrow \alpha+\beta$), the material becomes nanostructured and is re-strengthened again. After heat-treating the nanostructured TNZ alloy, the following properties are obtained: an UTS of 994 MPa, an elongation of 9.6 % and a Young's modulus of 73 GPa which are very promising properties for dental implant applications.

Keywords: Ti 13Nb 13Zr, TNZ, nanostructured titanium, high strength, low-modulus, equal channel angular swaging (ECAS), severe plastic deformation (SPD), recrystallization, dental implants.

1. Introduction

Due to its good biocompatibility and excellent corrosion behaviour, titanium and its alloys are widely used for implant applications [1]. In dentistry, commonly used implant systems, consisting of the implant (typically surface-structured by etching or the application of a coating to ensure good osseointegration), an abutment (connecting implant and crown), a fixing screw (to tighten the abutment in the implant) and a crown (artificial tooth made of ceramics), are made of CP-Titanium Grade 4 for the implant and Ti 6Al 4V ELI for the abutment and the screw. Although still the best choice whenever metallic implants are concerned, these alloys are associated with several problems. The comparably low strength of CP-Titanium Grade 4 leads to plastic deformation of the implant, wear and abrasion during chewing resulting in relative movements between implant and abutment so that in the worst case implant, screw and abutment breakage might occur. Abrasion is a critical factor as elementary aluminum (Al) and vanadium (V), related ions, as well as their oxides, are cytotoxic [2]. When damaging the oxide layer of a titanium implant, these ions might be released into the human bloodstream where they could cause severe health issues, i.e., higher aluminum concentrations are suspected to cause dementia, the Alzheimer disease

[3] and breast cancer [4]. Therefore, there is an ongoing discussion to replace these alloying elements in future implant applications. The relatively high Young's modulus of 100 – 120 GPa especially of CP-Titanium used as implant material leads to stress shielding and bone loss which is one of the driving factors to cause a disease called periimplantitis. Due to the bone loss, bacteria can colonize in the gaps between bone and implant surface, leading to inflammations. As the bacteria shield themselves from the environment by forming biofilms, the bone cells cannot (re-)attach to the implant surface and, therefore, the implant loosens, which in the worst case leads to total implant loss. This often requires an implant revision surgery. In terms of dentistry, since the amount of bone in the jaw is severely limited, a revision can only be repeated a limited number of times. Therefore, smaller dental implants are favoured to preserve as much of the bone mass as possible. Hence, smaller implant diameters increase the requirements regarding the strength to avoid implant deformation or breakage.

The treatment of periimplantitis includes grinding and polishing of the related implant surface to remove the biofilm. However, previously applied

coatings or etched surfaces are also being removed and re-osseointegration (if at all) only takes place to a lesser extent. To overcome this problem, advanced, next-generation dental implants should be manufactured out of ultrafine-grained material. Due to the different mechanical properties of the grains and the grain (or phase) boundaries, after grinding and polishing of an ultrafine-grained microstructure a nanostructured (slightly rough) surface will redevelop naturally, where the bone cells can (re-)attach and grow, but the colonization of bacteria can be reduced simultaneously.

To produce an ultrafine-grained material, severe plastic deformation (SPD) processes like Equal Channel Angular Pressing (ECAP) or Equal Channel Angular Swaging (ECAS), which has been invented at TU Darmstadt [5], can be used. The ECAS process allows a continuous production of heavily deformed material without the disadvantages of high friction and limited length of the resulting bars which are the characteristics of the ECAP process. Nevertheless, special effort is needed to produce long and straight bars by means of the ECAS process. In particular, a customized tool geometry, forming temperature, feed rate and counter pressure as well as an adequate oscillating frequency and closing height of the tools, needs to be defined. These parameters must be closely coordinated to prevent buckling or breaking of the bars, to avoid adiabatic shear band formation and to gain straight bars with sufficient surface quality to allow automated long turning for implant production. The ECAS process introduces work-hardening, so that the ductility of related bars is strongly reduced. Hence, a post heat-treatment procedure needs to be carried out to increase the ductility again at sufficient strength (but keep the nanostructure) to finally fulfil the requirements of the related medical standards.

In the present study, Ti 13Nb 13Zr (TNZ) alloy, an Al- and V-free second-generation β -rich $\alpha+\beta$ biomedical alloy, which has been introduced in the 1990's [6] and which is specified in the ASTM F1713 has been used. The requirements regarding the mechanical properties for the use as a medical implant material are an ultimate tensile strength (*UTS*) of minimum 860 MPa and an elongation at fracture (*A*) of at least 8 %. The Young's modulus is not specified in ASTM F1713. Bone-remodelling simulations carried out by our project partners have shown, that a Young's modulus between 70 – 80 GPa is beneficial for bone cell adhesion, as on the one hand it is low enough to prevent stress shielding, but on the other hand, it is high enough to avoid overloading of the newly formed bone during the implant ingrowth phase after implantation. To meet the requirements of

ASTM F1713 and to take the Young's modulus into account, internal goals have been set for the mechanical properties. These are the beforementioned Young's modulus of 70 – 80 GPa, an elongation of fracture of minimum 8 % and an *UTS* of at least 950 MPa to prevent the breakage of the implant, abutment and the screw and allow the design of a small implant.

TNZ alloy can occur in the two stable phases α and β . After fast cooling, i.e., water quenching (WQ) from temperatures exceeding the (local) martensite start temperature (M_s) of the present β -phase, the metastable orthorhombic α'' -martensite can form. The α'' -martensite is very soft (*UTS* of approx. 630 MPa) and well formable (*A* of approx. 25 %) and is, therefore, an easy to deform starting structure, even at comparably low temperatures. Due to the fine needle like structure, the α'' -martensite offers an ideal microstructure for severe plastic deformation as during the ECAS process the needles are strongly deformed or even completely separated by shearing and, as a result, provide several seeds for subsequent recrystallization heat treatments. In addition, during the ECAS-forming process the α'' -martensite starts to decompose into small α - and β -grains due to the elevated temperatures resulting from the heat produced by the forming action (and the energy provided by pre-heating the samples) leading to a nanostructured microstructure.

Short-time recrystallization heat-treatments of these deformed samples lead to an ultrafine-grained microstructure with primary- α (α_p) grain sizes smaller than 1 μm , which is essential to prevent bacterial colonization. Depending on the recrystallization temperature, different phase compositions can be adjusted after water quenching, namely, $\alpha+\beta$, $\alpha+\beta+\alpha''$ and $\alpha+\alpha''$ when recrystallization is carried out below β -Transus-temperature (β_T) or a fully martensitic α'' -structure develops when β_T was exceeded during this heat-treatment. A small amount of α_p -phase is desirable to prevent grain growth and also, to improve the fatigue properties. Both, the β -phase and the α'' -martensite, offer low values of the Young's modulus which is important to prevent stress shielding. During a subsequent ageing treatment at moderate temperatures, secondary- α (α_s) phase can be precipitated in the β -phase leading to a nanostructure and a higher strength. In addition, the α'' -martensite (partially) decomposes into small $\alpha+\beta$ substructures during ageing and, therefore, further refine the (already nanostructured) microstructure increasing the strength. Hence, with ongoing martensite decomposition, the elongation at fracture decreases and the Young's modulus increases. Therefore, a well-adjusted heat-

treatment after ECAS needs to be developed to meet the requirements of ASTM F1713 and to optimize the mechanical properties.

2. Materials and methods

The TNZ material used in this study was melted and re-melted resulting in two ingots with diameter 49 mm at GfE Metalle and Materialien GmbH in Nuremberg, Germany. The chemical composition (in weight-%) is shown in table 1. The ingots were afterwards deformed to a diameter of 10 mm by radial forging at GFM GmbH in Steyr, Austria. The final diameter of 8 mm, which is necessary for deforming the material by the ECAS process, was then achieved by rotary swaging at the PtU (Institute for Production Engineering and Forming Machines) of the TU Darmstadt. To avoid adiabatic shear band formation during the rotary swaging to the final diameter, the bars were heat-treated prior to the forming action to establish a fully α' -martensitic starting structure. This can be achieved by annealing the bars above β_T for approx. 30 minutes with subsequent water quenching.

Table 1: Chemical composition of Ti 13Nb 13Zr ingots in wt%.

Ingot 1	Ingot 2	Ingot 1	Ingot 2
Ti Balance	Ti Balance	C 0,014	C 0,010
Nb 13,21	Nb 13,12	H 0,003	H 0,002
Zr 12,89	Zr 12,87	N 0,003	N 0,004
Fe 0,022	Fe 0,023	O 0,065	O 0,068

After producing a fully martensitic structure and subsequently rotary swaging as described earlier, the ECAS process was carried out at the PtU at elevated temperature. For this purpose, the forming jaws were tempered to 150 °C by heating cartridges. Prior to the deformation, the TNZ bars were pre-heated to 150 °C by an inductor. Preliminary studies have shown that ECAS forming at room temperature leads to material defects (e.g., small cracks) and adiabatic shear band formation [7] so that ECAS was carried out at elevated temperature. The feed rate was chosen to 600 mm at a swaging frequency of 30 Hz and a radial infeed of 0.7 mm was applied. In addition, a counterpressure of 8 MPa was used to reach hydrostatic compressive stress conditions. The ECAS tool had a two-channel geometry with an angle of 150° which is shown in figure 1. The forming tool was divided into two oscillating dies, which significantly reduces friction and, therefore, enables the production of long bars. A special feature of ECAS is the unchanged shape of the workpiece after deformation. This allows the process to

be repeated several times to achieve very large strains and, therefore, high dislocation density for grain refinement incrementally.

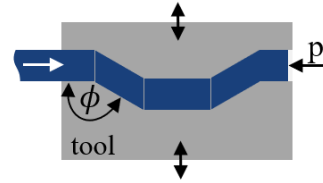


Figure 1. ECAS tool with 2-channel geometry and a tool angle ϕ of 150°.

Besides the production of an optimized implant material, the purpose of this study was to investigate (and understand the underlying mechanisms) the microstructure and mechanical properties after different stages of the forming process. Therefore, five different (intermediate) material states were investigated. The first specimens were taken in the “as received” (AR) condition, i.e., right after radial forging at GFM (\varnothing 10 mm). The second samples were investigated after rotary swaging (RS) to \varnothing 8 mm. The first two steps represent a possible conventional forming process, in which the mechanical properties are sufficient for dental implant applications, but the microstructure might not be fully nanostructured. This could be a potentially cheaper version of the final nanostructured product, as advantages of the TNZ alloy regarding the combination of the chemical composition and mechanical properties already exist when compared to the conventionally used alloys Ti 6Al 4V ELI and CP-Titanium Grade 4. The third step represents a 1-Pass ECAS and the fourth step a 2-Pass ECAS after the rotary swaging. As a fifth step, an additional rotary swaging after 1-Pass ECAS to a diameter of \varnothing 7.5 mm was performed, to straighten the bars and to smoothen the surface and in addition, to increase the level of stored deformation energy. The different steps are summarized in table 2.

Table 2: Different forming stages of the TNZ material.

Stage 1	\varnothing 10 mm AR
Stage 2	\varnothing 10 mm AR + 750 °C 30 min WQ + RS to \varnothing 8 mm
Stage 3	Stage 2 + 1-Pass ECAS
Stage 4	Stage 2 + 2-Pass ECAS
Stage 5	Stage 3 + RS to \varnothing 7.5 mm

For each stage, an optimized heat-treatment (recrystallization + ageing), which has been proven to be promising in previous studies [8], has been applied. For each condition, the microstructure as well as the mechanical properties were investigated.

For the heat-treatments, chamber furnaces Carbolite CWF 1300 using standard air atmosphere were used.

Microstructural investigations were performed at metallographic cross sections. The samples were sectioned by disc cutting (Jean Wirtz, Cuto 20), embedded into EpoMet[®] amorphous, glass fiber reinforced polymer by warm embedding (Buehler Simplimet 4000). Afterwards, the samples were processed by automated (ATM Saphir 550), water-cooled mechanical grinding with SiC grinding papers (size P320, P400, P600, P800, P1200 and P2500) and polishing (9 μm , 6 μm , 3 μm with Kulzer BioDiamant[®] diamond suspension including lubrication followed by OPS polishing with OPS ((25 ml) + H₂O (10 ml) + KOH (0.7 g) + distilled water). Finally, etching was carried out using a special titanium etching reagent (86 ml H₂O + 12 ml H₂O₂ + 4.5 ml HNO₃ + 5 ml HF) for 3 to 5 seconds.

The microstructure has been analysed by means of scanning electron microscopy (SEM, LEO 1550) using an In-lens detector. Hardness tests were carried out using an automated Vickers hardness tester (LECO LV100AT) with HV10 (10 indentations per specimen distributed over the full diameter) and an indentation time of 15 s. The measurement deviation at HV10 is $\pm 3\%$.

Tensile tests were carried out according to DIN EN ISO 6892-1 using a ZWICK/ROELL universal tensile testing machine AllroundLine (100 kN) at room temperature together with the testXpert software by ZWICK. Tensile test specimens were produced according to DIN 50125 B 4x20. For each material condition, two specimens were tested. For a more accurate determination of the Young's modulus a hysteresis loop was performed after 0.8 % plastic strain.

3. Results and discussion

3.1. Microstructure

In figure 2 the microstructures of the five different stages are illustrated. The left site shows the microstructures after the respective forming step without further heat-treatment. The right side shows the microstructures after recrystallization (700 °C / 10 min / WQ) and ageing for (+ 500 °C / 1 h / AC (Air Cooling)) after each forming route.

The microstructure after radial forging (stage 1) consists of highly deformed α (dark) and β (bright) lamellae. After the heat-treatment, comparably coarse ($> 1\ \mu\text{m}$) α_{P} -phase (darker phase in the SEM pictures in figure 1) is visible. The lamellae are not fully broken up

and recrystallized. During the ageing process the martensite decomposes into fine α_{S} - and β -phase. The darker spots in the former β -grains represents non-decomposed martensite. Longer holding times (not shown in the figure) would lead to a complete decomposition of the martensite into α - and β -phase and, thus, to an increase in Young's modulus.

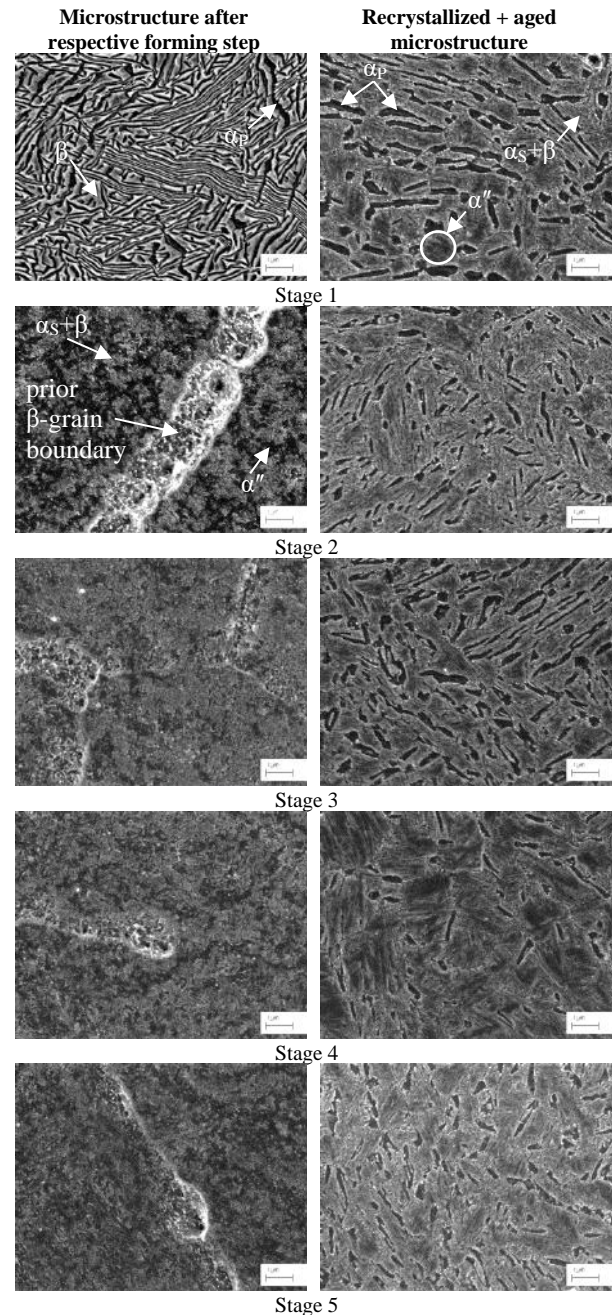


Figure 2. SEM pictures after the five different forming routes. Left side: Microstructure after forming process without further heat-treatment; right side: optimized heat-treatment (recrystallized + aged: 700 °C / 10 min / WQ + 500 °C / 1 h / AC).

As the α_{P} -phase is still larger than 1 μm , the microstructure has not been fully nanostructured which could have a detrimental effect on bone growth and

bacterial colonization. Nevertheless, as can be seen in section 3.3, the mechanical properties are sufficient for the use as implant material. Hence, this might be a production route for cost effective dental implant material as discussed in section 2.

The microstructures after the stages 2 to 5 show a similar appearance. The α'' -martensite (darker matrix) started to decompose into fine dispersed α - and β -grains because of the elevated temperatures together with the high forces of the forming process. Each condition also shows a former β -grain boundary which is interspersed with α -phase. After the recrystallization and ageing treatment of the stages 2 to 5 specimens, the microstructures resemble that of stage 1, but with smaller α -grain sizes. Each condition consists of α -grains smaller than 1 μm and mostly decomposed α'' -martensite. Some darker spots still indicate remaining α'' -martensite which is desirable to keep the Young's modulus low.

3.2. Hardness

Figure 3 shows the hardness values of the different forming stages in the as deformed condition after the respective forming processes (blue dots) and after the heat-treatment was applied (green triangles).

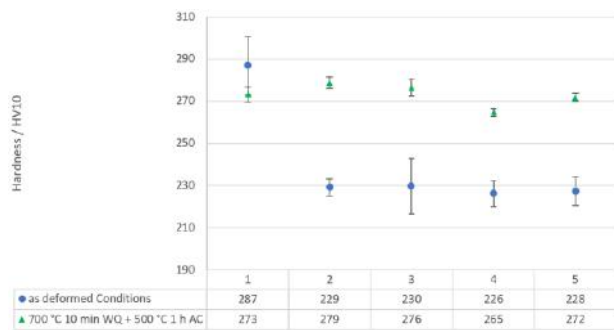


Figure 3. Hardness values for the different forming routes in the as deformed conditions (blue dots) and after heat-treatment (green triangles).

It can be seen that the as deformed condition of stage 1 has the highest hardness due to the work hardening after radial forging. After establishing the α'' -martensite and performing the other forming steps (stages 2 to 5), the hardness decreases significantly and is similar for each condition. After heat-treatment, the specimens of all stages show similar hardness values with low deviations. Stage 4 has the lowest hardness, which is because of the lower amount of α -phase present in the sample (see figure 2) compared to the other ones. Here, the temperature in the furnace could have been slightly higher. As the holding time of 10 minutes for the recrystallization is relatively short (to prevent grain growth), minor deviations in temperature (i.e.,

readjustment effect of temperature in the furnace) could have a great impact on the phase constitution. Another possibility might be temperature deviations during the 2-pass ECAS and/or a significant temperature rise due to the forming process (i.e., forming energy turns into additional heat).

3.3. Mechanical Properties

Table 3 shows the mechanical properties of heat-treated samples for the different stages. In addition, the mechanical properties specified in the ASTM F1713 standard as well as the internal goals are stated. It can be seen that with each stage the Young's modulus of 70 – 80 GPa can be reached. The ultimate tensile strengths also fulfil the requirements of ASTM F1713 for each stage.

Table 3: Mechanical properties after heat-treatment for the different stages. In addition, the mechanical properties required by ASTM F1713 standard and the internal goals are stated.

	E / GPa	$E_{Hysteresis}$ / GPa	UTS / MPa	A / %
Stage 1	84	75	983	9.3
Stage 2	81	75	965	8.7
Stage 3	79	73	988	9.7
Stage 4	85	73	951	4.4
Stage 5	83	73	994	9.6
ASTM F1713	n. def.	n. def.	860	8.0
Internal goals	70-80	70-80	950	8.0

The required elongation at fracture of 8 % can be reached after all stages except for stage 4. With 4.4 % elongation at fracture and an UTS of 951 MPa, this stage has the least promising properties of the investigated routes. As this stage is the 2-Pass ECAS route, it seems obvious that a multiple-pass ECAS operation need not necessarily be beneficial once the tested parameters are used. In addition, a strong deviation between the two tensile test specimens has been observed compared to the other routes, which once more indicates an inhomogeneous distribution of the mechanical properties. To optimize multi-pass ECAS, further testing with different deformation and heat-treatment parameters as well as an intermediate heat-treatment between the ECAS passes might be purposeful. In addition, the bars should be rotated between different passes to obtain a favourable stress superimposition.

High strength (UTS of 983 MPa) at sufficient ductility (elongation at fracture of 9.3 %) can also be reached with stage 1. As mentioned before, even if the microstructure has not been fully nanostructured, it might be a potential more cost-effective condition. In any case, it still outweighs the commercially used alloys because of the lack of critical alloying elements as well as a lower Young's modulus.

The highest strengths can be reached by stage 3 and 5 (UTS of 988 and 994 MPa, respectively). The only difference between those two stages is the additional rotary swaging after the ECAS process for stage 5. This might explain the slightly higher strength due to the additional introduced forming energy. Comparing both microstructures in figure 2, after stage 5, the α -phase appears to be finer than after stage 3. Furthermore, the rotary swaging leads to a smooth surface and a straightening of the bars, which is essential for further turning operations.

4. Summary and outlook

In the present study, the microstructure and the mechanical properties of Ti 13Nb 13Zr after different stages of the forming process (without and with subsequent heat treatments) for the use as dental implants were investigated.

Taking all factors into account (nanostructured microstructure with an α -grain size smaller than 1 μ m, a Young's modulus between 70 and 80 GPa, the highest possible strength with sufficient elongation at fracture (> 8 %), together with good surface quality of the bars), stage 5 offers the best properties for the production of future dental implants. Stage 5 consists of a pre-heat-treatment (750 °C / 30 min / WQ) of radial forged bars to establish a soft α' -martensitic structure to avoid adiabatic shear band formation during rotary swaging prior to the ECAS process. After 1-Pass ECAS the bars were straightened and the surfaces were smoothed with an additional rotary swaging operation to a diameter of 7.5 mm. Finally, a recrystallization and ageing treatment (700 °C / 10 min / WQ + 500 °C / 1 h / AC) was performed to obtain a nanostructured surface (which would redevelop naturally after a periimplantitis treatment) due to martensite decomposition and to set the required mechanical properties. With a Young's modulus of 73 GPa, an UTS of 994 MPa and an elongation at fracture of 9.6 %, this processing route offers a promising condition of TNZ alloy for application as a medical implant material.

In order to determine the biological suitability of the microstructures for the use as implant material, the specimens are going to be tested at the Medical University Innsbruck in terms of osteoblast proliferation and bacterial colonization. In addition, the fatigue properties will be investigated and – if necessary – the deformation and heat-treatment parameters will be adjusted to finally produce a fully nanostructured TNZ material for an advanced, next-generation dental implant system.

5. Acknowledgements

The research leading to the results presented here has been funded by the BMBF (Bundesministerium fuer Bildung und Forschung, Germany), project number 13XP5093C. Financial support is therefore gratefully acknowledged. Furthermore, we would like to thank the GfE Metalle und Materialien GmbH (Nuremberg, Germany) and the GFM GmbH (Steyr, Austria) for casting and forging of the alloy. Finally, the authors would like to thank our project partners ADVANTIQUX Dr. Johannes Scherer and Schweizer Feinwerktechnik.

6. References

1. G. Lütjering, J. C. Williams, *Titanium*, 2nd edn., Springer, Berlin Heidelberg, (2007).
2. M. Geetha, A. K. Singh, R. Asokamani, A. K. Gogia, *Progress in Material Science*, 397-425, (2009).
3. A. Mirza, A. King, C. Troakes, C. Exley, *Journal of Trace Elements in Medicine and Biology*, Volume 40, 30-36, (2017).
4. P. D. Darbre, D. Pugazhendhi, F. Mannello, *Journal of Inorganic Biochemistry*, Volume 105, Issue 11, 1484-1488, (2011).
5. M. Görtan, published dissertation, TU Darmstadt, Germany, (2014).
6. J. A. Davidson, P. Kovacs, United States Patent Nr. 5,169,597, Dec. 8, 1992.
7. L. Klinge., C. Siemers, L. Kluy, et al., *Journal of Materials Research* 37, 2581-2588 (2022).
8. L. Klinge, C. Siemers, C. Jahnke, *Proceedings of the 61st Conference of Metallurgists, COM 2022*, Paper No. 48, The Canadian Institute of Mining, Metallurgy and Petroleum, ISBN: 978-3-031-17425-4, Springer.

HIGHLY EFFICIENT CORAL PROPAGATION USING TITANIUM AND REGENERATIVE MEDICINE TECHNIQUES

Masato Ueda^{1,2,3}, Nanako Kosaka⁴, Tomoyuki Takahashi⁵, Masahiko Ikeda⁶

1 Department of Chemistry and Materials Engineering, Kansai University, 3-3-35 Yamate-cho, Suita, 564-8680, Japan.

2 Kansai Univ. Carbon Neutrality Research Centre (CNRC), Kansai University, 3-3-35 Yamate-cho, Suita, 564-8680, Japan.

3 Innoqua Inc., 3-7-10 Toranomon, Minato-ku, Tokyo, 105-0001, Japan.

4 Graduate School of Science and Engineering, Kansai University, 3-3-35 Yamate-cho, Suita, 564-8680, Japan.

5 Faculty of Societal Safety Sciences, Kansai University, 7-1 Hakubai-cho, Takatsuki, 564-8680, Japan.

6 Nihon Superior Co., Ltd., 1-16-15 Esaka-cho, Suita, 564-0063, Japan.

Roughly one-quarter of coral reefs worldwide are already damaged beyond repair, and another two-thirds under serious threat. Up to now, several restoration techniques of corals such as fragmentation, farming, Biorock have been developed and implemented for such issues in the past few years. In vertebrates such as mammals, osteoblast is known to form bone composed of hydroxyapatite. In hard corals, on the other hand, polyps covered on the skeletons made of calcium carbonate has osteoblasts as well. Although the substances of the skeleton are different, the mechanisms of their formation are almost identical. Titanium (Ti) and its alloys have been widely used as biomaterials for orthopaedic and dental implants because their surfaces can promote osteoconduction after suitable surface modifications. The top surface is known to be titanium dioxide (TiO₂). The purpose of this work was to investigate the potential of Ti and TiO₂ as scaffolds for immobilising polyps. The corals (*Pocillopora damicornis* sp., imported from Australia) were divided into the short fragments with a size of about 5 mm using a diamond aqua saw. The fragments were placed in a small 3L tank which was filled with the artificial seawater. The salinity was increased by natural evaporation or by addition of high-salinity seawater. The polyps were separated from the skeleton after a few hours, the obtained ones were seeded on the substrates. The separated polyps preferentially adhered to the TiO₂ surface and expanded vigorously. Interfacial analysis between the polyps and the substrates was carried out in order to understand the adhesion process by means of Quartz Crystal Microbalance. Up to 8 h after the seeding of polyps, the resonant frequency and resistance decreased and increased, respectively. The adhesion and expansion of the polyps to/on the substrates could be detected.

Keywords: bone formation, CP-Ti, TiO₂, surface modification, polyps.

1. Background and objectives

In recent years, coral reefs have been exposed to catastrophic conditions due to rapid climate change and several factors. Roughly one-quarter of coral reefs worldwide are already damaged beyond repair, and another two-thirds under serious threat [1]. Up to now, several restoration techniques of corals such as fragmentation, farming, Biorock have been developed and implemented for such issues in the past few years [2-4]. Unfortunately, no breakthroughs have been achieved. In vertebrates such as mammals, osteoblast is known to form bone composed of hydroxyapatite, Ca₁₀(PO₄)₆(OH)₂. In hard corals, on the other hand, polyps covered on the skeletons has osteoblasts as well and they produce calcium carbonate, CaCO₃. Although the substances of the skeleton are different, the mechanisms of their formation are almost identical. Titanium (Ti) and its alloys have been widely used as biomedical materials for orthopaedic and dental implants because of their excellent mechanical property and biocompatibility. The surfaces can promote osteoconduction after suitable surface modifications [5-7], the top surface is known to be titanium dioxide (TiO₂). In addition, Ti is an essential material in marine-related fields, but its use is mostly focused on its corrosion resistance. If Ti can be used to induce coral skeletons at an early stage, this will lead to the expansion of titanium applications. In addition, although this research was conducted on corals, we

believe that it can also be used to control the attachment of shellfish and other marine organisms to artificial materials. The purpose of this work was to investigate the potential of Ti and TiO₂ as scaffolds for immobilising polyps referring to the findings obtained from previous studies on metallic biomaterials, bone formation and regenerative medicine technology.

2. Experimental procedure

2.1. Materials

Commercially pure Ti plates (ASTM grade 2, CP-Ti) were used in this study. The samples were thoroughly cleaned in acetone, deionised water and dried at 383 K. Some plates were anodised at 80 V in a 5 vol.% phosphoric acid aqueous solution at room temperature. All the samples were dipped in deionised water for 10 min and then dried at 383 K.

2.2. Coral rearing

Artificial seawater (RED SEA SALT, Red sea) with an ion concentration (Ca²⁺; 10-11, Mg²⁺; 51-54, K⁺; 9.6-10 mM) nearly equals to the real one was employed in the aquariums. Deionised water was used in the preparation. Salinity, pH and temperature were kept at 3.3-3.5%, 7.5-8.5 and around 298-299 K, respectively.

2.3. Characterisation

A The skeleton of corals was imaged by a micro-computed tomography (μCT) (inspeXio SMX-90CT Plus,

Shimadzu, Japan) at a tube current of 110 μ A, a tube voltage of 90 kV.

Changes in resonance frequency and resonance resistance were monitored by Quartz Crystal Microbalance system (QCM; QCA922, Seiko EG&G, Japan). They are corresponding to small mass and viscoelastic changes, respectively. The well cell made of PEEK (QA-CL4PK) and the quartz crystals with ITO (indium tin oxide) electrodes (QA-A9M ITO (M) (SEP), 7.9 \times 7.9 mm) were employed in this study. The base resonance frequency of the quartz crystal was 9 MHz. The thin layer of TiO₂ was deposited on the quartz crystal by the conventional RF magnetron sputtering (Kenix, Japan) using CP-Ti. Planula larva, just hatched from their eggs (*Stylophora sp.*), were seeded on the samples at 5-6 planula larva/700 μ L seawater and incubated at room temperature for almost 15 h including the stabilisations of the QCM.

3. Results and discussion

3.1. Expansion of soft tissue polyps on substrates

The CP-Ti plates were anodised in the aqueous phosphoric acid at 80 V in order to synthesise a thin layer of TiO₂. Corallites with polyps (*Galaxea fascicularis*) were fixed on CP-Ti, TiO₂-coated CP-Ti and kept in the lab-scale aquarium with artificial seawater. Figure 1 shows the appearance of the corallites on the plates after 120 days. In both cases, the polyps expanded vigorously, and the area tended to be slightly larger in CP-Ti. Tentacles in the centre of the polyp can be recognised by fluorescence when irradiated with ultraviolet light. The number of polyps proliferated by asexual reproduction was clearly higher in CP-Ti. The density of functional hydroxyl groups on TiO₂ is expected to have increased compared to CP-Ti. The increase in OH groups results in stronger adhesion of the polyps to the substrates. The strength of polyp adhesion on the surface was adequate in CP-Ti, which would have promoted adhesion and asexual reproduction of polyps. In other words, the adhesion of polyps to the substrate might be too strong on TiO₂. The effect of surface roughness on the adherence behaviour of the polyps to the substrate was also investigated. Although the results are not shown, it was observed that rougher surfaces tended to adhere to the substrate earlier. Furthermore, when TiO₂ thin layer was synthesised on the surface by the anodic oxidation, the onset of adhesion was about 1 h earlier than for the CP-Ti. The interface between the polyps and the substrates was observed by μ CT. New skeletal formations were clearly observed, which were directly connected to the original skeleton and to the substrates. These results suggest a high affinity between titanium and corals.

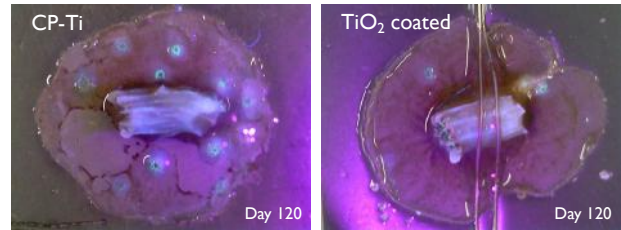


Figure 1. Corallites on CP-Ti and TiO₂ coated CP-Ti plates after 120 days incubation.

3.2. Separation of polyps from the skeleton

Generally, enzymes such as trypsin are used to separate cells from the soft tissue of a living body in the field of regenerative medicine. It has been reported that when corals receive sublethal environmental stress such as seawater temperature rise, salinity rise, oxygen concentration drop, pH drop and mechanical stimuli, the polyps try to escape the environments. It is known as the stress bailout reaction [8-10]. The stress avoidance response of polyps was artificially introduced in the coral fragments by increasing the salinity of the seawater. These are polyps that detach from the skeleton due to increased salinity (Fig.2). The bonded area among polyps become thinner, exposing the skeleton, and the polyps can be observed to gradually detach from the skeleton. When salinity increases rapidly, polyps are unable to keep up with the changes and die. When the salinity increases too slow, on the other hand, it takes longer to induce bailout reaction, resulting in a higher total burden on the polyps. Active polyps could be obtained by dropping seawater with 8.0% salinity into normal one with 3.5%, which was enriched to about 5.5% in 5 h. The time required for the polyp bailout using the stress avoidance response was strongly dependent on the structure of skeleton. Figure 3 shows a CT image of a coral skeleton (*Pocillopora damicornis sp.*). Dashed circle indicates corallite, which is the home of the polyps. The shorter the distance among the corallites and the larger the aperture diameter, the shorter the time required for bail-out.

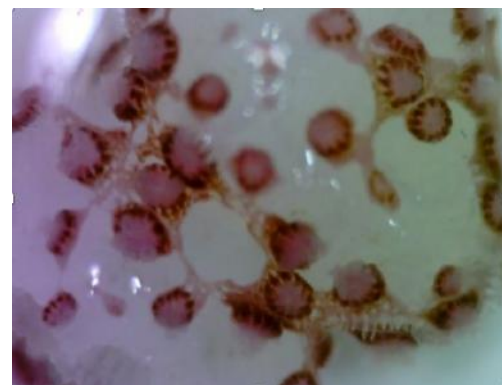


Figure 2. Polyp bailout response to increased salinity in the fragment of corals (*Pocillopora damicornis sp.*).

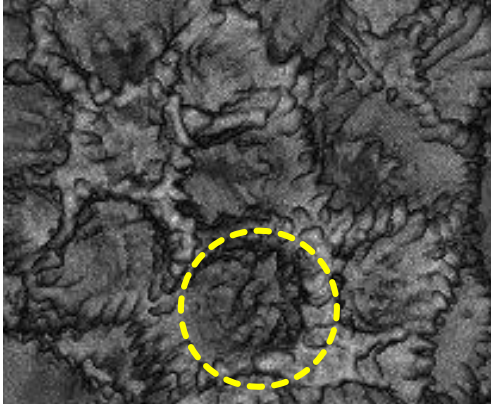


Figure 3. CT image of coral skeletons (*Pocillopora damicornis* sp.). The dashed circle indicates the corallite.

3.3. Interface analysis of coral/artificial materials

QCM is used for measuring a mass variation per unit area by measuring the change in frequency of a quartz crystal resonator. Therefore, it is widely employed as a good indicator for a biomolecular interaction on the material surfaces in-situ real-time and quantitatively. Recently, it has also been applied to analyse cell-material interactions [11,12]. Basically, a decrease in resonance frequency (F) indicates an increase in mass due to adsorbates on the surfaces, and an increase in resonance resistance (R) indicates an increase in viscosity of liquid in contact with the quartz crystal. In the present study, QCM method was employed to detect several behaviours at the interface between the coral soft tissue and the substrates.

TiO₂ was coated on the quartz crystals with ITO electrodes by the conventional RF sputtering. This TiO₂ film mimics the surface of Ti as well as TiO₂. The film, as well as the ITO, is colourless and transparent, so that the adhesion of the polyps can be observed from the back of samples. When distilled water was added to the well cell with the quartz crystals, the F and the R showed almost constant. By adding the artificial seawater corrected from the aquarium and seeding the planula larva to the well cell, in contrast, the F decreased, and the R increased.

The R was replotted against the F . This is commonly referred to as the F - R diagram (Fig. 4). Basically, these plots move from right to left over time and these changes can be divided into two types. In the case of seawater alone, the F decreased without much change in the R . Therefore the change shows horizontal. In the case of seawater with some planula, on the other hand, the F decreased and the R increased. Therefore the plot shifted to the upper left. These two changes might

correspond to protein adsorption from the seawater to the surface and the proximity/partial attachment of planula larvae to the surface, respectively. Changes in F and R over time could be also measured in the isolated polyps by using the stress avoidance response. Although further studies are required, this must be a powerful technique for analysing several behaviours at the interfaces between the corals and their scaffolds.

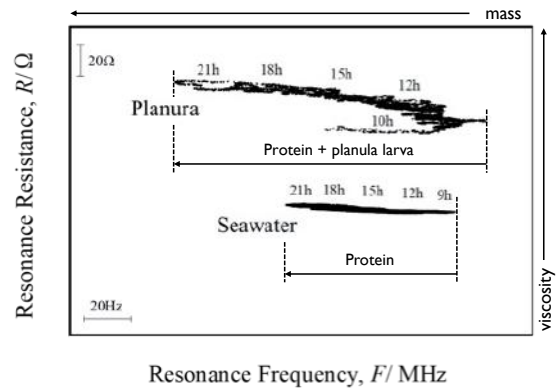


Figure 4. The F - R plots of seawater corrected from the aquarium and the seawater with some planula larva on TiO₂ films.

3.4. Trials at sea

Marine trials were conducted on Yoron island, Kagoshima prefecture. Good conditions for coral growth are still maintained. Fragments of corals (*Acropora* sp.) were fixed on the CP-Ti plates (40 mm square) and the anodised CP-Ti plates using SUS304 wires. Then the sets of samples were fixed to blocks placed on the seabed at a depth of approximately 2.5 m (Fig. 5). In the present marine test, vigorous polyp expansion and skeletal growth were observed on the CP-Ti and anodised CP-Ti surfaces.



Figure 5. Coral propagation platforms installed in the ocean (Yoron Island, Kagoshima, Japan).

Mortal is generally used as the base for coral transplantations. This is because it is the cheapest and closest artificial material to nature. Therefore the CP-Ti plate was glued on the surface of the mortar base. Then the fragment of coral was fixed on the CP-Ti plate with

SUS304 wire. Coral growth occurred along the Ti plate (Fig.6). This implies the coral growth was clearly faster and more desirable than that of mortar. This is thought to be due to the faster adhesion of coral soft tissue to the substrate and early stabilisation of corals on Ti. The superiority of Ti could be confirmed by the offshore test.



Figure 6. An example of a coral growing on CP-Ti in the offshore (Yoron Island, Kagoshima, Japan). CP-Ti plate was glued on the surface of the mortar base. The fragment of coral was fixed on the CP-Ti plate with SUS304 wire.

4. Summary

The potential of Ti and TiO₂ as scaffolds for proliferating coral reefs was investigated by analysing several interfacial reactions. The following conclusions were reached:

- (1) The polyps expanded vigorously on both CP-Ti and TiO₂. The area of expansion tended to be slightly larger in CP-Ti. The number of polyps proliferated by asexual reproduction was clearly higher in CP-Ti. New skeletal formations were clearly observed at the interface between corals and the substrates.
- (2) The stress avoidance response of polyps could be artificially introduced in the coral fragments by increasing the salinity of the seawater. Active polyps could be obtained by dropping seawater with 8.0% salinity into normal one with 3.5% under the appropriate salinity increase rate.
- (3) Protein adsorption and coral soft tissue adhesion behaviours on the surfaces could be detected by QCM technique.
- (4) Coral growth occurred along the Ti plate. The superiority of Ti in the growth could also be confirmed in the marine tests held in Yoron island, Kagoshima.

5. Acknowledgements

This work was financially supported by Grants-in-Aid for Scientific Research (21H05197, 22K19879) from the Ministry of Education, Culture, Sports, Science and Technology (MEXT) of Japan and the Light Metal Educational Foundation, Inc.. We are grateful to Kimiya Honma, Seiichi Saisho, Hiromitsu Kisaku, Akihiko Ohgane, Mitsutaka Ohta and Yoron Fisheries Cooperative Association for the offshore testing in Yoron island, Kagoshima, and also grateful to Chihiro Saruwatari for data management.

6. References

1. K.E. Carpenter, et al., *Science* 321 (2008) 560-563.
2. R.C. Babcock, et al., *Marine Biology* 90 (1986) 379-394.
3. C. Henderson, *New Scientist* (2002).
4. C.A. Boch, A.N.C. Morse, *Ecological Engineering* 40 (2012) 11-17.
5. T. Kokubo, F. Miyaji, H.M. Kim, T. Nakamura, *Journal of the American Ceramic Society* 79 (1996) 1127-1129.
6. M. Ueda, M. Ikeda and M. Ogawa, *Mater. Sci. Eng. C* 29 (2009) 994-1000.
7. M. Ueda, Y. Sasaki, M. Ikeda, M. Ogawa, W. Fujitani, T. Nakano, *Mater. Trans.* 50 (2009) 2147-2153.
8. P.W. Sammarco, *Marine Ecology-Progress Series*, 10 (1982) 57-65.
9. A.J. Fordyce, *F1000Research* 6 (2017) 687.
10. O.H. Shapiro, et al., *Nature Communications*, 7 (2016) 10860.
11. H.W. Kang, et al., *Analytica Chimica Acta* 2 (2008) 154-161.
12. K. Kushiro, et al., *Biomaterials Science* 4 (2016) 989-997.

FABRICATION OF CARBON-DOPED TiO₂ LAYERS VIA Ti OXIDATION AND EVALUATION OF THEIR ANTIBACTERIAL ACTIVITY

Ryusuke Koizumi¹, Kyosuke Ueda¹, Koyu Ito², Kouetsu Ogasawara², and Takayuki Narushima¹

¹ Department of Materials Processing, Graduate School of Engineering, Tohoku University, 6-6-02 Aza Aoba, Aramaki, Aoba-ku, Sendai, Miyagi 980-8579, Japan.

² Department of Immunobiology, Institute of Development, Aging and Cancer, Tohoku University, 4-1 Seiryomachi, Aoba-ku, Sendai, Miyagi 980-8575, Japan.

The visible-light-responsive photocatalytic activity of TiO₂ has the potential to facilitate the antibacterial functionalization of dental implants. In this study, TiO₂ layers were fabricated on commercially pure (CP) Ti substrates using a two-step thermal oxidation process involving carbonization (1st step), followed by oxidation (2nd step). The anatase fraction of the TiO₂ layers decreased with increasing 2nd-step temperature. In the 2nd step, carbon was introduced into the TiO₂ layer by optimizing 2nd-step temperature. The carbon-doped TiO₂ layers exhibited antibacterial activity against *Escherichia coli* under short-duration visible-light irradiation (15 min). The carbon introduced into the TiO₂ layer contributes to its visible-light response by decreasing its bandgap energy. Thus, the carbon-doped TiO₂ layer has the potential for the antibacterial functionalization of the Ti surface.

Keywords: Visible-light response, photocatalysis, carbon, titanium dioxide, biomedical.

1. Introduction

Ti exhibits excellent corrosion resistance and mechanical properties. In addition, Ti is recognized as a biomaterial owing to its osseointegration, a direct bond with the bone at the optical microscope level [1,2], and is widely used in dentistry. Ti dental implants have a high survival rate between 90% and 96% for up to 10–15 years after placement [3]. However, intraoral bacteria adhere to Ti implants that are exposed to the oral cavity and carry the risk of infections such as peri-implantitis. Notably, the risk of peri-implantitis 3.4–11 years after Ti implant placement is 22% [4]. Therefore, the antibacterial functionalization of Ti implant surfaces is required for the prevention and treatment of infections. TiO₂ exhibits antibacterial activity under ultraviolet (UV) irradiation owing to its photocatalytic activity [5], which reduces its susceptibility to infections [6]. However, UV irradiation being detrimental to the human body, the study of the photocatalytic activity of TiO₂ under visible-light irradiation is important. The addition of light elements, such as carbon and nitrogen, to TiO₂ enhances its visible-light responsivity [7,8].

Our group fabricated carbon-doped TiO₂ layers on commercially pure (CP) Ti using a two-step thermal oxidation process involving carbonization with CO gas (1st step), followed by oxidation in air (2nd step) [9,10]. The TiO₂ layers exhibited antibacterial activity under visible-light irradiation [11]. However, only antibacterial activity over a long duration (4 h) has been investigated; therefore, antibacterial activity over short irradiation periods must also be investigated to reduce patient burden. In this study, the effects of the 2nd-step conditions of the two-step thermal oxidation process on the structure of TiO₂ layers were investigated and their antibacterial activity over a short irradiation period was evaluated.

2. Materials and methods

2.1. Fabrication of TiO₂ layers

Single-sided mirror-polished CP Ti (Grade 2) plates, 12 mm in diameter, were used as the substrates. Figure 1 shows the schematic of the two-step thermal oxidation process. The substrates were carbonized (Ar-1% CO, 1073 K, 1 h) during the 1st-step treatment. During the 2nd step, the substrates were oxidized in air (at 573–923 K for 3 h). The treatment conditions in the 1st step were fixed, while the temperatures during the 2nd step were varied.

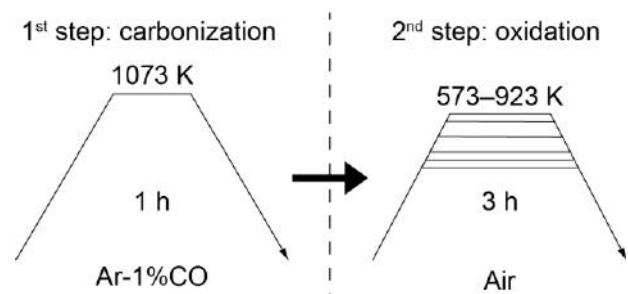


Figure 1. Schematic of two-step thermal oxidation.

2.2. Characterization of the layers

The surface reaction layers formed in each step were identified using X-ray diffraction (XRD; Smart Lab, Rigaku Co.). The anatase fraction (f_A) in the TiO₂ layer was calculated using Equation (1) [12]:

$$f_A = I_A / (I_A + 1.26 I_R), \quad (1)$$

where I_A and I_R are the maximum peak intensities of the anatase and rutile phases in the XRD patterns, respectively. The cross sections of the reaction layers were observed using scanning electron microscopy (SEM; XL-30FEG, Royal Philips Electronics Inc.). The chemical compositions and concentrations of the TiO₂

layers were analyzed using X-ray photoelectron spectroscopy (XPS; AXIS-ULTRA DLD, Shimadzu Co.).

2.3. Evaluation of antibacterial activity

The antibacterial activity of the TiO₂ layers under visible-light irradiation was evaluated using the glass cover method [11,13]. Figure 2 illustrates the procedure used for the antibacterial activity test. *Escherichia coli* (*E. coli*) was used as the bacteria, with a concentration of 10⁸ CFU (colony forming unit)·mL⁻¹. Firstly, 5 μL of the bacterial suspension was dropped onto three specimens, which were then covered with a glass plate. Subsequently, each specimen was immediately collected, irradiated with visible light, and placed in the dark. Visible-light irradiation and placement in the dark were each controlled at an intensity of 15 mW·cm⁻² for 15 min. The bacterial suspensions were thereafter collected in phosphate-buffered saline (PBS). The bacterial viable numbers in the specimen after immediate collection, visible-light irradiation, and placement in the dark, referred to as N_0 , N_{vis} , and N_{dark} , respectively, were counted using the plate dilution method. The normalized numbers of viable bacteria, N_{vis}/N_0 and N_{dark}/N_0 , were calculated for visible-light irradiation and placement in the dark, respectively. Statistical analysis was performed using the t-test for the logarithm of the normalized number of viable bacteria.

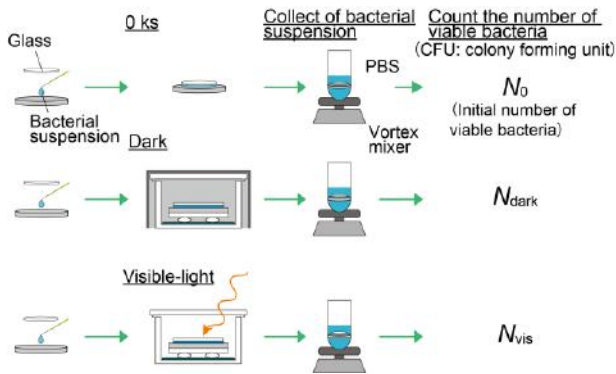


Figure 2. Schematic of the antibacterial activity test conducted using the glass cover method.

3. Results and discussion

3.1. Phase of TiO₂ layers

Figure 3 shows the XRD patterns of the reaction layers formed on the Ti substrate after each treatment step. As shown in Figure 3 (a), after the 1st step of treatment, reflection peaks between TiC and TiO were observed. The same peaks were reported for Ti(C,O), where a portion of the carbon in TiC was replaced by oxygen [14]. Therefore, Ti(C,O) was formed after the 1st step of carbonization. As shown in Figure 3 (b), during the 2nd step of oxidation, TiO₂ was formed when the temperature

was >623 K. The temperature of 573 K maintained during the 2nd step was insufficient to convert Ti(C,O) into TiO₂ in air. The anatase and rutile phases of TiO₂ were both detected; their fractions depended on 2nd-step temperature. Figure 4 shows the effect of 2nd-step temperature on the anatase fraction of the TiO₂ layers. The anatase fraction decreased as the 2nd-step temperature increased. Single-phase rutile was formed at 923 K. Figure 5 shows the cross sections of the TiO₂ layers formed at 673 and 923 K. The formation of uniform and dense TiO₂ layers on the Ti substrates was observed after the 2nd-step treatments. Figure 6 shows the thicknesses of the reaction layers formed after the 2nd step. The thickness of the TiO₂ layers increased as the 2nd-step temperature increased from 673 to 923 K. The layer thicknesses at 623 and 673 K were almost the same (approximately 0.5 μm) because the oxidation of the Ti(C,O) layers almost ended at these temperatures, while the further oxidation of the CP Ti substrates occurred at 773 to 923 K.

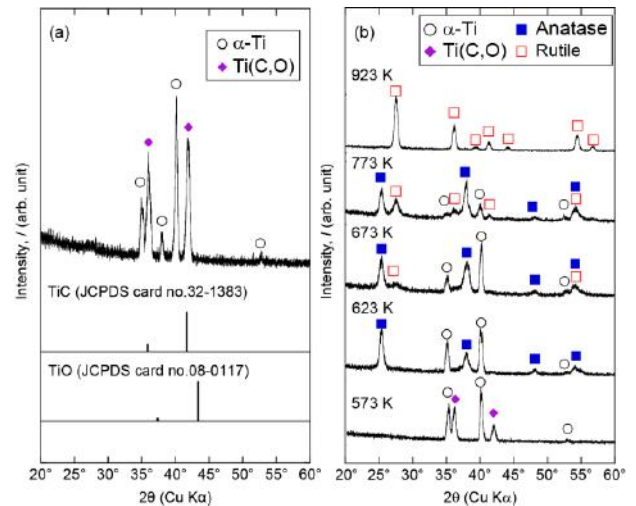


Figure 3. XRD patterns of reaction layers formed after the (a) 1st and (b) 2nd steps.

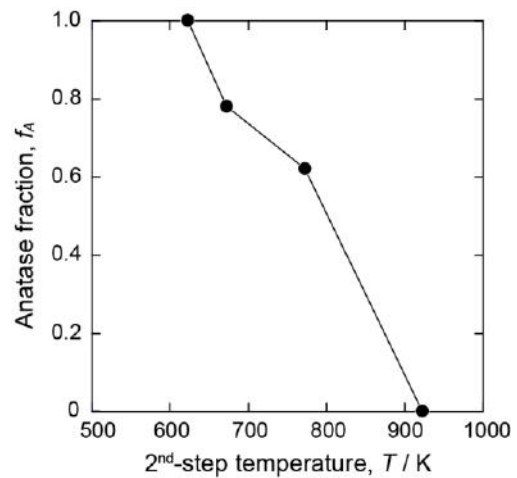


Figure 4. Effect of 2nd-step temperature on the anatase fraction of the TiO₂ layers.

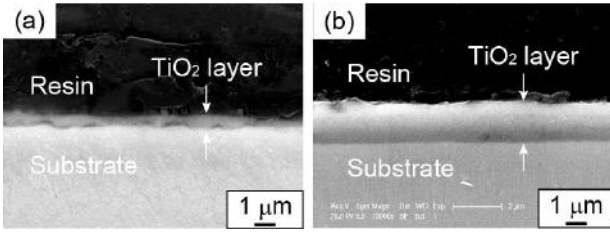


Figure 5. Cross-sectional SEM images of the TiO₂ layers formed at (a) 673 K and (b) 923 K after the 2nd step.

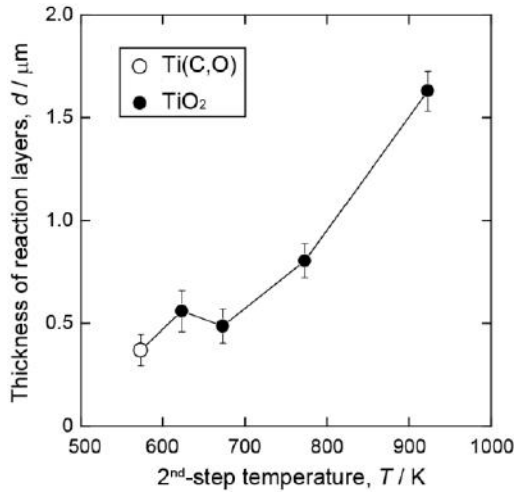
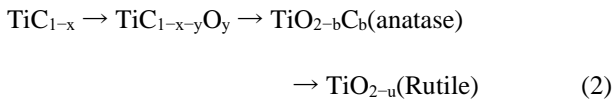


Figure 6. Effect of 2nd-step temperature on the thickness of the reaction layers.

Figure 7 shows the XPS depth profiles of carbon near the surface of the TiO₂ layers, 50–100 nm in size, formed after the 2nd step at 673 and 923 K. In both cases, a high carbon concentration, caused by surface-contaminated hydrocarbons, was detected on the outermost surface. Carbon was also detected inside the TiO₂ layer formed after the 2nd step at 673 K, as shown in Figure 7 (a). The carbon concentration near the surface of the TiO₂ layer was 1–3 mol%. However, carbon was not detected in the TiO₂ layer formed after the 2nd step at 923 K, as shown in Figure 7 (b).

Shabalin et al. [15] proposed the following equation for TiC_{1-x} oxidation.



As shown in Figure 4, an anatase-rich layer was formed after the 2nd step at 673 K, indicating that the remaining carbon was dissolved in TiO₂. However, when in the 2nd step, single-phase rutile was formed at 923 K, carbon was removed from TiO₂ owing to the anatase–rutile transformation at the high oxidation temperature of 923 K.

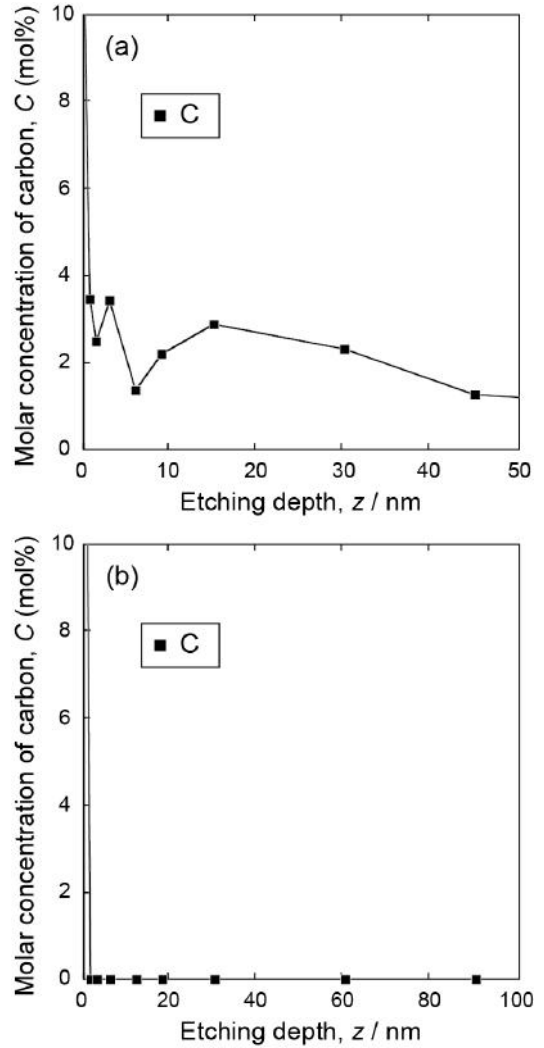


Figure 7. XPS depth profile of the carbon molar concentration of the TiO₂ layers at the 2nd-step temperatures of (a) 673 K and (b) 923 K.

3.2. Antibacterial activity of the TiO₂ layers under visible-light irradiation

Figure 8 shows the logarithms of the normalized numbers of viable bacteria in the TiO₂ layers fabricated at 2nd-step temperatures of 623, 673, and 923 K. The logarithm of the normalized number of viable bacteria after being placed in the dark ($\log(N_{\text{dark}}/N_0)$) for 15 min was approximately zero, independent of 2nd-step temperature, indicating that the number of viable bacteria had not decreased. In the case of the TiO₂ layer formed at 673 K after the 2nd-step, $\log(N_{\text{vis}}/N_0) \approx -1.6$, indicating antibacterial activity. However, in the TiO₂ layers formed at 623 and 923 K after the 2nd-step, no significant difference was observed in the logarithm of the normalized number of viable bacteria under visible-light irradiation or when placed in the dark.

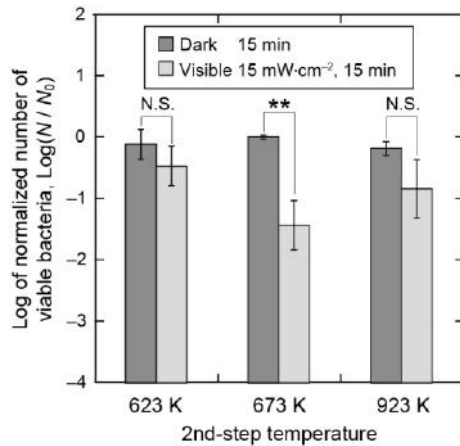


Figure 8. Logarithm of the normalized number of viable bacteria on the TiO₂ layers formed at the 2nd-step temperatures of 623, 673, and 923 K after visible-light irradiation or placement in the dark for 15 min. (** p < 0.01)

The TiO₂ layer fabricated at 673 K in the 2nd step contained carbon (Figure 7 (a)) and exhibited antibacterial activity under visible-light irradiation. Zhang et al. [16] proposed that the carbon in TiO₂ formed impurity levels, resulting in a decrease in the bandgap energy and an increase in visible-light responsivity. In this study, the carbon in the TiO₂ layer fabricated at the 2nd-step temperature of 673 K can be attributed to the antibacterial activity occurring under visible-light irradiation. The first principles calculations made by our group suggest that carbon introduced into anatase-type TiO₂ decreased its bandgap energy to 2.2 eV [17].

The TiO₂ layers fabricated at 623 and 923 K did not exhibit any antibacterial activity. As shown in Figure 3, only the anatase phase was detected in the TiO₂ layers fabricated at 623 K through the XRD analysis; however, Ti(C,O) presumably remained in the TiO₂ layers because of the low oxidation temperature and would act as a recombination site for the excited electrons and holes. Carbon was not detected in the TiO₂ layer fabricated at 923 K, suggesting that it did not respond to visible light.

4. Conclusion

Carbon-doped TiO₂ layers were fabricated on a Ti substrate using a two-step thermal oxidation process involving carbonization with CO gas, followed by oxidation. In the 2nd step, carbon was introduced into the TiO₂ layers by optimizing 2nd-step temperature. The carbon-doped TiO₂ layer exhibited antibacterial activity under short-duration visible-light irradiation (15 min). The carbon in TiO₂ contributed to its visible-light response. Therefore, the TiO₂ layers fabricated in this study could be used in the antibacterial functionalization of Ti dental implant surfaces, performed to prevent and treat infections.

5. Acknowledgements

The authors thank Ms. K. Omura of Tohoku University for performing the XPS analyses. This study was partially supported by the Grants-in-Aid for Scientific Research (KAKENHI) program of the Japan Society for the Promotion of Science (Grant number JP21H04603) and the program for the establishment of university fellowships for the creation of science and technology innovation (Grant number JPMJFS2102) of the Japan Science and Technology Agency.

6. References

1. P.-I. Brånemark, *The Journal of Prosthetic Dentistry* 50 (1983) 399–410.
2. P.I. Brånemark, B.O. Hansson, R. Asahi, U. Breine, J. Lindström, O. Hallén, A. Öhman, *Scandinavian Journal of Plastic and Reconstructive Surgery* 16 (1977) 1–132.
3. P.A. Norowski, J.D. Bumgardner, *Journal of Biomedical Materials Research Part B: Applied Biomaterials* 88 (2009) 530–543.
4. J. Derks, C. Tomasi, *Journal of Clinical Periodontology* 42 (2015) S158–S171.
5. K. Sunada, T. Watanabe, K. Hashimoto, *Journal of Photochemistry and Photobiology A: Chemistry* 156 (2003) 227–233.
6. J. Grischke, J. Eberhard, M. Stiesch, *Dental Materials Journal* 35 (2016) 545–558.
7. R. Asahi, T. Morikawa, T. Ohwaki, K. Aoki, Y. Taga, *Science* 293 (2001) 269–271.
8. A. Zaleska, *Recent Patents on Engineering* 2 (2008) 157–164.
9. T. Okazumi, K. Ueda, K. Tajima, N. Umetsu, T. Narushima, *Journal of Materials Science* 46 (2011) 2998–3005.
10. N. Umetsu, S. Sado, K. Ueda, K. Tajima, T. Narushima, *Materials Transactions* 54 (2013) 1302–1307.
11. T. Ueda, N. Sato, R. Koizumi, K. Ueda, K. Ito, K. Ogasawara, T. Narushima, *Dental Materials* 37 (2021) e37–e46.
12. R.A. Spurr, H. Myers, *Analytical Chemistry* 29 (1957) 760–762.
13. T. Ueda, K. Ueda, K. Ito, K. Ogasawara, H. Kanetaka, T. Mokudai, Y. Niwano, T. Narushima, *Journal of Biomedical Materials Research Part A* 107 (2019) 991–1000.
14. S. Sado, T. Ueda, K. Ueda, T. Narushima, *Applied Surface Science* 357 (2015) 2198–2205.
15. I.L. Shabalina, D.L. Roach, L.I. Shabalina, *Journal of the European Ceramic Society* 28 (2008) 3177–3188.
16. L. Zhang, M.S. Tse, O.K. Tan, Y.X. Wang, M. Han, *Journal of Materials Chemistry A* 1 (2013) 4497.
17. T. Ishikawa, R. Sahara, K. Ohno, K. Ueda, T. Narushima, *Computational Materials Science* 220 (2023) 112059.

LOW TEMPERATURE GASEOUS SURFACE HARDENING OF TITANIUM

Magnus F. Grüner^{1,2,*}, Frederik Bojsen-Møller¹, Morten S. Jellesen², Marcel A.J. Somers², Thomas L. Christiansen²

1 Elos Medtech, Engvej 33, 3330 Gørløse, DK

2 Department of Civil and Mechanical Engineering, Technical University of Denmark, Produktionstorvet b425, 2800 Kgs Lyngby, DK.

Titanium and its alloys are extensively used for medical implants due to their favourable properties, such as biocompatibility, corrosion resistance and osseointegration. However, titanium's poor wear resistance limits its range of use. Recently developed thermochemical surface treated titanium, comprising of a low temperature nitriding process and a subsequent vacuum treatment, might substantially improve wear resistance and portray an alternative to the use of CoCr alloys. In this study, the established microstructure of CP grade-4 titanium subjected to the novel surface hardening treatment is characterized by light optical microscopy and X-ray diffraction. Furthermore, hardness response and mechanical properties are investigated and compared to those of a conventionally used Co-Cr alloy. The applied thermochemical surface treatment resulted in the formation of a Ti₂N compound layer atop a solid solution strengthened diffusion zone. Thus, a very large hardness increase of the surface with gradual decrease to a depth of up to 25µm was achieved. The combination of a large hardness increase with a potential reduction in friction coefficient due to the formation of a Ti₂N surface layer resulted in a generally enhanced wear performance. Ball-on-disc wear testing showed a reduction in the wear track of about 50% compared to untreated CP grade-4 titanium. This study demonstrated that the wear performance of the treated CP grade 4 titanium was superior to that of the benchmarked CoCr alloy. The results of this study indicate that the CP grade-4 titanium subjected to the applied thermochemical surface treatment presents a promising alternative to Co-Cr alloys. However, to ensure its reliability under actual implant service conditions further testing closer to actual service load and environment must be carried out.

Keywords: Surface treatment, nitriding, wear resistance, CP titanium, biomaterials, CoCr.

1. Introduction

Medical implants demand materials with exceptional properties, including biocompatibility, high strength as well as corrosion, wear and fatigue resistance properties. Bone replacement implants are just one example where the implant consists of multiple components, each of which has individual material requirements to reliably fulfil the component's function. Titanium or titanium alloys are the material of choice for most of such parts. However, poor wear resistance limits their use in applications, where loaded sliding contact of components are required or where fretting can occur, as reported at the femoral head in hip prosthesis. Therefore, CoCr alloys are conventionally used in metal-on-plastic hip replacement implants instead [1]. Yet, studies have shown elevated cobalt levels in more than half of the investigated patients with metal-on-plastic hip prosthesis concluding a potential release of cobalt during service [2]. Moreover, a in 2021 updated EU Medical Devices Regulation (MDR) considers Cobalt carcinogenic, mutagenic and toxic to reproduction [3]. Thus, there is a need for profound justification for the continued use of cobalt, and there is a strong demand for better technical alternatives, especially in the long term. A potential alternative constitutes wear-improved titanium, for example by thermochemical surface treatment. Gaseous nitriding of titanium in nitrogen-containing atmospheres is commercially well established and is used to improve wear properties of titanium and its alloys. The required high process temperatures result, however, in deformation, severe grain growth and the formation of a brittle, albeit hard, titanium nitride layer on the surface.

The latter presents a major limitation for implants, because of the high risk of spallation and debris formation [4]. Recent research advances in thermochemical processing of titanium may be a way forward, particularly a combination treatment of a boost gaseous surface nitriding step followed by a diffusion step in vacuum, at low temperatures, as shown in figure 1 [5], [6]. Conventional molecular nitrogen atmospheres behave inert at low temperatures, so the metastability of ammonia is exploited to achieve the desired uptake of atomic nitrogen. Equivalent to common nitriding in N₂, a compound layer consisting of TiN and Ti₂N forms atop a nitrogen diffusion zone with concentration gradient. In contrast to pure nitrogen atmospheres, however, also hydrogen diffuses into titanium during the boost nitriding step in ammonia. The subsequent diffusion step leads to further ingress of nitrogen and retraction of hydrogen. Furthermore, during the vacuum treatment the compound layer provides additional nitrogen for further ingress, by (partial) dissolution. Sufficient holding time in the vacuum step can result in complete dissolution of the TiN layer and retraction of dissolved hydrogen. After dissolution of TiN, a surface layer of metallic shining Ti₂N remains or dissolves as well on prolonged annealing. Underneath a diffusion zone has developed that contains more nitrogen and is deeper than after the first nitriding step. The present study investigates the evolved microstructure as well as the resulting hardness response of commercially pure grade-4 titanium subjected to the novel surface treatment. Additionally, the achieved wear performance is tested and compared to a state-of-the-art CoCr alloy.

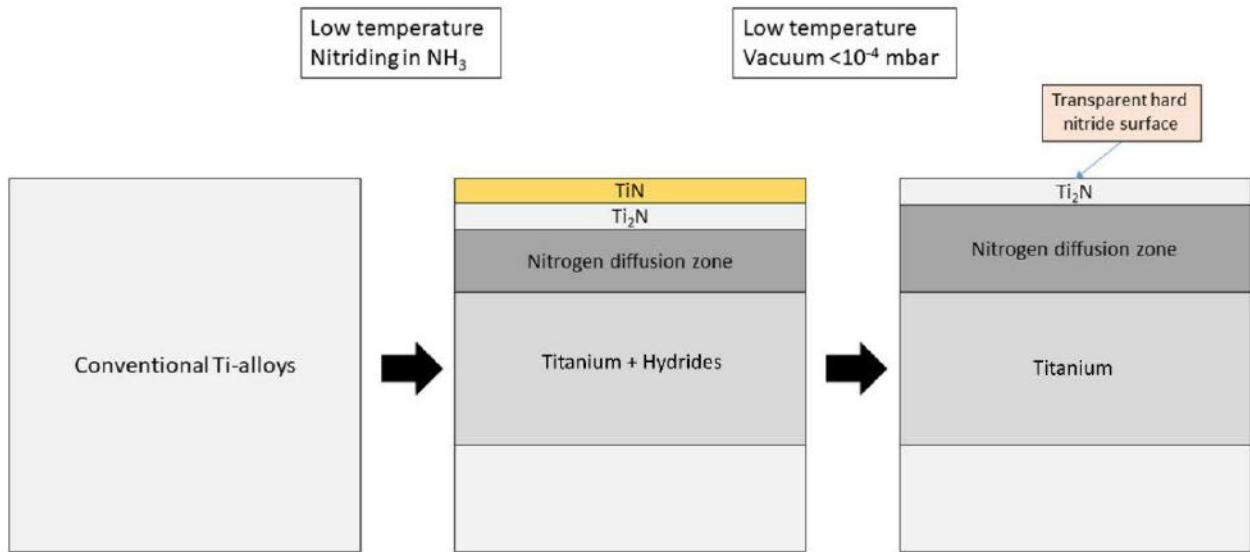


Figure 1. Schematic, cross-sectional overview of the investigated combination treatment of low temperature gaseous nitriding and subsequent vacuum treatment [6].

2. Materials and methodology

Commercially pure grade-4 titanium discs with a size of $\text{\O}15 \times 2 \text{mm}$ lathed from 16mm rods as well as ASTM F75 (Co-28Cr-6Mo) discs with a size of $\text{\O}12 \times 3 \text{mm}$ were used for the present experiments. All discs were ground with sandpaper under gradual use of finer grits up to 4000# SiC and subsequently polished with standard colloidal silica suspension (OP-U) to achieve a mirror finish.

2.1. Heat and surface treatment

2.1.1. Stress-relieving

The titanium discs were subjected to a vacuum stress-relief treatment at 640°C for 4h in a custom built Kanthal vacuum tube furnace equipped with an Edwards T-Station 85 vacuum pump station. The achieved vacuum was better than 10^{-4}mbar . Heating to treatment temperature as well as cooling to room temperature required 30 ± 5 minutes. Air cooling was facilitated by an external fan after removing the heat source.

2.1.2. Thermochemical surface treatment

Nitriding of the titanium discs was performed in a ceramic tube furnace with horizontal gas flow. The nitriding atmosphere consisted of $\text{NH}_3:\text{N}_2 = 2:1$. The atmosphere was established, after evacuating and backfilling the furnace with molecular nitrogen thrice to ensure the removal of ambient air and avoid oxidation. Afterwards, the furnace was heated within 30min to the nitriding temperature of 630°C and kept at treatment temperature for 20h. The specimens remained in the

nitriding atmosphere during slow cooling to room temperature within approx. 1.5h [5].

2.1.3. Diffusion vacuum treatment

The diffusion vacuum treatment after the boost nitriding treatment was executed in the same set-up as the vacuum stress-relief. The treatment was performed at 675°C for 24h [5].

2.2. Metallographic analysis

2.2.1. Light optical microscopy (LOM)

Cross-sections of the disc specimens were embedded in Struers LevoFast resin. Grinding and polishing of the cross-sections was conducted according to the procedure described for achieving the initial mirror finish. Cross-sectional microstructures were revealed by etching in Keller's reagent for approx. 7s. Imaging was performed on a Zeiss Axio Vert.A1 light optical microscope using polarized light and a 50x magnifying lens (Numerical Aperture = 0.75).

2.2.2. Phase analysis

X-ray diffraction for phase analysis was conducted on a Bruker D8 AXS X-ray diffractometer equipped with Cu-radiation ($\text{Cu-K}\alpha = 1.5418 \text{\AA}$). The measurements were performed in parallel beam geometry at a voltage of 40kV and a current of 40mA. The scans ranged from 30° to 80° over 2θ and were performed using a step size of $0.02^\circ 2\theta$ with a counting time of 2s.

2.3. Mechanical performance

Evaluation of mechanical properties of surface treated titanium was not performed on the as-nitrided specimens, but in the final condition after hydrogen removal.

2.3.1. Surface hardness measurement

Surface hardness was gauged by Vickers micro-hardness indentation using a Future-Tech FM-700 hardness tester. The indentation was applied top-down into the specimen surface for a dwell time of 10s with loads of 5g, 10g and 50g. Different loads were applied to average over different depth ranges to obtain information about a hardness gradient in the case. The indentations were measured at 100x magnification. All hardness values presented are an average over 3 indents.

2.3.2. Hardness profiling

Hardness profiles were acquired by nanoindentation using an CSM instruments NHT² nano-indenter equipped with a diamond Berkovich indenter. Before measurement the specimens were re-polished according to the previously described method aiming for a feature- and deformation-free preparation of the cross-section. Indents were placed to a constant depth of 500nm to minimize size effects; the dwell time was 5s. Thus, depending on the hardness, indentation loads varied from approx. 18 to 30mN. The final hardness profile was averaged over 5 indent matrices per sample. However, indents with discontinuities in the load-displacement curve and indents, showing deformation or close distance to microstructural features, such as grain boundaries, were disregarded. Additionally, the point of contact for each approved indent was manually corrected by inspection of the force-time curve. The final hardness profiles were fitted with an exponential decay function. The edge distance of every indent was measured by LOM.

2.3.3. Wear testing

Ball-on-disc wear testing was conducted on a CSM instruments TNR tribometer with the addition of phosphate buffered saline (PBS) solution as droplets and by using a zirconia ball (ZrO₂) of Ø6mm in diameter. The wear test was executed under an applied force of 2N over a wear radius of 3mm and a coverage angle of 75° for 2000 repetitions at 1Hz. Three replications were performed per condition. The induced wear tracks were inspected and measured using LOM.

3. Results and interpretation

3.1. Microstructure

Microstructures of CP grade-4 titanium discs as revealed by light optical microscopy of etched cross-

sections are presented in figure 2. The micrograph of the just stress-relieved condition as well as the microstructure in the core of the boost-nitrided and nitrided + vacuum treated specimen show microstructures consisting of α -Ti grains, as expected for an α -Ti alloy. Additionally, finely distributed Fe stabilized β -Ti regions can be seen, which are preferentially attacked by the etchant [7]. Dissolved nitrogen during the nitriding treatment is stabilizing α -Ti and has pushed iron further into the material. That results in the formation of a featureless surface zone consisting solely of nitrogen stabilized α -Ti with a thickness of about 8 μ m. The visual appearance of the nitrided specimen is golden, indicating the formation of titanium nitride TiN. However, the layer is probably too thin to be visible with LOM in the cross-section. The zone with increased etch-resistance comprises therefore solely of h.c.p. Ti with nitrogen in solid solution. The additional vacuum annealing extends this zone to a depth of 14 μ m. The microstructure in the core remained unaffected and only limited to no grain growth appears to have occurred.

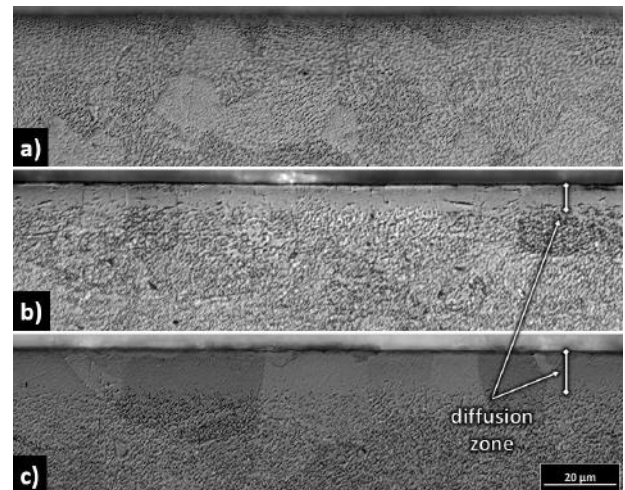


Figure 2. Cross-sectional light optical micrographs of CP grade-4 titanium discs after a) stress-relieving, b) + nitriding and c) + vacuum treating. The given scale bar applies for all micrographs.

3.2. Phase analysis

The measured diffractograms are displayed in figure 3. The diffraction pattern of the stress-relieved condition shows only peaks corresponding to α -Ti which is in good agreement with information obtained from the micrograph. The finely dispersed β -Ti regions are probably not detected due to the low fraction. Nitrogen uptake during nitriding can be confirmed by the presence of peaks corresponding to titanium nitride Ti₂N. Moreover, α -Ti diffraction peaks exhibit asymmetric broadening, which suggests a concentration profile of interstitially dissolved nitrogen. The peaks sensitive for the c lattice parameter (as the 013-peak in figure 3) are more affected by N dissolution, because the c direction of

the hcp unit cell expands more abundantly than directions in the basal plane on occupying octahedral interstitial sites by nitrogen atoms [8]. Despite the optical identification of the golden appearance of TiN, no diffraction evidence was observed. Potentially, the layer is too thin to be detected by the performed XRD measurements, as it is the case for LOM. Therefore, it is also not straightforward to prove the dissolution of the TiN layer during the subsequent vacuum treatment by XRD. However, additional Ti_2N peaks (e.g., at approx. $36^\circ 2\theta$) arise and existing Ti_2N peaks become more defined for the additionally boost vacuum treated condition. This can only occur if a reservoir for N has been present, as TiN.

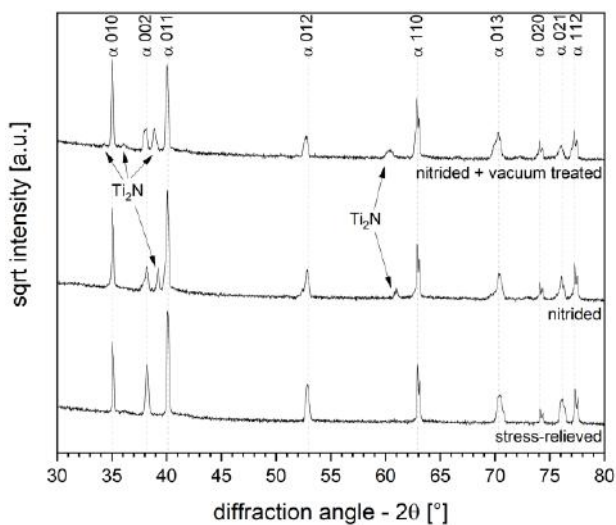


Figure 3. Diffractograms of CP grade-4 titanium discs after stress-relieving, + nitriding and + vacuum treating.

3.3. Hardness response

The top-down surface hardness of stress-relieved CP grade-4 titanium is $257 \pm 4HV0.05$. The hardness values increase sharply for lower loading forces, as shown in figure 4. These differences are partially attributed to the load dependence of micro hardness indentation. Additionally, the vacuum stress-relieving could have resulted in recrystallization of surface deformation induced during machining. Surface hardness measurements with lower loads might thereby be more affected due to their lower penetration depths. Surface hardening of titanium, comprising of nitriding followed by a vacuum treatment, results in a more than two-fold surface hardness increase to values up to almost 1000HV, when measured with 5g load. Indentation with higher loads yields gradually lower values for the surface hardness. To a certain extent, this is caused by the load dependency of microindentation, as mentioned previously. However, since increased loads also exhibit a deeper penetration and therefore information depth, lower

hardness values can be attributed to an expected hardness profile associated with a nitrogen concentration profile. The surface hardness of the CoCr alloy is gauged to approx. 450HV, which is harder than the stress-annealed CP grade-4 titanium. However, surface treating by means of gaseous nitriding elevated the surface hardness of titanium well above that of the inspected CoCr alloy in all applied loads. It is noted that the CoCr alloy possesses this intermediate hardness level also in the bulk of the material, thus, throughout the whole cross-section. Surface hardened titanium exhibits the mentioned hardness increase only in a shallow depth range.

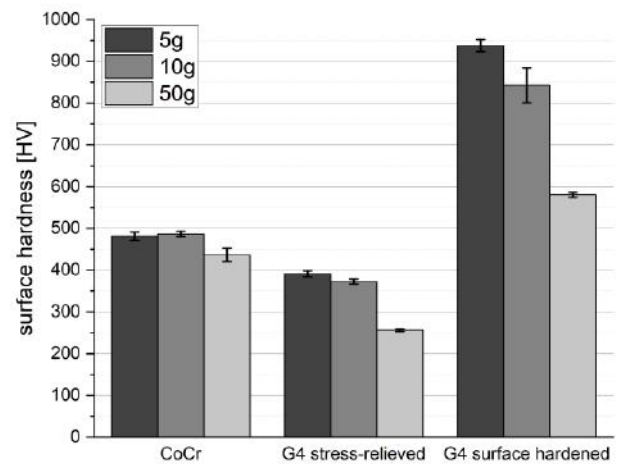


Figure 4. Top-down surface microhardness measurements according to Vickers with various loads of CoCr as well as CP grade-4 titanium in stress-relieved and nitride + boost vacuum treated condition.

The affected hardening zone was gauged by nanoindentation. The converted indentation hardness displayed over the edge distance is presented in figure 5. The hardness profiles of both conditions show a gradual decrease from a maximum hardness close to the surface down to the actual core hardness in the bulk of the material. A similar gradient is expected for the concentration of interstitial nitrogen. Thus, the hardness increase can directly be attributed to interstitial solid solution strengthening. The boost-nitrided condition shows to be affected by elevated hardness to a depth of approx. $15\mu m$. The additionally applied vacuum treatment shifts the profile to an elevated depth of about $25\mu m$. Thus, the added vacuum treatment leads to additional ingress of nitrogen. The hardness profile is thereby not flattened, but rather moved to higher edge distances, which results in an increased area under the curve. Therefore, it must be concluded that more nitrogen is interstitially dissolved. Thus, the disappearance of the golden TiN layer is concluded to have been the reservoir where nitrogen was stored during boost nitriding [6]. Moreover, the bulk hardness of the as-nitrided condition appears to be higher than of the additionally vacuum

treated condition. The reduction in core hardness cannot be attributed to grain growth. During nitriding in ammonia, also hydrogen diffuses into titanium. The higher diffusivity of hydrogen in the titanium lattice entails significantly larger diffusion depths for hydrogen than for nitrogen [9]. Thus, the reduction in core hardness during the added vacuum treatment could be caused by the removal of hydrogen, which served as solid solution strengthener in the bulk. Hence, the subsequent vacuum step serves not only as dissolution step for the formed TiN nitride layer, which is a diffusion barrier for hydrogen, but also as hydrogen extraction step.

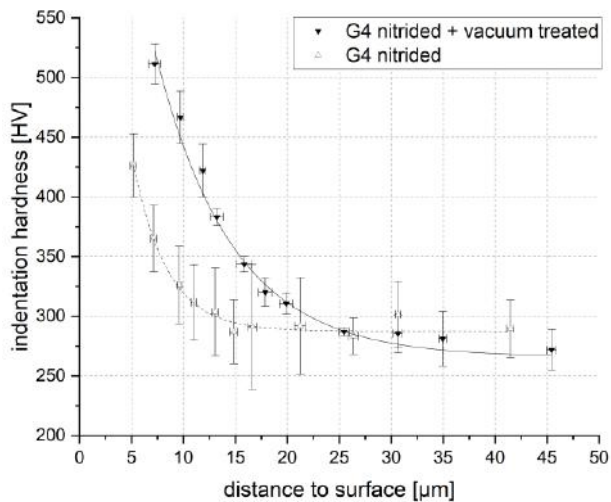


Figure 5. Hardness profiles of CP grade-4 titanium discs in nitrided and nitrided + vacuum treated condition gauged with nanoindentation.

3.4. Wear performance

Wear track widths of ball-on-disc wear tests are displayed in figure 6. A broader wear track implies a greater amount of wear. The wear track of the stress-relieved CP grade-4 titanium specimen has a width of $316 \pm 31 \mu\text{m}$, which is about twice the width of the wear track of the CoCr alloy. Thus, the test confirms that untreated CP titanium exhibits poor wear resistance. Surface hardened CP grade-4 titanium shows, however, a significant reduction in the wear track width to $142 \pm 8 \mu\text{m}$. Hence, the measured wear performance of treated titanium is enhanced to a level exceeding that of the CoCr alloy, based on the chosen tribometer conditions. Due to the increased hardness of the specimen, the zirconia ball could have predominantly suffered from wear instead. However, inspection of the zirconia balls revealed no considerable signs of wear.

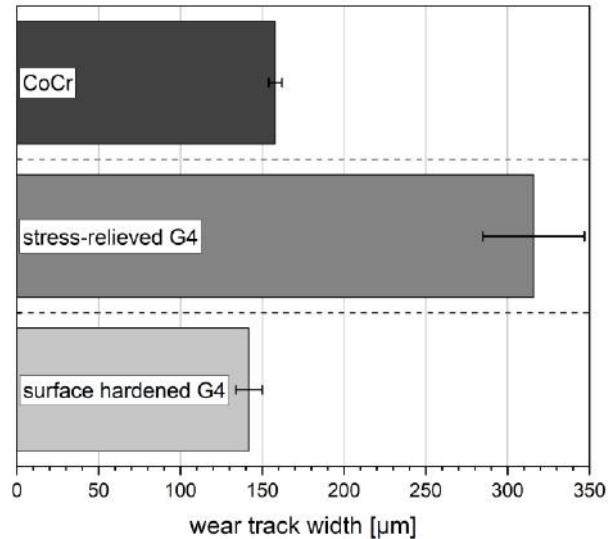


Figure 6. Wear track widths of wear tested samples made from CoCr as well as CP grade-4 titanium in stress-relieved and nitrided + vacuum treated condition.

4. Discussion

4.1. Surface hardening process

Ferritic nitriding in ammonia is well established to enhance wear resistance of various steels by the formation of a nitrogen enriched subsurface zone and a compound layer atop a substrate. Equivalently, nitriding of titanium in an ammonia atmosphere results in the formation of a mixed intermetallic layer, consisting of golden TiN and metallic shining Ti_2N , and a supporting, solid solution strengthened subsurface with a nitrogen concentration gradient underneath. However, a stand-alone nitriding process in ammonia is not recommended for industrial applications due to titanium's high affinity for hydrogen, and thus instant uptake of hydrogen into solid solution, entailing an increased risk of failure caused by hydrogen embrittlement. The added vacuum treatment could be performed at low temperatures, at which hydrogen is mobile, yet kinetics for nitrogen diffusion is limited. Thereby, detrimental hydrogen is removed, while the nitride layer remains intact to serve in applications with severe wear. Vacuum treating at higher temperatures, as shown in this study, results additionally in the dissolution of the TiN nitride layer, serving as a nitrogen reservoir for further solid solution strengthening. Latter results in the recuperation of the metallic luster and therefore represents the preferred treatment for implants, as a hard, but brittle TiN layer bears the risk of spallation and debris formation [4]. Since the processes are diffusion based, further tailoring of the concentration gradient, and thereby the hardness profile, can be realized by adjustments of process parameters i.e., time and temperature [10].

4.2. Wear performance

The surface hardening treatment reduced the wear track width to less than half compared to the untreated CP grade-4 titanium. That might primarily be attributed to the significant hardness increase of the surface and the supportive layer. Additionally, Ti₂N, as preserved microstructure constituent in the outermost layer, might cause a reduction in the friction coefficient and thus positively influence the contact wear behaviour [11]. It is noted, that once actual wear commenced, the wear resistance is expected to decrease over the course of the wear test, as high hardness and the presence of Ti₂N decline with increasing edge distance. Under the applied test conditions, the surface hardened titanium presents a viable alternative to the conventionally used CoCr alloy. The wear test showcases a simplified situation and, admittedly, does not represent the real load situation of i.e., specific joint replacement implants. Furthermore, it is of interest to investigate how surface hardened titanium performs, when multiple mechanisms, such as wear and corrosion, act synergistically, as it is commonly the case in service.

5. Conclusion

Based on the results of the present investigations, the following conclusions can be drawn:

1. The presented surface hardening treatment results in the formation of a substantially hardened surface layer, while maintaining the metallic luster of the titanium specimen.

2. The achieved case consists of a metallic Ti₂N atop a diffusion zone that is solid solution strengthened by nitrogen.

3. The wear performance of CP grade-4 titanium is substantially enhanced, also to a level better than that of the referred CoCr alloy. Potentially, the large hardness increase of the surface assisted by a lowered coefficient of friction, contribute to enhanced tribological performance.

4. The used tribometer test is not representative for complex real-life implant applications. Further testing, respecting synergistic degradation mechanisms, is required.

6. Acknowledgements

We are grateful to the Innovation Foundation Denmark for partial funding through grant number 2050-00010B.

7. References

- [1] A. Jahan, K. L. Edwards, and M. Bahraminasab, *Case studies of materials selection and design*. 2016.
- [2] S. S. Tower, C. S. Cho, R. L. Bridges, and B. D. Gessner, "Prevalence of Cobalturia among Adults with Joint Replacements," *JAMA Netw. Open*, vol. 4, no. 8, pp. 2021–2024, 2021, doi: 10.1001/jamanetworkopen.2021.21758.
- [3] W. K. L. Chan, "Regulatory framework," *Prof. Hous. Manag. Pract. Hong Kong*, no. 7440, pp. 33–46, 2006, doi: 10.4324/9781315758091-6.
- [4] J. Komotori, B. J. Lee, H. Dong, and P. A. Dearnley, "Corrosion response of surface engineered titanium alloys damaged by prior abrasion," *Wear*, vol. 250, no. 251, pp. 1239–1249, 2001, doi: 10.1016/S0043-1648(01)00753-0.
- [5] T. L. Christiansen, M. S. Jellesen, M. A. J. Somers, A. F. K. Körkel, and O. Z. Andersen, "Surface hardening of group IV metals," *WO 2022184812 A1*, 2022.
- [6] A. F. K. Körkel, "Surface engineering of titanium and titanium alloys for dental applications," Ph.D. Thesis, Technical University of Denmark, 2022.
- [7] F. B. Kværndrup, K. V. Dahl, D. Poquillon, K. Ståhl, M. A. J. Somers, and T. L. Christiansen, "Kinetics of interstitial uptake during gaseous carbo-oxidizing of titanium foils," *Thermochim. Acta*, vol. 703, no. April 2021, p. 178991, 2021, doi: 10.1016/j.tca.2021.178991.
- [8] H. A. Wriedt and J. L. Murray, "The N-Ti (Nitrogen-Titanium) System," *Bull. Alloy Phase Diagrams*, vol. 8, no. 4, pp. 378–388, 1987.
- [9] U. Zwicker, *Titan und Titanlegierungen*. 1974.
- [10] A. Zhecheva, S. Malinov, and W. Sha, "Titanium alloys after surface gas nitriding," *Surf. Coatings Technol.*, vol. 201, no. 6, pp. 2467–2474, 2006, doi: 10.1016/j.surfcoat.2006.04.019.
- [11] S. Lavrys, I. Pohrelyuk, O. Tkachuk, J. Padgurskas, V. Trush, and R. Proskurnyak, "Comparison of Friction Behaviour of Titanium Grade 2 after Non-Contact Boriding in Oxygen-Containing Medium with Gas Nitriding," *Coatings*, vol. 13, no. 2, 2023, doi: 10.3390/coatings13020282.

CRYSTALLOGRAPHIC INSIGHTS INTO THE OXYGEN ORDERING IN Ti-O SYSTEM: CONSEQUENCES ON THE MECHANICAL PROPERTIES

Régis Poulain^{1,2,3}, Fabienne Amann^{1,3}, Stéphanie Delannoy^{1,2}, Ivan Guillot³, Raphaëlle Guillou⁴, Sylvie Lartigue-Korinek³, Zachary Kloenne⁵, Dominique Thiaudière⁶, Jean-Luc Béchade⁷, Emmanuel Clouet⁷, Hamish Fraser⁵, Frédéric Prima¹

1 Université PSL, Chimie ParisTech–CNRS, Institut de recherche de Chimie Paris (UMR 8247), 75005 Paris, France

2 Biotech Dental SAS, 305 allées de Craponne, 13300, Salon-de-Provence, France

3 Université Paris Est Créteil, CNRS (UMR 7182), 2 rue H. Dunant, F- 94320 Thiais France

4 Université Paris-Saclay, CEA, Service de Recherches Métallurgiques Appliquées, F-91191, Gif-sur-Yvette, France

5 Ohio State University, Department of Materials Science and Engineering, Columbus, OH 43210 USA

6 Synchrotron SOLEIL, F-91192, Gif-sur-Yvette, France

7 Université Paris-Saclay, CEA, Service de Recherches de Métallurgie Physique, F-91191, Gif-sur-Yvette, France

The hexagonal-close packed titanium α -phase has long been believed to be able to incorporate up to 15wt% of oxygen in solid solution. This view, though, is challenged since the 1970s with the report of ordered compounds at lower oxygen concentrations. More recently, studies have even predicted the existence of a Ti_6O structure arising for contents as low as 0.3wt%. The influence of oxygen on titanium is yet still examined through the prism of atoms in solid solution, particularly when considering their impact on the mechanical properties. Here, we evidence that oxygen ordering phenomena can occur at low oxygen contents and have a real impact on strength and ductility. This work focuses on the microstructural and mechanical study of a series of Ti-xO alloys, with x ranging from 0.15 to 0.8wt%. In all alloys, X-Ray Diffraction and Transmission Electron Microscopy allow to evidence ordered nanoprecipitates with a crystallographic structure close to Ti_6O associated with an oxygen ordering in the hexagonal octahedral sites. The stress-strain curves resulting from this microstructure display a drastically different mechanical behavior in contrast to the literature results for the Ti-O system: a strong hardening is still observed with oxygen addition, but the ductility remains constant between 0.2 and 0.6wt%. The absence of the classically observed ductility drop is here explained by the interaction between the dislocations and the oxygen-ordered precipitates. These results call for a reassessment of the precise role of oxygen in titanium alloys and open up promising perspectives for the development, at lower costs, of oxygen-tolerant titanium alloys, which could be of great interest to biomedical industry since oxygen is fully biocompatible.

Keywords: Oxygen strengthening, ordering, mechanical properties, electron microscopy.

1. Introduction

Titanium alloys are found in mechanically demanding applications, i.e. aerospace and biomedical [1], where materials durability in service is safety-critical. The oxygen addition in titanium results in a large strength increase but also a drastic drop in ductility and associated embrittlement [2–5]. These two antagonistic mechanical properties are balanced by carefully monitoring the oxygen content in commercially pure α -titanium alloys not to exceed 0.4 wt% [3,6]: beyond such a concentration, oxygen appears as a “poison” because of a dramatic drop in ductility. Costly efforts have thus been pursued in the titanium industry to prevent oxygen contamination during the complete processing route for α -titanium alloys. When oxygen is added in titanium, the resulting strengthening is ascribed to the strong interaction of gliding dislocations with isolated oxygen atoms [2,4,7–9]. Our current understanding of the impact of oxygen additions on the mechanical properties of titanium and its alloys therefore uniquely relies on a picture where all oxygen atoms are in solid solution.

However, in the early 1970s, a few scattered studies on order-disorder transitions reported that oxygen had a natural tendency to order itself into interstitial

superlattices when added in high concentration in titanium α -phase [10–14]. More recently, thermodynamic models relying on *ab initio* calculations have foretold the existence of Ti_6O ordered compounds [15,16], with oxygen ordering on the octahedral interstitial sites of the hcp lattice, for compositions as low as 0.3 wt% oxygen at room temperature. These predictions have not been supported, so far, by experimental observations of such compounds for oxygen contents below the Ti_6O stoichiometry. However, a thorough observation of the literature shows that the nearly-universally accepted assumption that oxygen only contributes to solid solution hardening hardly accounts for the great dispersion of mechanical properties obtained in the Ti-O system over nearly 50 years of research [17–21]. At this stage, we can safely say that a piece is missing in our current understanding of oxygen hardening in titanium alloys and a paradigm shift may be necessary to fully grasp the complex effects of oxygen on the mechanical properties of titanium alloys.

In this work, the capacity of oxygen to form ordered compounds in the titanium α -phase is investigated in a series of Ti-xO alloys, with x ranging from 0.15 to 0.8 wt%. The influence of oxygen on the mechanical properties is then studied and discussed.

2. Experimental methods

All Ti-xO alloys analyzed in this study, with x ranging from 0.15 to 0.8 wt%, were received from Timet company. To precisely control their oxygen contents, TiO₂ powder were added to arc-melted pure titanium sponges. The obtained 200 g buttons were then hot-rolled into square-shaped bars, heat-treated at 923 K for 1800 s and water quenched. Pieces of the bars were then cut, cold-rolled down to 0.6 mm plates, recrystallized at 1023 K for 600 s in molten salts baths (Li₂CO₃, Na₂CO₃, K₂CO₃) and water quenched. The gas analyses of the interstitial contents in all alloys revealed a very low nitrogen contamination (<0.007 wt%) and small oxygen concentration deviations compared to the aimed contents (<5%). Samples were cut from the plates, polished with SiC paper and electropolished with a Struers LectroPol-5 apparatus using an electrolyte solution composed of HClO₄ (6%), HCl (4%), 2-butoxyethanol (34%) and methanol. Electron Backscattered Diffraction (EBSD) maps were then obtained using a Leo 1530 SEM operating at 20 kV. Transmission Electron Microscopy (TEM) samples were prepared by cutting 3 mm discs and grinding them down to 100 μ m. A final electrolytical thinning was carried out using a Struers Tenupol twin-jet machine with a solution of butanol (27%), HClO₄ (7%) and methanol at a voltage of 25 V and a temperature of 253 – 263 K. TEM observation were carried out on a JEOL 2100+ microscope working at 200 kV. X-ray diffraction samples were grinded with SiC paper and analyzed using a Panalytical XPert Pro diffractometer with Cu K α radiation at 45 kV, 40 mA and with precession of the sample. The TEM image analyses were performed using the ImageJ software [22]: a contrast threshold were applied, followed by a ‘particle analysis’. Dynamical diffraction patterns were computed using the software CRYSTAL developed in our laboratory by D.Gratias and M. Quiquandon based on the quantum mechanical formulation of dynamical elastic diffraction of fast electrons [23,24]. The Scanning-TEM (STEM) images were taken in a 1%-strained sample using a FEG-equipped Tecnai F20 operating at 200 kV. Flat dog-bone specimens with a 20 mm gauge length were cut along the rolling direction for tensile tests. Two reproducible tests were performed on a 10 kN INSTRON 5966 electro-mechanical machine using a 10 mm gauge length extensometer and a strain-rate of 10^{-3} s⁻¹.

3. Microstructure of the Ti-xO alloys

3.1. Evidencing the presence of nanoprecipitates

The Fig 1 depicts the multi-scale analysis of the microstructure in the Ti-0.4%O alloy that is

representative of the microstructure observed in the entire alloy family.

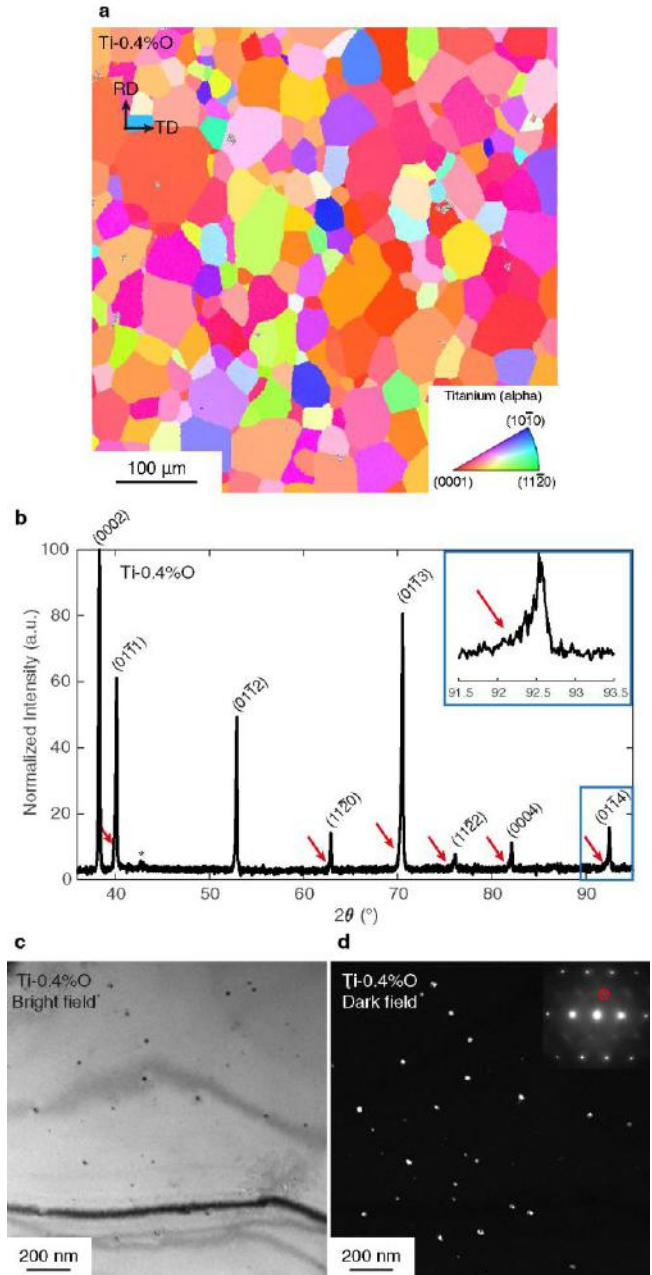


Figure 1. Microstructure analysis of the Ti-0.4%O alloy. EBSD Inverse Pole Figure (IPF) orientation map along normal direction (a). The triangle representing the orientation color code for the α -phase is plotted on the right side. RD: Rolling Direction. TD: Transverse Direction. XRD diffractogram (b) with red arrows highlighting the systematic shoulders on the left of each peak. The inset is a magnification of the (01 $\bar{1}$ 4) reflection. The peak marked by the symbol * is induced by a sample holder artifact. Bright-field (c) and dark-field (d) TEM images taken in [10 $\bar{1}$ 2] zone axis, which SADP is shown in inset. The reflection used to take the dark-field picture is highlighted by a red circle. From [25,26].

From the EBSD map, Fig 1a, equiaxed α -grains are noticed, showing a strong (0001) texture that is often observed in recrystallized α -titanium alloys [27]. The grain size, determined by the mean circle diameter of the detected grains with a misorientation threshold of 5° , is approximately $35\ \mu\text{m}$. The X-ray diffraction (XRD) analysis, Fig 1b, presents a set of peaks characteristic of the α -phase with no additional peak. However, a systematic shoulder, highlighted by the red arrows in Fig 1b, can be evidenced on the side of most α -peaks toward low diffraction angles. One possible interpretation of the presence of such shoulders is that they are the signature of another structure, very similar to the α -phase but with slightly different lattice parameters. To support this hypothesis, finer observations using bright-field and dark-field conditions in TEM were performed and are displayed in Fig 1c and 1d. The micrographs reveal nanoprecipitates whose size is in the 15-30 nm range and are too small to be observed in a SEM. The Selected Area Diffraction Pattern (SADP) associated with these precipitates, in inset in Fig 1d, reveal superlattice reflections. These additional spots are only visible in some particular zone axes, such as $[10\bar{1}2]$, but not in the most commonly studied ones, such as $[11\bar{2}0]$ or $[0001]$.

3.2. Determination of the crystallographic structure

To further investigate the crystallographic structure of the nanoprecipitates, a set of SADP in different zone axes is taken and analyzed. The diffraction patterns including superlattice reflections are gathered in Fig 2 and compared to the structure composed of titanium and oxygen that are referenced in the literature. Among the possible candidates, our experimental patterns particularly match the Ti_6O crystal structure [12–14], represented in Fig 2d along the $[01\bar{1}0]_{\text{Ti}_6\text{O}}$ direction. To confirm this match, the corresponding diffraction patterns in the Ti_6O structure are simulated and depicted in Fig 2d. To account for all observed superlattice spots, the simulation assumes that the structure is sub-stoichiometric to break a mirror symmetry existing in the perfect and stoichiometric Ti_6O structure. As a result, a perfect fit between the experimental and simulated patterns is observed. The fact that some additional spots of the $[2\bar{1}\bar{1}3]_{\text{Ti}_6\text{O}}$ zone axis are not experimentally observed can be explained by their relatively lower intensity.

The determined Ti_6O -type structure is thus a trigonal structure (space group $P31c$) arising from oxygen ordering in every second layer along the $[0001]_\alpha$ axis.

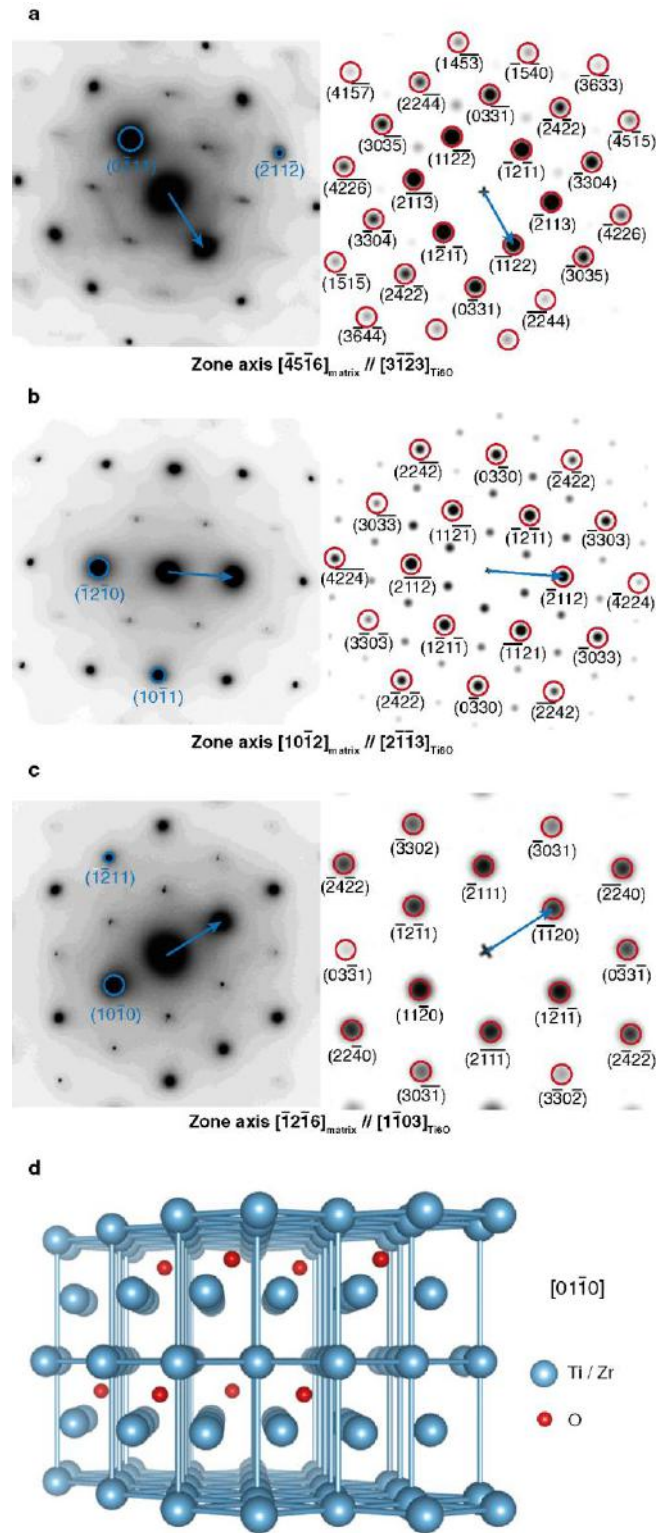


Figure 2. Structure determination of the nanoprecipitates. Experimental TEM SADP with inverted contrast and corresponding simulated diffraction patterns of the Ti_6O structure in the zone axes where superlattice spots are observed: $[45\bar{1}6]$ (a), $[10\bar{1}2]$ (b) and $[\bar{1}2\bar{1}6]$ (c). The blue arrows are visual guides to compare experimental and simulated patterns. The red circles on the simulated patterns highlight the spots that are visible in the respective experimental image. Atomic representation of the Ti_6O crystal structure along $[01\bar{1}1]$ direction (d) obtained using VESTA three-dimensional visualization program [28]. From [25].

The Burgers Orientation Relationship (BOR) inferred from the different SADPs is the following: $[0002]_{\alpha} // [0002]_{\text{Ti}_6\text{O}}$ and $(1\bar{1}00)_{\alpha} // (1\bar{2}10)_{\text{Ti}_6\text{O}}$, which corresponds to the theoretical description available in the literature [12,29]. The shoulders evidenced in XRD, Fig 1b, are therefore perfectly explained by the strong similarity between the α -phase and the Ti_6O structure and by their very close lattice parameters, whereas the absence of additional peak characteristic of the Ti_6O structure results from their extremely low relative intensity, around 1%.

3.3. Observation of precipitates in all Ti-xO alloys

TEM observations are further carried out to assess the presence of the ordered nanoprecipitates in the entire Ti-xO alloy family. It is first worth noting that no precipitate has been observed in pure titanium (0.05 wt%O), thus ruling out the hypothesis of a precipitate's formation during TEM sample electropolishing. The TEM images taken in the Ti-xO alloys, and gathered in Fig 3, all display the same nanoprecipitates as in the Ti-0.4%O alloy. The precipitates size does not significantly evolve with oxygen content and remains stable around 20 nm.

It should be pointed out that such ordered precipitate has never been evidenced in Ti-O alloys in the composition range 0.15 – 0.8 wt%O. This point can be

explained by the fact that the SADP displaying the superlattice spots, $[\bar{4}5\bar{1}6]$, $[10\bar{1}2]$ and $[11\bar{2}6]$, are high indices zone axes and therefore are not particularly studied. The observation of ordered precipitates in our Ti-xO alloys is, though, in complete agreement with a published phase diagram deduced from *ab initio* calculations, where ordering of oxygen at low temperature was predicted [16].

4. Mechanical properties and strengthening mechanisms

4.1. Tensile properties of the Ti_xO alloys

The observation of the Ti_6O -type precipitates in all Ti-xO alloys raise the question of their influence on the mechanical properties. The Fig 4a shows the engineering stress-strain curves of our alloys. Below 0.6 wt%O, a linear increase in Yield Strength (YS) is observed with oxygen, from 400 to 700 MPa. Surprisingly, this evolution is coupled with a maintaining of the elongation-to-fracture around 30%. This behavior strongly contrasts with previous works on Ti-O alloys [2,4], where the strength increase is combined with a sharp decrease in elongation-to-failure. A slope-break is yet observed at 0.8 wt%O, with a drastic increase in YS and a severe drop in elongation-to-fracture, suggesting a turning point in terms of oxygen content regarding the mechanical properties.

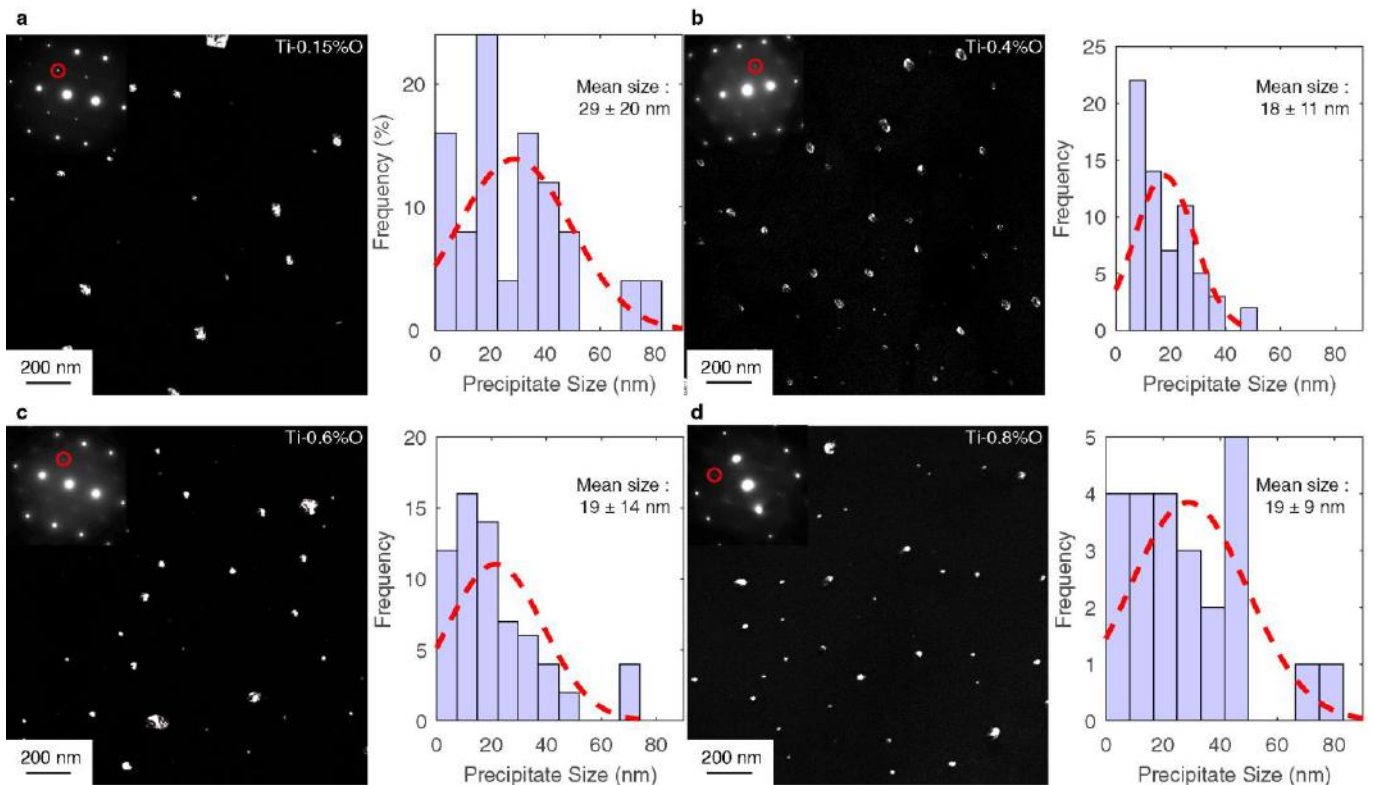


Figure 3. TEM observations in dark-field conditions of the Ti-xO alloys with $x = 0.15$ (a), 0.4 (b), 0.6 (c) and 0.8 (d). The insets indicate the corresponding zone axis and show the SADP, and the reflections used to record the dark-field images (red circles). The respective distribution function of the precipitates size is represented for each alloy. From [25]

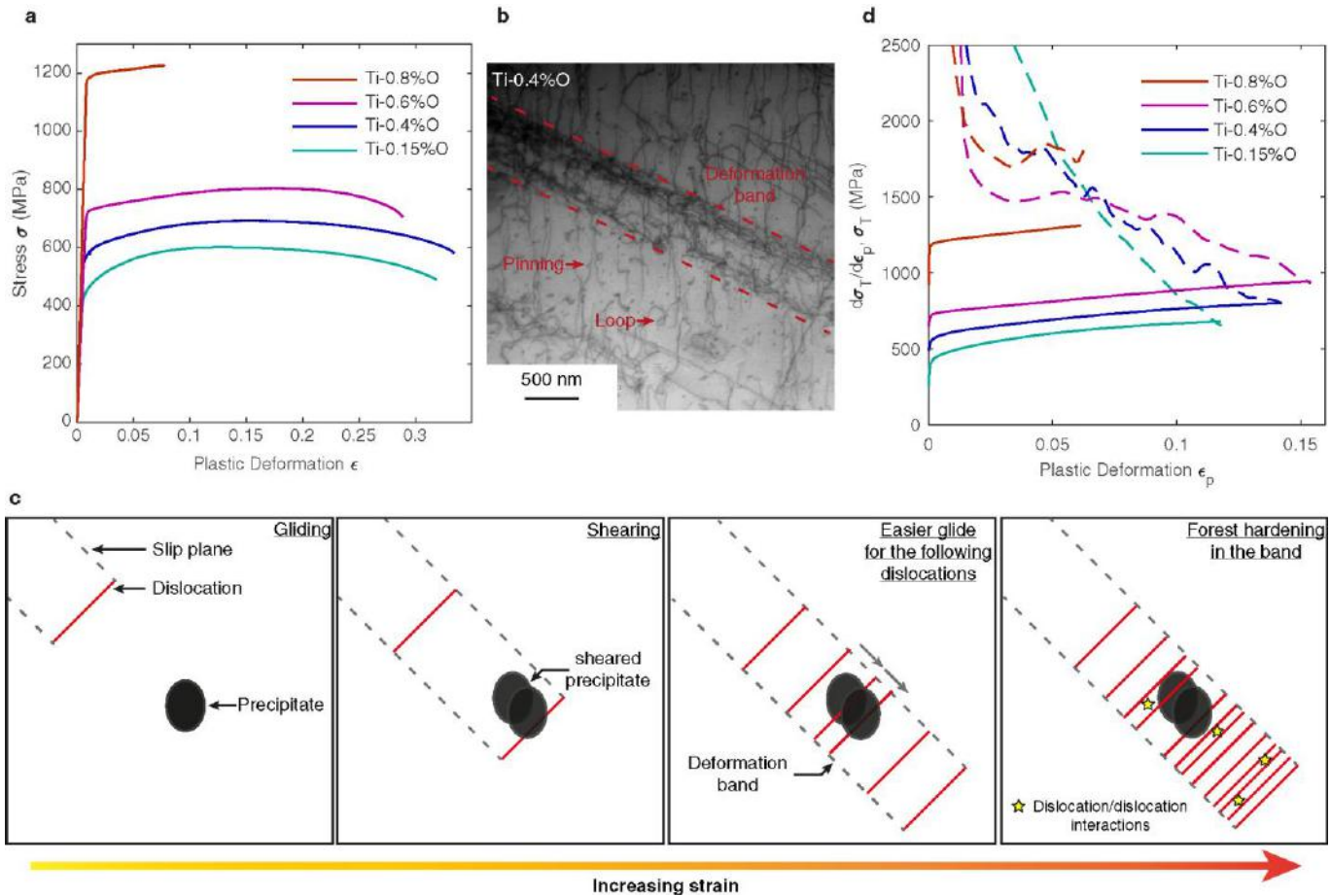


Figure 4. Mechanical properties of the Ti-xO alloys at room temperature. Engineering stress-strain curves (a) and true-stress – true plastic strain curves with corresponding work-hardening rates (dotted lines) (c) of the Ti-xO alloys. STEM image taken in Ti-0.4%O alloy deformed at 1% plastic strain in ABF conditions and in [4156] zone axis (b). Schematic diagram illustrating the dislocation/precipitates interactions leading to the alloy strengthening (d). From [26].

Interestingly, the maintaining of the elongation-to-failure with oxygen addition was already reported in a previous work [17], where the X-ray diffractograms display the same type of systematic shoulders as in our work. This detail suggests that Ti_6O -type precipitates might be present in these alloys as well and play a key role in the conservation of the elongation-to fracture.

4.2. Investigation on the hardening mechanisms

To investigate the impact of the nanoprecipitates on the dislocation network, STEM observations are carried out in a 1%-strained Ti-0.4%O sample. The micrography, depicted in Fig 4b, reveals the presence of numerous pinning points, indicating strong dislocations/precipitates interactions. These probably leads to a strong strengthening of the alloy, that is different from the often put forward solid solution hardening. Besides, the presence of slip bands, in which dislocations are confined, suggests that at this scale, the plastic deformation localizes.

The mechanism leading to such localization can reasonably be explained by the precipitates/dislocations interactions, as illustrated in Fig 4c. Since the

nanoprecipitates have a small lattice mismatch with the matrix and a nanometric size, they are easily sheared by a first dislocation, opening a way for following dislocations gliding in the same direction [5]. The strong precipitates/dislocations interactions probably lead to profuse cross-slips, as supported by the observation of multiple loops and debris [4,8,9]. The result of the confinement of the dislocations within deformation bands coupled with an intense cross-slip activity is a probable forest hardening due to the interactions of dislocations with each other.

This mechanism is macroscopically studied in Fig 4d, displaying the Work-Hardening (WH) rate of our alloys according to the true plastic strain. In the Ti-0.15%O alloys, the WH rate is high at low deformation, then quickly decreases. At 0.4 wt%O, the WH rate decreases at lower deformation but stabilizes and decreases more slowly at higher deformation. This trend with oxygen addition is confirmed for the Ti-0.6%O and the Ti-0.8%O alloys, for which a nearly perfect elastoplastic transition is observed. The increasing strain hardening ability with oxygen content is here attributed to

the forest hardening described in Fig 4c. Besides, the combine increase in WH with oxygen content and the high value of WH most probably explain the possibility for our alloys to reach large deformations before necking and a high ductility.

5. Conclusion

This work allowed evidencing a novel type of precipitates, that arise from oxygen ordering, in a wide range of α Ti-xO alloys. These precipitates exhibit a crystalline structure close to Ti₆O, very similar to the α phase, which may explain the difficulty to observe them. The mechanical properties of these alloys were investigated and showed a conservation of the elongation-to-fracture up to 0.6 wt%O. The maintaining of the ductility may here be explained by the interactions between the nanoprecipitates and the dislocation. The combination of an intense cross-slip activity on one hand and of a forest hardening induced by the confinement of dislocations in deformation bands on the other hand leads to large work-hardening rates that enable a substantial homogeneous deformation and a large ductility.

The combination of both strength and ductility reached for the Ti-0.6%O alloy, 800 MPa and 29% respectively, opens very promising outlooks for the development of oxygen-enriched α titanium alloys in which the classically observed ductility loss is prevented.

6. Acknowledgements

Y. Millet from the Timet company is gratefully acknowledged for providing the alloys studied in this work. We thank D. Gratias and M. Quiquandon for their help with the TEM diffraction simulation. The company Biotech Dental is acknowledged for its financial support on R.P. grant (Industrial CIFRE doctoral fellowship). The funding of the TiTol Project (ANR-19-CE08-0032) was provided by the French National Research Agency.

7. References

- [1] D. Banerjee, J.C. Williams, *Acta Mater.* 61 (2013) 844–879.
- [2] H. Conrad, *Prog. Mater. Sci.* 26 (1981) 123–403.
- [3] G. Lutjering, J.C. Williams, *Titanium*, 2nd editio, Springer-Verlag Berlin Heidelberg, Berlin, Germany, 2007.
- [4] Q. Yu, L. Qi, T. Tsuru, R. Traylor, D. Rugg, J.W. Morris, M. Asta, D.C. Chrzan, A.M. Minor, *Science*. 347 (2015) 635–639.
- [5] Y. Chong, M. Poschmann, R. Zhang, S. Zhao, M.S. Hooshmand, E. Rothchild, D.L. Olmsted, J.W. Morris, D.C. Chrzan, M. Asta, A.M. Minor, *Sci. Adv.* 6 (2020) 1–11.
- [6] R.O. Ritchie, *Nat. Mater.* 10 (2011) 817–822.
- [7] S. Naka, A. Lasalmonie, P. Costa, L.P. Kubin, *Philos. Mag. A Phys. Condens. Matter, Struct. Defects Mech. Prop.* 57 (1988) 717–740.
- [8] B. Barkia, J.P. Couzinié, S. Lartigue-Korinek, I. Guillot, V. Doquet, *Mater. Sci. Eng. A* 703 (2017) 331–339.
- [9] N. Chaari, D. Rodney, E. Clouet, *Scr. Mater.* 162 (2019) 200–203.
- [10] M. Hirabayashi, S. Yamaguchi, H. Asano, K. Hiraga, in: H. Warlimont (Ed.), *Order-Disorder Transform. Alloy.*, Springer-Verlag Berlin Heidelberg, Berlin, Heidelberg, Germany, 1974, pp. 266–302.
- [11] S. Banerjee, P. Mukhopadhyay, in: E. Science (Ed.), *Phase Transform. Examples from Titan. Zircon. Alloy.*, New York City, USA, 2007, pp. 764–769.
- [12] S. Yamaguchi, *J. Phys. Soc. Japan* 21 (1966) 2096.
- [13] S. Yamaguchi, *J. Phys. Soc. Japan* 27 (1969) 155–163.
- [14] S. Yamaguchi, K. Hiraga, M. Hirabayashi, *J. Phys. Soc. Japan* 28 (1970) 1014–1023.
- [15] B.P. Burton, A. Van De Walle, *Calphad Comput. Coupling Phase Diagrams Thermochem.* 39 (2012) 97–103.
- [16] N.S.H. Gunda, B. Puchala, A. Van Der Ven, *Phys. Rev. Mater.* 2 (2018) 33604.
- [17] B. Sun, S. Li, H. Imai, T. Mimoto, J. Umeda, K. Kondoh, *Mater. Sci. Eng. A* 563 (2013) 95–100.
- [18] D.J. Simbi, J.C. Scully, *Mater. Lett.* 26 (1996) 35–39.
- [19] B. Chen, J. Shen, X. Ye, J. Umeda, K. Kondoh, *J. Mater. Res.* 32 (2017) 3769–3776.
- [20] Y. Liu, H. Tang, Q. Huang, D. Zhao, J. He, Y. Cao, M. Song, B. Liu, S. Ouyang, *Trans. Nonferrous Met. Soc. China* 30 (2020) 2449–2458.
- [21] S.D. Luo, T. Song, S.L. Lu, B. Liu, J. Tian, M. Qian, *J. Alloys Compd.* 836 (2020).
- [22] C.A. Schneider, W.S. Rasband, K.W. Eliceiri, *Nat. Methods* 9 (2012) 671–675.
- [23] D. Gratias, R. Portier, (2017).
- [24] M. Quiquandon, J.T. Beauchesne, D. Gratias, *Philos. Mag.* 88 (2008) 1941–1948.
- [25] R. Poulain, S. Delannoy, I. Guillot, F. Amann, S. Lartigue-korinek, D. Thiaudière, J. Béchade, E. Clouet, F. Prima, *Mater. Res. Lett.* 10 (2022) 481–487.
- [26] F. Amann, R. Poulain, S. Delannoy, J.P. Couzinié, E. Clouet, I. Guillot, F. Prima, *Mater. Sci. Eng. A* 867 (2023).
- [27] N. Bozzolo, N. Dewobroto, T. Grosdidier, F. Wagner, *Mater. Sci. Eng. A* 397 (2005) 346–355.
- [28] K. Momma, F. Izumi, *J. Appl. Crystallogr.* 44 (2011) 1272–1276.
- [29] S. Banerjee, P. Makhopadhyay, *Phase Transformations : Examples from Titanium and Zirconium Alloys*, Vol.12, Elsevier Science Ltd, 2007.

EFFECT OF OXYGEN ON THE MICROSTRUCTURE AND MECHANICAL PROPERTIES OF $\alpha+\beta$ -TYPE Ti-5Nb ALLOYS FOR BIOMEDICAL APPLICATIONS

Kyosuke Ueda¹, Yusuke Hirose¹, Takayuki Narushima¹

1 Department of Materials Processing, Graduate School of Engineering, Tohoku University, 6-6-02, Aza-Aoba, Aramaki, Aoba-ku, Sendai, 980-8579, Japan.

Oxygen is the primary impurity in titanium (Ti); thus, utilizing oxygen as an alloying element may effectively lower the production costs of Ti alloys. In this study, the microstructure and mechanical properties of the Ti-Nb-O alloy system were studied to develop low-cost $\alpha+\beta$ -type Ti alloy. Ti-5Nb-(0.2, 0.5, 0.7)O (mass%) alloys were prepared by arc melting, and the ingots were hot-forged and heat-treated at 973–1323 K for 3.6 ks in an argon (Ar) atmosphere. The alloys consisted of α and α' phases under the heat-treatment condition of the α -phase fraction (f_α) of 0.3, independent of the oxygen content. The elastic modulus of the Ti-5Nb- x O alloys was approximately 95 GPa, independent of the oxygen content, which is lower than that of the Ti-6Al-4V (Gr. 5) alloy. The indentation hardness of the α phase is higher than that of the α' phase because of the distribution of oxygen in the α phase. The critical cold rolling reduction (CCR) of the Ti-5Nb- x O alloys decreased with increasing the oxygen content. The CCR of Ti-5Nb-(0.2 and 0.5)O alloys was higher than that of Ti-6Al-4V alloy. Thus, in conclusion, the Ti-5Nb-0.5O alloy is a promising low-cost $\alpha+\beta$ -type Ti alloy for biomedical applications. It has a low elastic modulus and good tensile properties, with toughness and cold workability comparable to those of Ti-6Al-4V alloy.

Keywords: $\alpha+\beta$ -type Ti alloys, oxygen, approach curve, α fraction, tensile properties, Charpy impact strength, cold workability.

1. Introduction

Titanium (Ti) and its alloys are used in aerospace components, chemical plants, and biomedical devices owing to their high specific strengths, excellent corrosion resistances, and good biocompatibilities [1–3]. In particular, $\alpha+\beta$ -type Ti alloys exhibit an excellent balance between strength and ductility. Their mechanical properties can be controlled by changing the fraction, shape, and grain size of the α -phase through thermomechanical processing [4,5].

However, Ti and its alloys have a high production cost, which limits their application [6]. Therefore, alloying with ubiquitous elements has been suggested as an effective method for reducing costs. Oxygen is the primary impurity in Ti; thus, utilizing oxygen as an alloying element may effectively lower the production costs of Ti alloys. In our previous study, we focused on oxygen, vanadium (V), and niobium (Nb) as alloying elements to develop $\alpha+\beta$ -type Ti alloy for biomedical applications [7–10]. Nb is known to have less cytotoxicity and is already employed as an alloying element in biomedical β -type Ti alloys. The Ti-5Nb-(0.5, 0.75)O (mass%) alloys fabricated previously exhibited excellent tensile properties, high corrosion resistance, and low cytotoxicity [10]. As oxygen decreases toughness and cold workability, its content in the alloy must be optimized. Therefore, in this study, the effects of oxygen and thermomechanical treatments on the microstructure, mechanical properties, and cold workability of the $\alpha+\beta$ -type Ti-5Nb alloys were investigated.

2. Materials and methods

2.1. Fabrication and heat treatment of specimens

Commercially pure (CP) Ti plates (JIS Grade 2; oxygen content: 0.1038 mass% (1038 mass ppm)) and TiO₂ powder (99.5%) were melted in a non-consumable electrode argon (Ar) arc-melting furnace to fabricate a master Ti-1.5mass%O binary alloy. Next, the master alloy, CP Ti plates, and Nb plates (99.9%) were arc-melted to fabricate Ti-5Nb-(0.2–0.7)O (mass%) alloy ingots. The oxygen and Nb contents of the alloys were measured using inert gas fusion infrared absorption and inductively coupled plasma-mass spectrometry (ICP-MS), respectively. The chemical compositions of the alloys after forging are listed in Table 1. Hereinafter, the alloys are referred to as x O alloys based on their oxygen content.

After melting, the ingots were forged in β -region at 1373 K to form bars with diameters of 16 mm, followed by air cooling to room temperature. Subsequently, the alloys were forged in the $\alpha+\beta$ region at 1073 K to form bars with diameters of 8 mm, followed by air cooling to room temperature. During the forging process, the alloys were reheated to prevent a decrease in temperature. The forged alloy bars were cut into sections (diameter: 8 mm, length: 40 mm), and the oxide scale on the specimen surface was removed by machining. A Ti-6Al-4V alloy (Gr. 5, oxygen content: 0.14 mass%) forged bar was used for comparison.

After forging, heat treatments were performed under Ar flow at 973–1323 K for 3.6 ks, followed by quenching in ice water. A schematic of the

thermomechanical process used in this study is shown in Figure 1.

Table 1: Chemical composition of Ti-5Nb-xO alloys and β -transus (T_β) estimated from approach curve.

Alloy	Chemical composition (mass%)			β -transus, T_β / K
	Ti	Nb	O	
0.2O	Bal.	4.75	0.18	1151
0.5O	Bal.	4.87	0.49	1205
0.7O	Bal.	5.12	0.72	1274

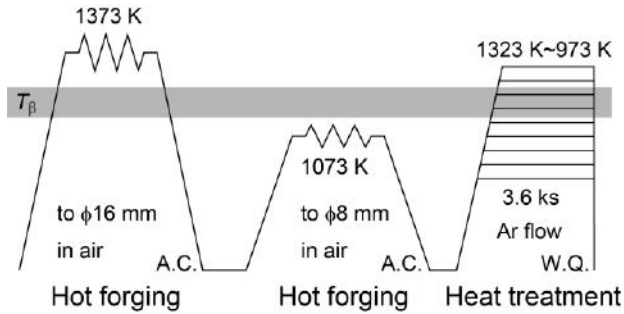


Figure 1. Schematics of thermomechanical treatment applied in this study.

2.2. Analysis of microstructures of specimens

The microstructures of the alloys were observed using scanning electron microscopy (SEM) in backscattered electron (BSE) mode. The volume fraction of the equiaxed α -phase (f_α) was calculated from five SEM images (magnification: $\times 2000$) using an image analysis software (ImageJ). The value of f_α was calculated as the area fraction of the equiaxed α -phase observed in the SEM images, as defined by Eq. (1) [7,8,10].

$$f_\alpha = S_\alpha / S_{\text{total}}, \quad (1)$$

where S_α is the area of the equiaxed α -phase in the SEM image; and S_{total} is the total image area. The constituent phases of the heat-treated alloys were identified by X-ray diffraction (XRD). The oxygen and Nb contents of the α - and β -phases (α' -phase) were determined by field-emission electron probe microanalysis (FE-EPMA) using CP Ti and Ti-(5, 10, 15, 20)Nb-(0.2, 0.5, 0.7, 1.0)O (mass%) alloys as reference materials. The reference materials were heat-treated above the β -transus (T_β) to obtain a single phase. Measurements were performed at

10 positions for each phase, and the average values and standard deviations were calculated.

2.3. Evaluation of mechanical properties of specimens

As the grain size of each phase was approximately 5–10 μm , the hardness of each grain was measured by a nanoindentation hardness tester with a load of 5 mN (0.5 gf). After indentation testing, the indentation trace was observed using SEM, and the indentation traces on the α and β grains were decided. Ten values for each phase were calculated to obtain the average values and standard deviations.

Uniaxial tensile tests were conducted at room temperature using a universal material testing instrument. The tensile specimens were machined to gauge diameters and lengths of 3 mm and 10 mm, respectively. The strain rate was set to $5.0 \times 10^{-4} \text{ s}^{-1}$, and the tensile strength, 0.2% proof stress, and total elongation were measured. The elastic moduli of the specimens were measured using the free resonance vibration method.

Charpy V-notch test (CVN) was performed at room temperature using specimens with dimensions of 55 mm \times 10 mm \times 2.5 mm, and a notch depth of 2 mm [11]. Tensile tests, CVN tests, and elastic modulus measurements were performed on three specimens for each heat-treatment condition, and the average values and standard deviations were calculated.

The cold workability of the alloys was evaluated using cold-rolling testing. Specimens with dimensions of 55 mm \times 10 mm \times 2 mm were polished and subjected to cold rolling. The roll gap was decreased by 0.1 mm each and the thickness of the specimen after formation of cracks was measured to evaluate the critical cold rolling reduction (CCR).

3. Results and discussion

3.1. Microstructure of the alloys

Figure 2 shows the microstructures of the 0.2O, 0.5O, and 0.7O alloys after heat treatment at various temperatures for 3.6 ks. Equiaxed α -phase grains were observed, indicated by the gray-colored regions, in the alloys. Acicular grains were detected after heat treatment at 1173, 1223, and 1323 K for the 0.2O, 0.5O, and 0.7O alloys, respectively. These were considered as prior β grains. The volume fraction of the equiaxed α -phase (f_α) in each alloy was calculated from the SEM images using Eq. (1). The f_α values are plotted in Figure 3 as functions of the heat-treatment temperature (approach curve). In cases where no equiaxed α -phase was observed in the

alloy, as shown in Figures 2 (a), (d), and (g), f_{α} was taken to be zero. Here, the approach curves were obtained as smooth curves using all values of f_{α} , except $f_{\alpha} = 0$ for each alloy. Evidently, the values of f_{α} decreased as the heat-treatment temperature increased. The gradients of these curves decreased with increasing oxygen content, and those of the 0.5O and 0.7O alloys were smaller than those of the Ti-6Al-4V alloy. This indicates that the heat treatment windows of 0.5O and 0.7O alloys are wider than those of the Ti-6Al-4V alloy, thus implying good heat treatability. The β -transus (T_{β}) of the alloys were estimated by extrapolating the approach curves to $f_{\alpha} = 0$, and the values are listed in Table 1.

As is well known, the mechanical property of $\alpha+\beta$ type Ti alloy is affected by the α/β phase ratio. Herein, the Ti-6Al-4V alloy was solution-treated at 1223 K; at this temperature, the f_{α} value was approximately 0.3. Therefore, the heat treatment conditions for the 0.2O, 0.5O, and 0.7O alloys were fixed to achieve an f_{α} of 0.3. The heat-treatment temperatures to obtain the f_{α} value of approximately 0.3 are at 1123, 1173, 1223, and 1223 K for 0.2O, 0.5O, 0.7O, and Ti-6Al-4V alloys, respectively.

The XRD patterns of the alloys with f_{α} of 0.3 are shown in Figure 4. Peaks derived from the hexagonal close-packed (HCP) were observed. Here, the HCP corresponded to the α and α' phases, thus implying that the prior β observed from the SEM images in Figures 2 (a), (d), and (g) was α' phase.

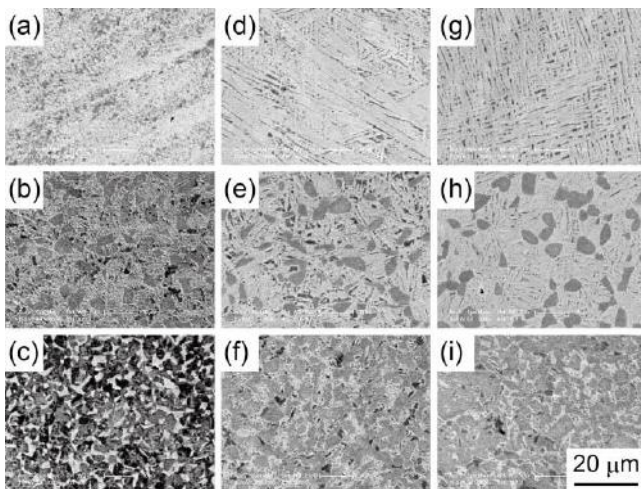


Figure 2. SEM/BSE images of (a)–(c) 0.2O, (d)–(f) 0.5O, and (g)–(i) 0.7O alloys after heat treatment at (a),(e) 1173 K, (b),(f) 1123 K, (c),(i) 1073 K, (d),(h) 1223 K, and (g) 1323 K for 3.6 ks.

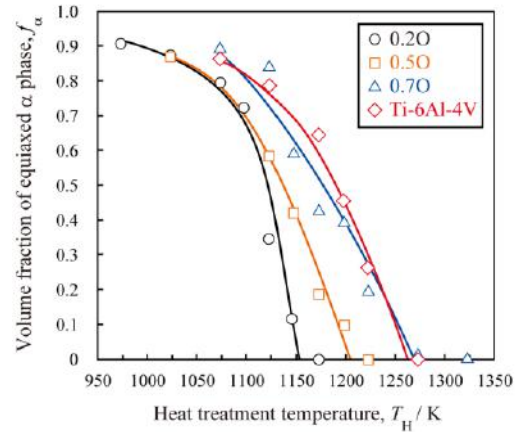


Figure 3. Volume fractions of equiaxed α phase (f_{α}) of 0.2O, 0.5O, 0.7O, and Ti-6Al-4V (Gr. 5) alloys as a function of heat treatment temperature.

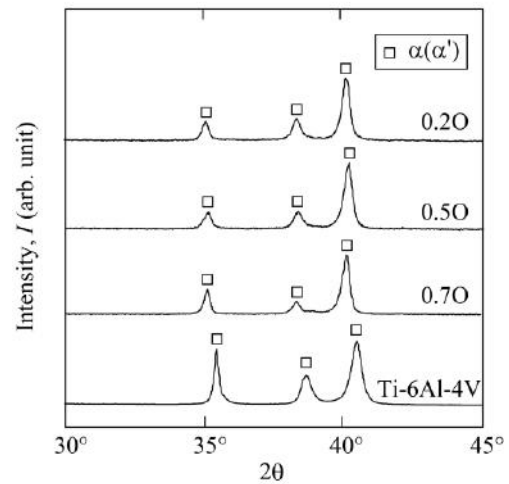


Figure 4. XRD patterns of the 0.2O, 0.5O, 0.7O, and Ti-6Al-4V alloys after heat treatment at 1123, 1173, 1223, and 1223 K, respectively.

3.2. Composition of equiaxed α - and α' - phases after heat treatment of the alloys

The oxygen contents of the equiaxed α and α' (prior β) phase grains of the alloys with f_{α} value of 0.3 as a function of the averaged oxygen content in the alloy are shown in Figure 5. The dotted line in the figure represents the equivalent line between the oxygen content of the alloy and that of each grain. Evidently, the oxygen content in the α phase was higher than that in the α' phase, thus indicating oxygen distribution in the α phase. The oxygen distribution coefficient, k_O , was calculated using Eq. (2), and the oxygen contents in the α ($C_{O,\alpha}$) and α' phases ($C_{O,\alpha'}$), as follows.

$$k_O = C_{O,\alpha} / C_{O,\alpha'} \quad (2)$$

The k_O value of each alloy was approximately 2.1, irrespective of the oxygen content in the alloy.

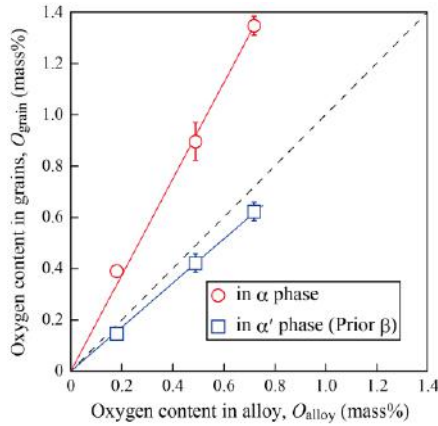


Figure 5. Relationship between averaged oxygen content in the alloy and in α - and α' -phase (prior β) grains.

3.3. Mechanical properties of the alloys

3.3.1. Indentation hardness of α and α' grains

Figure 6 shows the indentation hardness of the equiaxed α and α' grains at the 0.2O, 0.5O, 0.7O, and Ti-6Al-4V alloys analyzed using a nanoindenter. It revealed that the indentation hardness increased with the oxygen content in the alloy. In addition, the indentation hardness of the α grains was higher than that of the α' grains in the Ti-5Nb-xO alloys. These results are good agreement with the oxygen content in each grain (Figure 5). This indicates that the indentation hardness of the alloy was dominated by the oxygen content of the grains. However, for the Ti-6Al-4V alloy, the indentation hardness of the α grains was lower than that of the α' grains. Dong et al. [12] measured the indentation hardness and density of dislocation of each grain of Ti-6Al-4V alloy and reported that the indentation hardness of α' martensite (α' grain) was higher than that of the equiaxed α (α grain) because of the higher density of dislocations in the α' martensite.

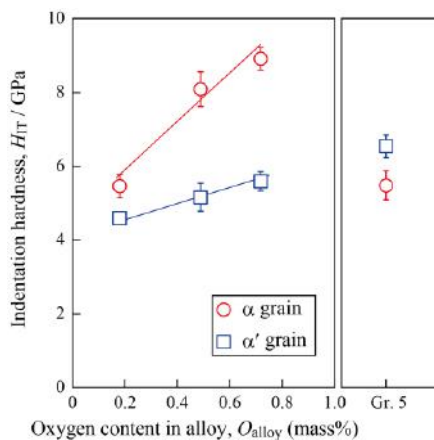


Figure 6. Relationship between oxygen content in the alloy and indentation hardness of α and α' grains. The results of the Ti-6Al-4V alloy are also plotted.

3.3.2. Tensile properties

Figure 7 shows a comparison of the ultimate tensile strength (σ_{UTS}) and total elongation (L) of Ti-5Nb-xO and Ti-6Al-4V alloys [13–17]. For the Ti-5Nb-xO alloys, the ultimate tensile strength increased with increasing the oxygen content in the alloy because of the solid solution strengthening by oxygen, whereas the total elongation decreased with increasing the oxygen content. Compared with the Ti-6Al-4V alloy, the 0.5O and 0.7O alloys exhibited comparable ultimate tensile strengths and superior total elongation.

The elastic moduli of the Ti-5Nb-xO and Ti-6Al-4V alloys with an f_{α} of 0.3 are listed in Table 2. Evidently, the elastic moduli of the Ti-5Nb-xO alloys were approximately 95 GPa, independent of the oxygen content, which is lower than that of the Ti-6Al-4V alloy (107 GPa). For an alloy to be suitable for use in bone substitute devices, such as the stems of artificial hip joints and bone plates, it must exhibit an elastic modulus similar to that of bone to help prevent stress shielding of the bone [18]. Thus, Ti-5Nb-xO alloys are more suitable than the Ti-6Al-4V alloy.

3.3.3. Toughness

The Charpy impact strengths of the Ti-5Nb-xO alloys and Ti-6Al-4V alloy are listed in Table 2. For the Ti-5Nb-xO alloys, the Charpy impact strength decreased with increasing the oxygen content, and for the 0.7O alloy, the value was below the lower limit of measurement. Takahashi and Sato [19] reported that the Charpy impact strength of Ti alloys decreases with increasing oxygen content. Although the Charpy impact strength decreased with the addition of oxygen, the Charpy impact strength of the 0.5O alloy was comparable to that of the Ti-6Al-4V alloy.

3.3.4. Cold workability

The cold workability of the alloys was evaluated using cold-rolling testing. Critical cold rolling reduction (CCR) is defined as the occurrence of several cracks at the edge of a specimen after cold-rolling testing. The CCR values of the Ti-5Nb-xO alloys and Ti-6Al-4V alloy are listed in Table 2. In the case of the Ti-5Nb-xO alloys, although CCR decreased with increasing oxygen content, the value of the 0.5O alloy was higher than that of the Ti-6Al-4V alloy.

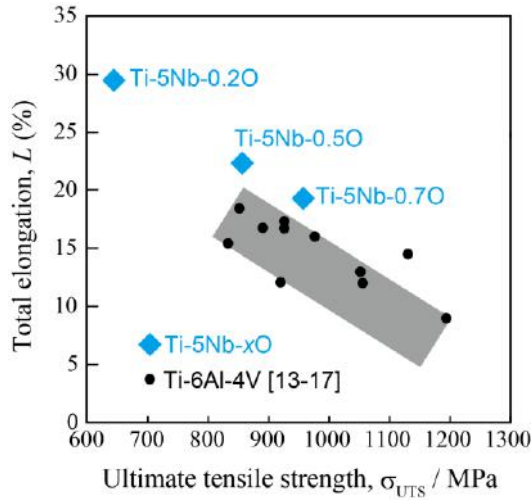


Figure 7. Comparison of ultimate tensile strength and total elongation of Ti-5Nb-xO alloys and Ti-6Al-4V (Gr. 5) alloy [13–17].

Table 2: Elastic moduli (E), Charpy impact strength (E_c), and critical cold rolling reduction (CCR) of Ti-5Nb-xO and Ti-6Al-4V (Gr. 5) alloys with f_α of 0.3.

Alloy	Elastic moduli, E / GPa	Charpy impact strength, E_c / J·cm ⁻²	Critical cold rolling reduction, CCR (%)
0.2O	95.1 ± 0.3	58.1 ± 16.0	70.0
0.5O	95.2 ± 1.4	20.5 ± 0.3	47.7
0.7O	97.1 ± 0.9	*5.1 ± 0.1	26.4
Ti-6Al-4V	106.5 ± 0.1	31.3 ± 1.9	27.0

*: Below the lower limit of measurement

4. Conclusion

The effect of the oxygen content on the microstructure and mechanical properties of the Ti-5Nb alloy was investigated. The β -transus of the Ti-5Nb-(0.2–0.7)O alloys was experimentally decided. The alloys constituted the α and α' phases under the heat-treatment condition of an equiaxed α phase fraction of 0.3. The oxygen distribution coefficient of the alloys was approximately 2.1, independent of the oxygen content. The toughness and cold workability decreased with increasing the oxygen content. Further, the α phase was harder than the α' phase because of the oxygen distribution to the α phase.

Thus, in conclusion, the Ti-5Nb-0.5O alloy is a promising low-cost α + β -type Ti alloy for biomedical

applications. It has a low elastic modulus and good tensile properties, with toughness and cold workability comparable to those of the Ti-6Al-4V alloy.

5. Acknowledgements

The authors thank Prof. Nomura of the Tohoku University for measuring the elastic moduli of the alloys. This study was partially supported by Grants-in-Aid for Science Research (grant numbers 20H02448 and 22K18305) from the Ministry of Education, Culture, Sports, Science and Technology (MEXT), Japan, and The Light Metal Educational Foundation, Inc.

6. References

- Z. Liu, B. He, T. Lyu, Y. Zou, *JOM* 73 (2021) 1804–1818.
- M. Niinomi, T. Hanawa, T. Narushima, *JOM* 57 (2005) 18–24.
- M. Peters, J. Kumpfert, C.H. Ward, C. Leyens, *Advanced Engineering Materials* 5 (2003) 419–427.
- C. Ouchi, *Bulletin of the Japan Institute of Metals* 25 (1986) 672–679.
- S.L. Semiatin, V. Seetharaman, I. Weiss, *JOM* 49 (1997) 33–39.
- F.H. Froes, H. Friedrich, J. Kiese, D. Bergoint, *JOM* 56 (2004) 40–44.
- K. Ueda, T. Kobayashi, T. Narushima, *Journal of the Japan Institute of Metals and Materials* 80 (2015) 60–65.
- M. Omiya, K. Ueda, T. Narushima, *Materials Transactions* 58 (2017) 1250–1256.
- K. Ueda, M. Omiya, Y. Hirose, T. Narushima, *MATEC Web Conferences* 321 (2020) 05003.
- K. Ueda, M. Omiya, K. Kato, H. Kanetaka, T. Narushima, *Materials Transactions* 64 (2023) 138–146.
- JIS Z2242:2018 (2018).
- J. Dong, F. Li, C. Wang, *Materials Science and Engineering: A* 580 (2013) 105–113.
- K. Maeda, S. Suzuki, K. Ueda, T. Kitashima, S.Kr. Bhattacharya, R. Sahara, T. Narushima, *Journal of Alloys and Compounds* 776 (2019) 519–528.
- H. Arabi, M. Ketabchi, *Materials Science and Technology* 35 (2019) 1735–1741.
- P. Ahmadian, M. Morakabati, *Transactions of the Indian Institute of Metals* 73 (2020) 1301–1309.
- M.K. Dunstan, J.D. Paramore, Z.Z. Fang, P. Sun, *Materials Science and Engineering: A*, 764 (2019) 138244.
- Z. Xu, W. Yang, J. Fan, T. Wu, Z. Gao, *Materials* 15 (2022) 3156.
- M. Abdel-Hady Gepreel, M. Niinomi, *Journal of the Mechanical Behavior of Biomedical Materials* 20 (2013) 407–415.
- K. Takahashi, E. Sato, *Tetsu-to-Hagané* 98 (2012) 491–496.

TOWARDS ANTIBACTERIAL IMPLANTS: INFLUENCE OF THE MICROSTRUCTURE ON THE PROPERTIES OF Ti-7Ag ALLOY

Julie Deya^{1,2}, Stéphanie Delannoy^{1,2}, Frédéric Prima¹

1 Université PSL, Chimie ParisTech–CNRS, Institut de recherche de Chimie Paris (UMR 8247), 75005 Paris, France

2 Biotech Dental SAS, 305 allées de Craponne, 13300 Salon-de-Provence, France

The specific composition Ti-7Ag (wt%) was chosen as a model material to illustrate the suitability of Ti-Ag alloys for applications as antibacterial dental implants. Indeed, both a precipitated and a solid-solution microstructural states can be obtained with the same nominal composition through specific thermal treatments. A focus was made on controlling precipitates nucleation since bactericidal activity, corrosion resistance and mechanical properties are known to be improved with a finely distributed precipitation in Ti-Ag systems. Since precipitation can be triggered by pre-strain followed by a thermal treatment, a process was developed to obtain a precipitated state through an adapted recrystallization treatment. Solid solution was then obtained by a controlled dissolution treatment of the precipitated state. The development of this new set of thermomechanical treatments, adapted for industrial purposes, led to optimized microstructures before evaluation of their properties. Mechanical properties assessment highlighted that precipitated state exhibits the best compromise between ultimate strength and elongation, comparable to Ti grade 4 already used to produce dental implants. These findings therefore provide a new insight into Ti-Ag alloys for antibacterial dental implants perspectives.

Keywords: Alpha titanium, silver, precipitation, process, heat treatment, cold rolling, tensile tests

1. Introduction

Due to their good corrosion resistance, mechanical properties and biocompatibility, titanium alloys, such as cp-Ti grade 4 or Ti64, are the materials of choice for biomedical applications, including dental implantology. Although these materials provide a high implant success rate, a significant number of failures are attributed to bacterial infections (e.g. peri-implantitis). To counteract this phenomenon, intrinsic antibacterial alloys are being considered as a promising alternative. One of the possible approaches is to combine titanium with a naturally bactericidal element such as silver. According to the literature, antibacterial properties can then be conferred via two distinct mechanisms: sterilization by direct contact with precipitates [1,2] or action of Ag⁺ ions [3]. However, a review of the literature highlighted that there is currently no clear consensus on the relative effectiveness of each of these mechanisms, for two main reasons: (1) Specimens are often analyzed in homogenized as cast [2,4,5] or sintered state [2,5,6], without further accurate microstructural control, (2) Evaluation of the antibacterial activity (depending on the microstructure), is often performed over a large range of silver nominal contents [4,6], only providing a “dose-related” investigation of the final bactericidal properties [3]. In this work, a unique specific nominal composition, Ti-7Ag (wt%), was investigated since this system is of particular relevance to bring critical information on microstructures. As a fact, the microstructural control is hardly addressed in Ag-containing Ti alloys because of high nucleation barriers regarding the Ti₂Ag intermetallic particles, inducing slow precipitation kinetics. A particular interest was here brought towards the control of both size and distribution of the precipitation since these parameters have presumably a huge impact on final properties. As an example, fine scaled precipitates with a

homogeneous distribution tend to have higher bactericidal activities [2,5]. Besides, precipitation monitoring is also major concern for corrosion resistance and mechanical properties, which are part of the specification for a dental implant. Corrosion resistance of Ti-Ag is higher than pure titanium, but only to the extent that silver content remains low and the precipitates fine scaled [5,7], and coarse precipitation on grains boundary can lead to a detrimental loss of ductility [8]. For these reasons, the present work aims at providing a clearer insight for both solid solution (SS) and precipitated states (PS) for a better microstructural control, as a direct perspective. A process was developed with thermomechanical treatments close to industrial practices, and complementary techniques, such as scanning electron microscopy and tensile testing, were used to characterize the materials and establish relationships between microstructure and mechanical properties. This study is a first step towards the use of Ti-Ag alloys to produce antibacterial implants.

2. Material and methods

Studied Ti-7Ag alloy was fabricated by arc melting using pure titanium (>99,88 at% pure from TIMET) and silver (99,95 at% pure from STREM CHEMICAL). Pieces of silver were contained inside titanium samples, because titanium’s melting point (1668°C) is close to silver’s boiling point (2162°C). The ingot was melted five times to ensure the chemical homogeneity, and then a 15mmx15mm square section bar was prepared by suction casting. The ingot was subjected to a homogenization treatment of 24h at 1000°C under vacuum, and then a solution thermal treatment of 10min at 800°C followed by water quenching. The obtained material was defined as the initial state for the study (IS). Additional thermomechanical processing steps were

carried out including cold and hot-rolling at 600°C, and thermal treatments under vacuum or using molten salt baths with the following bath composition: 33.4wt% Na₂CO₃ / 32.1wt% Li₂CO₃ / 34.5wt% K₂CO₃. Before microstructural analysis, specimens were polished with SiC800 and SiC1200 papers and then electropolished at 25V for 45s (STRUERS Lectropol). The solution used was composed by 66vol% methanol, 27vol% butanol and 7vol% perchloric acid to obtain mirror-polished surfaces. Microstructures were then characterized by scanning electron microscopy (SEM). Electron backscatter diffraction (EBSD) analysis was performed on a Zeiss LEO 1530 SEM operating at 20kV. Backscattered electron (BSE) images were acquired on a Zeiss SUPRA 25 SEM. Finally, tensile tests were performed at room temperature on flat dog-bone specimens at a strain rate of 10⁻³s⁻¹. A 10kN Instron5966 machine equipped with a 10mm gauge length extensometer was used.

3. Results and discussion

In this study, a specific nominal composition, Ti-7Ag, was chosen to possibly access two different microstructural states through thermomechanical treatments: a solid solution (SS) and a precipitated State (PS) (Fig. 1).

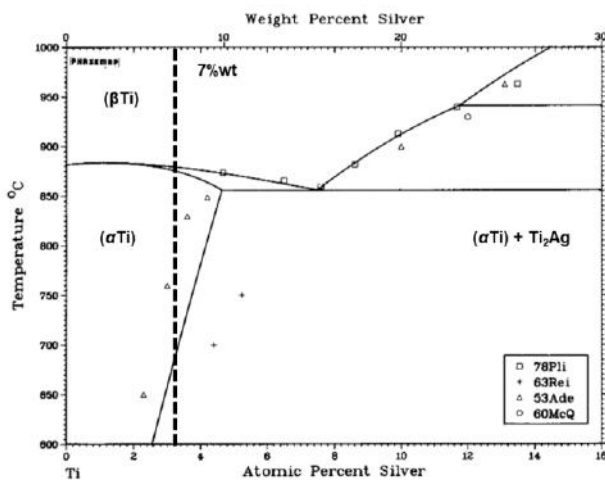


Fig. 1:Ti-Ag phase diagram adapted from literature [9]

The objective was to optimize both microstructures to obtain a fine scale dispersion of Ti₂Ag throughout the matrix and a solid solution state. To this extend, Ti-7Ag was casted, homogenized, then solution-treated and water quenched to reach a single-phase solid solution stated as initial state (IS). This state exhibited an as-cast microstructure with large-scaled grains. To obtain finer grain size, a recrystallisation treatment was considered. However, it is well known that pre-strain followed by heat treatment can possibly deeply affect the

nucleation kinetics. Indeed, Larché [10] reported that dislocations can be a favorable nucleation site for precipitates and a short circuit for accelerated solute diffusion [11]. Finally, both these phenomena apparently tend to induce a preferred precipitation on slip bands. This understanding led to the idea of using recrystallisation treatment to assist precipitation within slip bands. If the pre strain is high enough, it would be possible to attain a homogeneous precipitate distribution. For this purpose, a process adapted to industrial purpose was designed. The first step consisted in a hot rolling (600°C) stage for a first 75% thickness reduction. The second step was to bring, by cold rolling, a sufficient amount of stored mechanical energy for a subsequent efficient recrystallization stage. As a consequence a further 40% reduction step was introduced in the process, in order to induce recrystallization [12]. The last step consisted in a controlled recrystallization treatment where both time and temperature had to be first fully determined. The salt bath was chosen because it allowed an immediate immersion at the chosen temperature to reduce prior recovery (which drastically reduces the stored mechanical driving force for recrystallization). The treatment time was set at 10 min to reduce undesired phenomenon such as oxidation, but the temperature had to be determined. On one hand, the temperature needed to be high enough to induce recrystallization so at least 700°C [12], but on the other hand, the phase diagram suggested that the temperature was supposed to be below 700°C to allow Ti₂Ag precipitation (Fig. 1). However, the limit between solid solution and the dual phase was already proved to be slightly offset [9], and precipitation kinetics was not taken into account, so a further investigation was also necessary to understand the real boundaries between the single alpha phase and the two-phase fields. Hence, the recrystallization temperature was determined by systematic change of the temperature to enhance both recrystallization and precipitation, while allowing to understand the precipitation temperature range. The specimens were investigated with BSE mode to discern precipitates. Indeed, this mode provides chemically contrasted pictures, enabling to easily distinguish areas enriched in heavy elements such as silver (Z=47), which appear brighter, from those mostly comprising light elements such as titanium (Z=22), which appear darker. Moreover, the recrystallization level was assessed with EBSD. Images of the alloy treated at 650°C for 10 min are shown on Fig. 2 (a)(b)(c) and exhibits a partially recrystallized microstructural state, with remaining deformed area (circled in white). However, the precipitates appear as approximately well-dispersed away from non-recrystallized areas, so phase diagram remained

right for this range of temperature. Then, a treatment at 750°C (Fig. 2 (d)(e)(f)) exhibited a complete recrystallization: the grain size is fine-scaled and quite homogeneous (approximately 15µm), and free from deformed areas. Whereas precipitates are homogeneously dispersed within the matrix. The precipitation was not, this time, in total accordance with the phase diagram, on

which 750°C belongs to the alpha single-phase field for our nominal composition. This kind of deviation was already noticed in previous studies and can also be explained because precipitation kinetics was not taken into account in phase diagram. In the end, the treatment at 750°C was selected as the precipitation one because it allowed both precipitation and recrystallisation.

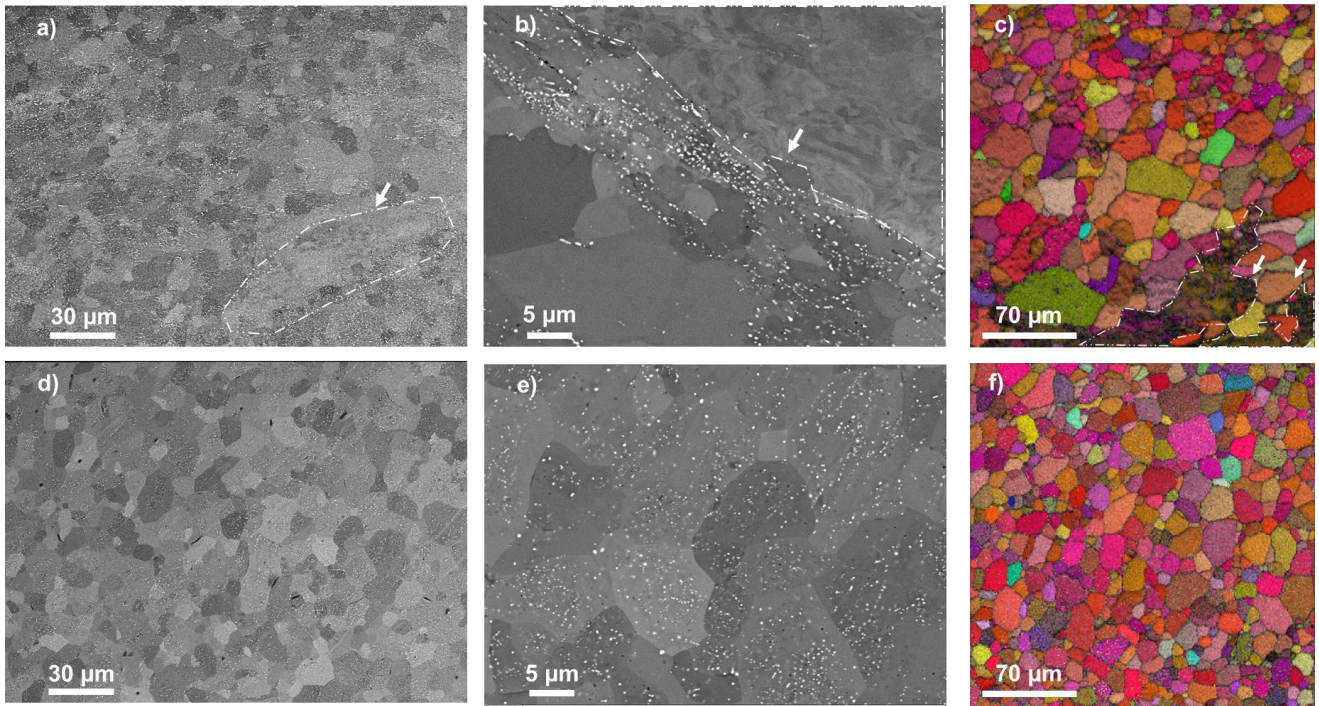


Fig. 2: BSE images of the IS specimen after deformation and recrystallization at 650°C(a)(b) or 750°C (d)(e), and EBSD map of the specimen after deformation and recrystallization at 650°C(c) or 750°C (f)

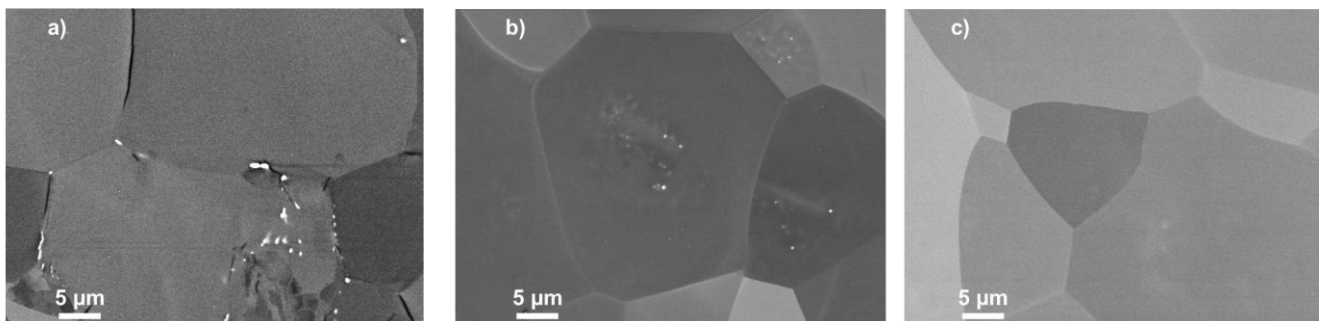


Fig. 3: BSE images of PS sample after dissolution treatment: 800°C 30min (a), 850°C 30min (b), 850°C 1h (c)

In order to reach a solid solution from the precipitated state, an additional dissolution treatment was then applied. To limit the increase in grain size, the treatment time was supposed to be as short as possible, and the temperature was fixed below the beta transus and above 750°C to reach a single phase according to our previous experiment (Fig 2). The adapted treatment was identified as 850°C for 1h (Fig. 3 (c)), because a shorter time or a lower temperature was not sufficient to dissolve all precipitates (Fig. 3 (a)(b)). Finally, a process was design to obtain an optimized microstructure for precipitated state and solid solution. The mechanical properties of these obtained states were then assessed (Fig. 4, Table 1).

Table 1: Recapitulative table of mechanical properties of Ti-7Ag alloys (PS and SS), pure titanium with the same process, and specification for Ti grade 4 [13]

Micro-structure	Young modulus (GPa)	Re _{0.2} (MPa)	R _m (MPa)	Elongation at break (%)
Ti-7Ag PS	105	370	550	34
Ti-7Ag SS	95	260	490	23
Pure Ti	100	130	270	62
Ti grade 4	104	480	550	15

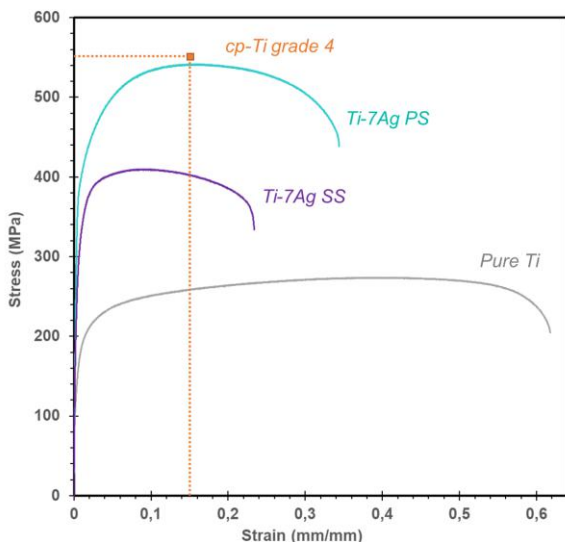


Fig. 4: Engineering stress-strain tensile curves of Ti-7Ag (PS and SS), pure titanium with the PS process, and specification for Ti grade 4 [13]

A solid solution hardening was displayed for Ti-7Ag PS and SS compared to pure Titanium. The specification of Ti grade 4 were shown in order to be

compared with our specimens. Indeed, this unalloyed titanium is already used as dental implant. Finally, the precipitated state exhibited the best compromise between ultimate strength and elongation, with even higher ductility than cp-Ti grade 4.

4. Conclusion

A new set of thermomechanical treatments adapted to industrial uses was developed to achieve optimized microstructures for both precipitated state (PS) and solid solution (SS). This study highlighted that the precipitation can be assisted by recrystallization to lead to a homogeneous distribution of precipitates. Subsequently, a solid solution state was obtained thanks to dissolution treatment. Finally, the mechanical properties were particularly interesting, especially for precipitated state because its elongation and ultimate strength were comparable to Ti grade 4, already used as dental implant. These optimized microstructures will be further studied to assess other properties such as antibacterial activity and corrosion resistance.

5. Acknowledgements

This work is financially supported by the Industrial CIFRE doctoral fellowship of Biotech Dental.

6. References

1. M. Rai, A. Yadav, A. Gade, *Biotechnology Advances* (2009) Vol.27 76–83.
2. S. Fu *et al.*, *Materials Science and Engineering C* (2021) Vol.128 112266.
3. N. Stobie *et al.*, *Biomaterials* (2008) Vol.29 963–969.
4. A. Shi *et al.*, *Materials Science and Engineering C* (2020) Vol.109 110548.
5. M. Chen *et al.*, *Materials Science and Engineering C* (2017) Vol.75 906–917.
6. M. Chen, E. Zhang, L. Zhang, *Materials Science and Engineering C* (2016) Vol.62 350–360.
7. M.K. Han *et al.*, *Materials* (2014) Vol.7 6194–6206.
8. K.F. Kelton, A.L. Greer, *Nucleation in Condensed Matter. Cohesive Properties of Semiconductors under Laser Irradiation* 2010.
9. J.L. Murray, K.J. Bhansali, The Ag-Ti (Silver-Titanium) system. *Bulletin of Alloy Phase Diagrams* 1983 Vol.4.
10. F.C. Larché, *Dislocations in Solids*. 1979 Vol.4.
11. F.J. Humphreys, M. Hatherly, *Recrystallization and Related Annealing Phenomena. Recrystallization and Related Annealing Phenomena* 2004.
12. D. Raabe, in *Physical Metallurgy* (Laughlin, D. E. & Kazuhiro, H.) 2014 Vol.3 2291–2399.
13. ASTM F67-13, *ASTM International* (2017) 8.

RECENT DEVELOPMENT OF Ti-Mo AND Ti-Cr BASED SUPERELASTIC ALLOYS

Hideki Hosoda and Masaki Tahara

Institute of Innovative Research, Tokyo Institute of Technology, 4259 Nagatsutao, Midori-ku, Yokohama, 226-8503, Japan

This presentation focuses on Ti-Mo and Ti-Cr-based superelastic (SE) alloys developed by our research group and discusses their design and SE properties. Superelasticity SE is one of the most crucial functional properties of shape memory alloys (SMAs), and room temperature (RT) SE is widely required and used for practical applications, including medical devices, in comparison to the shape memory effect (SME). In the literature, several near β -type Ti SMAs have been reported, most of which are Ti-Nb-based alloys. However, the lattice deformation strain (LDS) between the parent β (bcc) phase and martensite α'' (orthorhombic) phase in the conventional Ti-Nb binary and ternary SE alloys is relatively small, around 1-3% [1,2], compared to practical Ti-Ni SE alloys with a maximum LDS of ~10.5% [3]. Thus, we have been developing Ti-based SE alloys that exhibit both larger LDS and sufficient cold workability without utilizing medium- or high-entropy effects. This presentation introduces two recently developed alloy systems: Ti-Mo-Al and Ti-Cr-Sn. For example, Ti-3Cr-9Sn exhibits excellent SE behavior with a deformation stress of 600-800MPa, SE strain of 7.8% after 8% applied strain, and a critical stress for slip of about 600MPa. These values are comparable to those of Ti-Ni. Through all the studies, we have realized that the suppression of the ω phase is intrinsically more critical for the appearance of RT SE than generally believed.

Keywords: Ti-Mo, Ti-Cr, superelasticity, shape memory effect, lattice deformation strain

1. Introduction

Ti-based shape memory alloys (SMAs) have attracted significant interest for use in biomedical applications due to their unique properties. Near- β (bcc) Ti-based SMAs, which can contain various additional elements that dissolve into the bcc β phase of Ti, are particularly suitable for medical devices used in the human body, as they do not need to contain toxic or allergenic elements such as Ni, making them less likely to cause metallic allergies.

When the martensitic transformation temperatures (M_s) become sufficiently lower than the operation temperature (often room temperature, RT) in the SMAs, superelasticity (SE) appears. In SE deformation, applying stress triggers stress-induced forward martensitic transformation from a parent phase to a martensite phase, and shape recovery occurs automatically by removing the stress due to the reverse martensitic transformation from the martensite phase to the parent phase. SE can be achieved by lowering M_s between the parent β and the martensite α'' (orthorhombic), and suitable amounts of β -stabilizing elements can control the appearance of SE in the Ti-based SMAs. Due to the relatively low values of $d\sigma_{\text{SMT}}/dT$ (σ_{SMT} : stress for inducing martensite, and T: temperature) around a few MPa/K in Ti-based SMAs [1, 2], SE can easily appear not only at around RT but also in a wide temperature range, making Ti-based SMAs suitable for various SE applications.

While many kinds of Ti-based SMAs have been reported in the literature, most of them are Ti-Nb based alloys. The Ti-Nb based SMAs exhibit several benefits in mechanical properties and workability, which enable microstructure and texture control through thermo-mechanical treatment. However, the lattice deformation strain (LDS) between the parent β phase and the α''

(orthorhombic) martensite phase in Ti-Nb SE alloys is relatively small, around 1-3% compared to the Ti-Ni practical SE alloy with a maximum LDS of ~10% [3]. This is because the crystal structure of α'' martensite becomes closer to that of bcc due to the addition of a large amount of Nb, resulting to the enhancement of β stability. To obtain a larger LDS, the crystal structure of α'' martensite phase should be close to that of hcp martensite (α') phase. This can be achieved by adding a small amount of β -stabilizing elements. Therefore, there are two contradictory conditions in the Ti-based SE alloys with large LDS.

(1) To achieve SE at RT, a large amount of β -stabilizing elements should be added to decrease M_s sufficiently below RT.

(2) To achieve a large LDS, the amount of β -stabilizing elements should be decreased as much as possible so that the crystal structure of α'' martensite phase is closer to the hcp α' phase.

This research presents some trials to solve the problem and the present achievements of Ti-Mo and Ti-Cr based SE alloys developed by our group, focusing on their design and SE properties.

2. Ti-Mo based alloys

Although β Ti and Mo form a complete solid solution of β (Ti, Mo) at high temperature in the Ti-Mo binary phase diagram [4], the β phase with Ti-rich composition is decomposed into the β phase with Mo-rich composition and α Ti (a monotectoid reaction from β_{rich} to $\beta_{\text{lean}} + \alpha$ Ti) in the equilibrium condition. Thus, the β phase with Ti-rich composition quenched from high temperature must be more unstable due to the suppression of the monotectoid reaction in compared with the simple phase separation (precipitation) from β (Ti, Mo) to $\beta + \alpha$. This

leads to larger LDS expected in the Ti-Mo based alloys without decreasing the β stabilizer content. However, in the binary Ti-Mo alloys, very small SE shape recovery has been obtained: the maximum SE was 0.7% in water-quenched Ti-12mass%Mo [5]. The poor SE is caused by existence of large amount of ω phase. Therefore, the reduction and suppression of ω phase should be solved, and that can be achieved by addition of ω inhibitor elements. These elements, Zr, Al, Ga, Sn, O are often classified into Al-stabilizers or neutral elements in Ti. In the Ti-Mo based alloys, stable SE appears in the (Ti, Zr)-Mo-Sn [6] and Ti-Mo-Sn-Zr quaternary alloys [7, 8]. It is also revealed that the addition of Sn and Zr decreases M_s but not largely decreases LDS [9]. SE was not obtained for long time in Ti-Mo-X ternary systems such as Ti-Mo-Al [10, 11] and Ti-Mo-Ga [12, 13] except for Nb [14], but recently stable SE can be achieved in the Ti-Mo-Al ternary system [15]. With increasing Al content without changing reverse martensitic transformation start temperature (A_s), the deformation mechanism changes from twin deformation (Ti-6mol%Mo binary) to SME (Ti-6mol%Mo-5mol%Al) and SE (Ti-6mol%Mo-10mol%Al). Not only the reduction of volume fraction of ω phase but also the number density of ω phase particles is important for the appearance of RT SE in the Ti-Mo-Al alloys. ω phase is easily formed in Ti-Mo-Al alloys even when Al content is relatively high around 14mol%, and isothermal ω phase and isothermal α'' phase coexist in aged Ti-6Mo-14Al alloy [16, 17]. A solution-treated Ti-6.1mol%Mo-10.8mol%Al (Ti-12mass%Mo-6mass%Al) alloy exhibit good SE at RT with large SE shape recovery of 5.5% after 8% deformation.

3. Ti-Cr based alloys

As Ti-Cr binary alloys possess poor workability at room temperature [18], there is currently no literature reporting either SE or SME in the binary alloys. In the equilibrium Cr-Ti binary phase diagram [4], β -Ti is not stabilized, regardless of alloy composition, due to the eutectoid reaction from β to α +Cr₂Ti. Therefore, quenched-in β phase must be more unstable due to the suppression of the eutectoid reaction. We have explored the Ti-Cr-Sn system in detail and reported on the SME and mechanical properties of Ti-6mol%Cr-3mol%Sn alloy mainly [19-22]. However, we were unable to obtain SE in this compositional range of Ti-4~7mol%Cr-0~4mol%Sn despite precisely controlling the chemical composition. At present we have realized that the disappearance of SE in the compositional range is caused by the formation of ω phase. Consequently, we have reinvestigated the Ti-Cr-Sn system but a different compositional region (lower Cr content than 5mol% and higher Sn content than 6mol% to

suppress ω phase formation) [23]. As a result, it was found that good SE appears in Ti-4Cr-6.5Sn, Ti-3.5Cr-7.0Sn, Ti-3.0Cr-7.5~8.0Sn and Ti-2.5Cr-8.5Sn (mol%) alloys. The slip stress of Ti-3.0Cr-7.5Sn alloy reached 500MPa due to large solid solution strengthening by Sn addition, where the slip stress is defined as the stress that introduces 0.5% permanent (not shape recoverable) strain. Ti-4.0Cr-6.5Sn alloy possessed large shape recovery strain of 6.5% by unloading only, 4.0% SE strain (transformation strain), and high slip stress of 641MPa (when 0.5% permanent strain was generated) [24]. The flow stress during superelastic deformation reached 420MPa. Although the chemical compositional region for RT SE slightly changes depending on impurities such as oxygen, Ti-3Cr-9Sn alloy exhibited excellent SE behavior with a deformation stress of 600-800MPa, SE strain of 7.8% after 8% applied strain, and a critical stress for slip of about 600MPa. These SE properties of the Ti-Cr-Sn alloys are comparable to those of TiNi. Therefore, the Ti-Cr-Sn alloy system is a promising candidate to produce a practical SE alloy which can replace Ti-Ni in the field of medical devices, especially. Now we are also conducting additive manufacturing researches using the Ti-Cr-Sn alloys as a collaboration with Profs T. Nakano and Y. Koizumi at Osaka Univ., Japan. Besides, for medical applications, Bi-added Ti-Cr alloys [25, 26] and Au-added Ti-Cr alloys [27-33] have been systematically reported where Bi and Au additions are considered to improve X-ray radiography.

4. Acknowledgements

This work is supported by the Japan Society for the Promotion of Science (JSPS) (KAKENHI 19H02417, 20K20544, 22K18899, 22H00256 and 22H05276).

5. References

- [1] H.Y. Kim, Y. Ikehara, J.I. Kim, H. Hosoda, S. Miyazaki, *Acta Materialia*, 54 (2006) 2419-2429.
DOI: 10.1016/j.actamat.2006.01.019.
- [2] S. Miyazaki, H.Y. Kim, H. Hosoda, *Materials Science and Engineering: A* 438-440, (2006) 18-24,
DOI: 10.1016/j.msea.2006.02.054
- [3] S. Miyazaki, S. Kimura, K. Otsuka and Y. Suzuki, *Scripta Metallurgica*, 18 (1984) 883-888. (1984).
DOI: 10.1016/0036-9748(84)90254-0
- [4] H. Okamoto, *Desk Handbook Phase Diagrams for Binary Alloys*, Second Edition, (2010), ASM International, Materials Park, OH, USA. p.294 (Cr-Ti) and p. 609 (Mo-Ti).
ISBN 13: 978-1-61503-046-0

- [5] C.H. Wang, M. Liu, J.C. Peng, J.A. Wang, Z.M. Ren, G.H. Cao, *Journal of Alloys and Compounds*, 720 (2017) 488-4
DOI: 10.1016/j.jallcom.2017.05.29996.
- [6] M. F. Ijaz, H.Y. Kim, H. Hosoda, S. Miyazaki, *Materials Science and Engineering C* 48 (2015) 11-20
DOI: 10.1016/j.msec.2014.11.010
- [7] K. Endoh, M. Tahara, T. Inamura, H.Y. Kim, S. Miyazaki, H. Hosoda, *Journal of the Japan Institute of Metals and Materials*, 80 (2015) 37-44
doi.org: 10.2320/jinstmet.JB201509
- [8] K. Endoh, M. Tahara, T. Inamura, H. Hosoda, *Materials Science & Engineering A* 704 (2017) 72-76
DOI: 10.1016/j.msea.2017.07.097
- [9] K. Endoh, M. Tahara, T. Inamura, H. Hosoda, *Journal of Alloys and Compounds*, 695 (2017) 76-
DOI: 10.1016/j.jallcom.2016.10.10882
- [10] H. Hosoda, N. Hosoda and S. Miyazaki, *Transactions of Materials Research Society in Japan*, 26 (2001) 243-246.
- [11] H. Hosoda, M. Taniguchi, T. Inamura, H. Kanetaka, S. Miyazaki, *Materials Science Forum*, 654-656 (2010) 2150-2153
DOI: 10.4028/www.scientific.net/MSF.654-656.2150
- [12] H. Hosoda, Y. Ohmatsu and S. Miyazaki: *Transactions of Materials Research Society of Japan*, 26 (2001) 235-238.
- [13] H. Y. Kim, Y. Ohmatsu, J. I. Kim, H. Hosoda and S. Miyazaki, *Materials Transactions*, 45 (2004) 1090-1100.
DOI: 10.2320/matertrans.45.1090
- [14] Y. Al-Zain, H.Y. Kim, H. Hosoda, T.H. Nam, S. Miyazaki, *Acta Materialia*, 58 (2010) 4212-4223
DOI: 10.1016/j.actamat.2010.04.013
- [15] N. Nohira, Y. Oshita, W.T. Chiu, A. Umise, M. Tahara, H. Hosoda, *Materials*, 15 (2022) 861
DOI: 10.3390/ma15030861
- [16] N. Nohira, Y. Oshita, W.T. Chiu, A. Umise, M. Tahara, H. Hosoda, *Micro*, 2 (2022) 113-122
DOI: 10.3390/micro2010007
- [17] N. Nohira, Y. Oshita, W.T. Chiu, A. Umise, M. Tahara, H. Hosoda, *Materials Characterization*, 199 (2023) 112850
DOI: 10.1016/j.matchar.2023.112850
- [18] W.T. Chiu, K. Wakabayashi, A. Umise, M. Tahara, T. Inamura, H. Hosoda, *Journal of Alloys and Compounds*, 875 (2021) 160088
DOI: 10.1016/j.jallcom.2021.160088
- [19] A. Wadood, T. Inamura, H. Hosoda, S. Miyazaki, *Materials Transactions*, 52 (2011) 1789-1793
DOI: 10.2320/matertrans.M2011153
- [20] A. Wadood, T. Inamura, H. Hosoda, S. Miyazaki, *Materials Science and Engineering A*, 530 (2011) 504-510.
DOI: 10.1016/j.msea.2011.10.009
- [21] A. Wadood, T. Inamura, Y. Yamabe-Mitarai, H. Hosoda, *Materials Science and Engineering A*, 555 (2012) 28-35.
DOI: 10.1016/j.msea.2012.06.029
- [22] A. Wadood, T. Inamura, Y. Yamabe-Mitarai, H. Hosoda, *Materials Science and Engineering A*, 559 (2013) 829-835.
DOI: 10.1016/j.msea.2012.09.030
- [23] M.S. Park, W.T. Chiu, N. Nohira, M. Tahara, H. Hosoda, *Materials Science and Engineering: A* 822 (2021) 141668
DOI: 10.1016/j.msea.2021.141668
- [24] M.S. Park, W.T. Chiu, N. Nohira, M. Iwasaki, M. Tahara, H. Hosoda, *Materials Science and Engineering: A* 869 (2023) 144790
doi.org/10.1016/j.msea.2023.144790
- [25] N. Nohira, K. Hayashi, M. Tahara, H. Hosoda, *Journal of Materials Research and Technology*, 23 (2023) 5644-5652
DOI: 10.1016/j.jmrt.2023.02.173
- [26] N. Nohira, K. Hayashi, M. Tahara, H. Hosoda, *Journal of the Mechanical Behavior of Biomedical Materials*, 141 (2023) 10588
DOI: 10.1016/j.jmbbm.2023.105800
- [27] W.T. Chiu, T. Ishigaki, N. Nohira, A. Umise, M. Tahara, H. Hosoda, *Journal of Alloys and Compounds*, 857 (2021) 157599
DOI: 10.1016/j.jallcom.2020.157599
- [28] W.T. Chiu, T. Ishigaki, N. Nohira, A. Umise, M. Tahara, H. Hosoda, *Journal of Alloys and Compounds*, 867 (2021) 159037
DOI: 10.1016/j.jallcom.2021.159037
- [29] W.T. Chiu, K. Wakabayashi, A. Umise, M. Tahara, T. Inamura, H. Hosoda, *Journal of the Mechanical Behavior of Biomedical Materials*, 123 (2021) 104707
DOI: 10.1016/j.jmbbm.2021.104707
- [30] W.T. Chiu, K. Wakabayashi, A. Umise, M. Tahara, T. Inamura, H. Hosoda, *Journal of Alloys and Compounds*, 897 (2022) 163134
DOI: 10.1016/j.jallcom.2021.163134
- [31] W.T. Chiu, K. Fuchiwaki, A. Umise, M. Tahara, T. Inamura, H. Hosoda, *Materials Science and Engineering: A* 847 (2022) 143312
DOI: 10.1016/j.msea.2022.143312
- [32] W.T. Chiu, K. Fuchiwaki, A. Umise, M. Tahara, T. Inamura, H. Hosoda, *Journal of the Mechanical Behavior of Biomedical Materials*, 133 (2022) 105358
DOI: 10.1016/j.jmbbm.2022.105358
- [33] W.T. Chiu, K. Fuchiwaki, A. Umise, M. Tahara, T. Inamura, H. Hosoda, *Journal of Alloys and Compounds*, 920 (2022) 166016
DOI: 10.1016/j.jallcom.2022.166016